Technische Universität München

TUM School of Natural Sciences

Modeling Coated Gasoline Particulate Filters

Raimund Mathias Heinz Walter

Vollständiger Abdruck der von der TUM School of Natural Sciences der
Technischen Universität München zur Erlangung des akademischen
Grades eines

Doktors der Ingenieurwissenschaften (Dr.-Ing.)

genehmigten Dissertation.

Vorsitz: Hon.-Prof. Dr. Richard W. Fischer
Prüfer*innen der Dissertation: 1.   Prof. Dr.-Ing Kai-Olaf M. Hinrichsen
                                 2.   Prof. Dr.-Ing. Harald Klein

Abstract

The growing public awareness regarding air pollution drives the trend towards stricter regulations, thereby, forcing carmaker to improve the aftertreatment system of their cars. Gasoline engines are equipped with catalysts to reduce or store the harmful gaseous species and with a gasoline particulate filter (GPF) to capture soot. The increasing requirements on the aftertreatment demand more active catalysts and a higher catalytic active volume compared to previous systems. Hereby, the integration of three-way catalysts (TWC) and gasoline particulate filters into a single so-called coated GPF (cGPF) can decrease the necessary packaging volume and costs causing cGPFs to be a critical element of future emission concepts.

The complex interaction of filter substrate and washcoat in cGPFs requires additional research. A deep understanding of the underlying phenomena is necessary because upcoming cars must meet the legislation under an enlarged window of driving conditions. The filter properties strongly influence the performance but also its costs. This work aims to establish a simulation model for cGPFs which allows a predictive evaluation of pressure drop, filtration and catalytic conversion under harsh real-driving conditions. The development of this model proceeds in four steps.

In a first step, an extension to established channel scale filtration models is proposed to predict the particle number filtration of GPFs. As validation, the particle-size resolved filtration efficiency of seven cordierite filters is determined on a dynamic engine test bench. The steady-state as well as transient experiments include variations of the pore size distribution and the filter wall thickness. After the inclusion of a new correlation for the particle collection due to inertial deposition, the model reliably replicates the influence of the wall thickness, pore size-distribution and the operating conditions on the filtration characteristics of uncoated GPFs.

In a next step, this filtration model is extended to coated filters. Accordingly, necessary filter characteristics after coating are gathered by analyzing cGPFs and their corresponding uncoated substrate on a pore scale level with 3D X-ray microscopy. The properties are then embedded into the simulation model in order to capture the dynamic pressure drop and filtration behavior. The model successfully replicates the accompanying measurements conducted on a dynamic engine test bench. Due to the reduced porosity and due to the decrease of medium sized pores relative to the uncoated substrate, the experiments

reveal a lower filtration efficiency after coating that was also predicted by the simulations. To capture the chemical behavior of cGPFs under highly dynamic operating conditions, a new global kinetic model considering standard TWC reactions is developed. Submodels were introduced for the extent of oxidation of the active centers and for oxygen storage. With the goal to establish a model that is applicable under a wide range of operating conditions, steady-state and transient experiments were conducted on a engine test bench to calibrate the approach. After calibration, it was possible to accurately predict the tailpipe emissions released in a WLTP driving cycle.

A filter can either be coated solely in-wall or have a partially or fully on-wall coating. In addition it is possible to apply advanced coating technologies. Zoning, for instance, creates domains of high and low washcoat loading, resulting in a non-uniform washcoat distribution. The combination of both technologies results in a variety of coating configurations. To investigate their impact on pressure drop, high load conversion, and light-off performance, a new methodology to describe the cGPF with coating parameters is embedded into the existing model. The resulting simulations show an enhanced light-off at steady-state conditions if more washcoat is deposited at the front part of the filter or on the inlet channel wall. However, under transient conditions, a filter with a partial catalytic layer on the outlet channel performs best.

The presented simulation model predicts the pressure drop, filtration efficiency and chemical conversion performance of coated gasoline particulate filters under highly transient conditions encountered at real driving scenarios. Next to the application in exhaust gas aftertreatment design, the developed approach enables a fast,early and compared to measurements cheap evaluation of new GPF and TWC technologies.

Zusammenfassung

Das wachsende Problembewusstsein in der Bevölkerung für Luftverschmutzung spiegelt sich in strengeren gesetzlichen Regulatorien wieder. Dadurch werden beispielsweise auch Automobilhersteller verpflichtet, die Abgasnachbehandlung ihrer Fahrzeuge zu verbessern. Nach Stand der Technik sind Autos mit Ottomotoren bereits mit Katalysatoren zum Abbau und zur Speicherung von schädlichen gasformigen Stoffen als auch einem Otto-Partikelfilter (OPF) zum Filtern von Ruß ausgestattet. Durch die gestiegenen Anforderungen an die Abgasnachbehandlung sind im Vergleich zu bestehenden Systemen aktivere Katalysatoren und ein größeres katalytisch wirksames Volumen notwendig. Ein sogenannter beschichteter Otto-Partikelfilter (bOPF), die Integration eines Drei-Wege-Katalysators in einen Otto-Partikelfilter, kann dabei helfen, den notwendigen Bauraum und die Kosten zu minimieren. Der beschichtete Otto-Partikelfilter stellt somit ein wichtiges Element für zukünftige Emissionskonzepte dar.

Die komplexe Wechselwirkung des Filtersubstrats mit der Beschichtung in einem bOPF erfordert eine tiefere Betrachtung. Ein genaues Verständnis der zugrundliegenden Phänomene ist notwendig, da zukünftige Fahrzeuge die Grenzwerte in einem deutlich erweiterten Fahrbereich einhalten müssen. Der Aufbau des Filters beeinflusst stark die Wirksamkeit aber auch die Kosten des Bauteils. Das Ziel dieser Arbeit ist es daher, ein Simulationsmodel für den bOPF zu entwickeln, welches die prädiktive Bewertung des Gegendrucks, der Filtrationsleistung sowie der katalytischen Schadstoffkonvertierung unter den anspruchsvollen RDE (real driving emissions) Bedingungen erlaubt.

In einem ersten Schritt wurde eine Erweiterung bestehender Filtermodellen auf Kanalebene zur Simulation der Partikelanzahl-Filtration in OPFs erarbeitet. Zur Validierung werden Messungen von sieben Cordierit-Filtern auf einem speziell dafür ausgestatten Motorprüfstand verwendet. Die Messtechnik analysiert die quantitative Partikelgrößenverteilung vor und nach dem Filter. Die für diese Arbeit durchgeführten stationären sowie transienten Experimente beinhalteten Variationen der Porengrößenverteilung und der Wandstärke. Durch die Einführung einer neuen Korrelation für die Partikelabscheidung durch Trägheitsablagerung kann das Modell den Einfluss der Porengrößenverteilung, Substrateigenschaften und Betriebsbedingungen auf die Filtrationscharakteristik eines unbeschichteten OPFs korrekt wiedergeben. In einem nächsten Schritt wurde dieses Modell für beschichtete Filter erweitert. Dabei wurden die Eigenschaften des Filters vor

und nach der Beschichtung über dreidimensionale Röntgenmikroskopie auf Porenebene bestimmt. Die so ermittelten Eigenschaften dienen als Eingang in das Simulationsmodell, um den Gegendruck sowie das dynamische Filtrationsverhalten vorherzusagen. Das Modell repliziert erfolgreich begleitende Messungen auf einem Motorprüfstand. Aufgrund der reduzierten Porosität and einer Verringerung der Poren im mittleren Größensegment der beschichteten Filter, zeigen die Experimente eine niedrigere Filtrationseffizienz für bOPFs als für das korrespondierende unbeschichtete Substrat. Diesen Effekt zeigt die Simulation auf gleiche Weise.

Um das chemische Verhalten des Filters unter dynamischen Betriebsbedingungen in das Modell einzubeziehen, wurde ein neuer globaler Reaktionsmechanismus, aufbauend auf den etablierten Drei-Wege-Katalysator Reaktionen, entwickelt. Hierbei wurden Untermodelle für die Oxidation der aktiven Zentren und des Sauerstoffspeichers implementiert. Zur Kalibrierung des Modells wurden stationäre als auch dynamische Messungen auf einem Motorprüfstand durchgeführt, mit dem Ziel ein unter einem breiten Bereich an Betriebsbedingungen gültiges Modell zu erhalten. Das so kalibrierte Modell konnte die emittierten Emissionen in einem WLTP-Zyklus exakt vorhersagen. Ein Filter kann entweder nur in der Wand (in-wall), oder auf der Wand (auf-wand) beschichtet werden. Zusätzlich besteht die Möglichkeit moderne Beschichtungstechnologien zu verwenden. Eine sogenannte Zonierung erzeugt Bereiche mit niedriger beziehungsweise höherer Washcoatmenge, was zu einer inhomogenen Katalysatorverteilung innerhalb des Filters fuhrt. Die Kombination von Zonierung mit den unterschiedlichen Beschichtungsarten ermöglicht eine Vielzahl an Beschichtungskonfigurationen. Um den Einfluss dieser Konfigurationen auf Gegendruck, Hochlastkonvertierung und Kaltstartkonvertierung zu untersuchen, wurde eine neue Methode zur Beschreibung der Beschichtung mithilfe von dimensionslosen Kennzahlen entwickelt und in das Modell integriert. Die resultierenden Simulationen zeigen eine verbesserte Konvertierung beim quasi-stationären Kaltstart, wenn mehr Washcoat im vorderen Teil des Filters oder auf der Wand des Einlasskanals platziert ist. Unter transienten Kaltstartbedingungen erreicht allerdings eine partielle Beschichtung des Auslasskanals die höchste Konvertierung.

Das in dieser Arbeit entwickelte Simulationsmodell kann prädiktiv die wesentlichen Eigenschaften beschichteter Ottopartikelfilter, den Gegendruck, die Filtrationseffizienz und die Schadstoffkonvertierung, ermitteln. Dies gilt sowohl für stationäre, als auch für hochtransiente Bedingungen, wie sie sich auch bei realen Fahrszenarien auftreten. Neben der Optimierung der Auslegung von Emissionskonzepten ermöglicht der entwickelte Ansatz eine schnelle, frühzeitige und vor allem zu experimentellen Ansätzen kostengünstige Bewertung neuer bOPF-Technologien.

Content

Nomenclature

Latin Symbols

A_{Ad}	pre-exponential factor of equilibrium constant, $[\frac{\text{m}^3}{\text{mol}}]$
$A_{\text{wsc}}^{\text{ow}}$	cross-sectional area of the on-wall layer in one channel, $[\text{m}^2]$
A_{pre}	pre-exponential factor, $[\frac{\text{m}^2}{\text{s}\cdot\text{mol}}]$
$c_{gas,p}$	gaseous heat capacity, $[\frac{\text{J}}{\text{kg}\cdot\text{K}}]$
c_S	solid heat capacity, $[\frac{\text{J}}{\text{kg}\cdot\text{K}}]$
c	concentration, $[\frac{\text{mol}}{\text{m}^3}]$
Cf_j	friction coefficient, $[-]$
D	channel width, $[\text{m}]$
$D_D = \frac{k_B \cdot T}{3\pi \cdot \mu \cdot d_p} \cdot SCF$	length scale of the filter collector, $[-]$
D_{eff}	effective diffusion coefficient, $[\frac{\text{m}^2}{\text{s}}]$
$D_{i,M}$	mixture diffusion coefficient of species i, $[\frac{\text{m}^2}{\text{s}}]$
d_p	particle mobility diameter, $[\text{m}]$
E_A	activation energy, $[\frac{\text{J}}{\text{mol}}]$
$f(\varepsilon)$	Kuwabara's formular, $[-]$
FE	filtration efficiency, $[-]$
G	inhibition factor $[-]$
$GHSV$	space velocity at standard conditions $[\frac{1}{\text{h}}]$
H_{Ad}	heat of adsorption, $[\frac{\text{J}}{\text{mol}}]$
h	heat transfer coefficient, $[\frac{\text{W}}{\text{m}^2\text{K}}]$
H_B^0	heat of formation, $[\frac{\text{J}}{\text{mol}}]$
k	mass transfer coefficient, $[\frac{\text{m}^2}{\text{s}}]$
k_B	Boltzmann's constant, $[\frac{m^2 kg}{s^2 K}]$
$Kn = \frac{2\lambda}{d_p}$	Knudsen number, $[-]$
k_{w}	wall permeability, $[\text{m}^2]$
$k_{\text{w,ow}}^*$	effective on-wall layer permeability, $[\text{m}^2]$
$k_i = A_{pre} \cdot exp(-\frac{E_A}{RT})$	reaction rate constant, $[\frac{\text{m}^2}{\text{s}\cdot\text{mol}}]$
K	equilibrium constant $[-]$
l_{d_c}	length scale of the filter collector, $[-]$
$\dot{m}$	mass flow, $[\frac{\text{kg}}{\text{s}}]$
NCOE	normalized cumulative outlet emissions, $[-]$
NOE	normalized outlet emissions, $[-]$
N_R	interception parameter, $[-]$
p	local pressure, $[\text{Pa}]$
pdf	probability density function, $[-]$
Pe	Peclet number, $[-]$
PN	particle number, $[\#]$

PNC	particle number concentration, [#/cm^3]
Q_f	quality factor of the chemical conversion, [-]
$\dot{r}_i$	reaction rate, [$\frac{mol}{m^3 \cdot s}$]
R	universal gas constant, [$\frac{J}{mol \cdot K}$]
$Re_w = \frac{\rho \cdot v_w \cdot D}{\mu}$	wall Reynolds number, [-]
$SCF = ...$ $1 + Kn(1.257 + 0.4 \cdot exp(\frac{1.1}{Kn}))$	Stokes Cunningham correction factor, [-]
St	Stokes number, [-]
$SV = \frac{\dot{V}}{V_{Filter}}$	space velocity, [s^{-1}]
T	temperature, [K]
$T50$	inlet temperature at 50% conversion, [$^\circ$C]
t_w	wall thickness, [m]
t_{ow}	on-wall layer thickness, [m]
$U_i = (\frac{d_{c,i}}{l_{dc}})^2 \cdot v_w$	interstitial velocity , [$\frac{m}{s}$]
v	velocity along the channel axis, [$\frac{m}{s}$]
v_w	wall flow velocity, [$\frac{m}{s}$]
w	mass fraction, [-]
X	conversion, [-]
x	through-wall direction, [m]
y	molar fraction, [-]
z	axial coordinate, [m]

Greek Symbols

$\beta_j(Re_w)$	momentum flux correction factor, [-]
$\theta = \frac{c_{CeO_2}}{c_{CeO_2}+2c_{Ce_2O_3}}$	OSC filling level, [-]
ε	porosity, [-]
η	collection efficiency, [-]
λ_s	effective filter conductivity, [$\frac{W}{m \cdot K}$]
λ	air fuel equivalence ratio, [-]
ϕ_{wsc}	volumetric washcoat fraction, [-]
μ	dynamic viscosity, [Pa$\cdot$s]
ρ	density, [$\frac{kg}{m^3}$]
τ	tortuosity, [-]
ξ	partial coating factor in axial direction, [-]
χ	fraction of washcoat in the lowly-washcoated zone, [-]
ζ	on-wall fraction, [-]

Subscript

cord	cordierite
cum	cumulative
eff	effective quantity
fast	fast OSC
i	species i
iw	in-wall
j	channel index (1: inlet channel, 2: outlet channel)
ow	on-wall
slow	slow OSC
w	wall
wsc	washcoat

Abbreviations

cGPF	coated gasoline particulate filter
DPF	diesel particulate filter
GPF	gasoline particulate filter
iw-HL	in-wall high low
iw-HN	in-wall high no
iw-LH	in-wall low high
iw-NH	in-wall no high
meas	measurement
MPS	mean pore size
norm	normalized
OSC	oxygen storage capacity
owi	on-wall inlet channel
owo	on-wall outlet channel
PGM	platinum group metals
RDE	real driving emissions
sim	simulated
SCR	selective catalytic reduction
TWC	three-way catalyst
WLTC	worldwide harmonized light duty test cycle
XRM	X-Ray microtomography

1 Introduction

1.1 Research Context

The growing public awareness of air pollution by traffic drives the policymakers towards stricter regulations. Yet, most of todays powertrains do still consist of internal combustion engines. Carmakers need to improve the abatement systems to meet the regulations. The following section aims to provide an overview of the current framework surrounding the exhaust gas aftertreatment of gasoline engines.

1.1.1 Automotive Emissions and the Corresponding Legislation

The stringent legislation regarding automotive emissions in the European union and California, as the state with the most stringent regulations in the US market, have a great impact on the global pollution. In consequence, it was possible to reduce the global amount of fine particulate matter (PM2.5) road emission by 60% since the 1990s [1]. As a third major market, China introduced regulation similar to the European laws. Huang et al. evaluated the impact of the emission regulation on the air quality and public health in Chinese cities [2]. Similar to earlier studies in Europe or US [3, 4], they ascertained that the stricter legislation limits decreased the air pollution and substantially increased public health [2]. Models of the future road transport predict a further decrease of the NOx emissions by 80% in the next 20 years [5].

Due to the non-ideal, incomplete combustion of fuel, gasoline and diesel engines emit harmful pollutants next to CO_2 and water. The major emissions are carbon monoxide (CO), nitrogen oxides (NO_x), unburned hydrocarbons (HC) and particles. For gasoline engines mostly NO is emitted as NO_x. HC emissions are a mixture of aliphatic, olefinic and aromatic compounds [6, 7].

Especially, particle emissions have a negative impact on human health by causing and aggravating heart or lung diseases [8, 9]. When these particles are emitted to the atmosphere, they diminish visibility, absorb solar radiation, change the heat balance of the atmosphere, settle on plants and inhibit photosynthesis [10]. Next to the particle emissions, NOx is strongly regulated, since e.g., it is associated with the development of asthma, headaches and chronically reduced lung function [11].

The other two main emissions HC and CO already created a discussion about urban air quality in the 1970s [12]. CO exposure results in fatigue, dizziness and in extreme cases suffocation due to inadequate oxygen delivery to the brain [13]. Similar, inhaling low doses of HC already causes dizziness and headache [13]. As a result, the first Emissions Directive (70/220/EEC) in the European union was published in 1970 [14]. To cope with this, automotive manufacturers introduced the three-way catalyst for the aftertreatment of gasoline engines [15]. Afterwards, approximately every four to five years the European union adapted the emission limits for gasoline engines (see Table 1.1).

Table 1.1: Overview of the European legislations regarding emissions from light-duty vehicles with direct injection gasoline engines [16]

Model Year		Euro 1 1992	Euro 2 1996	Euro 3 2000	Euro 4 2005	Euro 5 2009	Euro 6 2014
Directive		91/441/EWG	04/12/EG	08/69/EG	98/69/EG	V0 EG 715/2007 with V0 EG 692/2008 and V0 EG 459/2012	
CO	g/km	2.72	2.2	2.3	1	1	1
HC+NOx	g/km	0.92	0.5	-	-	-	-
Total HC	g/km	-	-	0.2	0.1	0.1	0.1
NOx	g/km			0.15	0.08	0.06	0.06
Particle Mass	mg/km	-	-	-	-	4.5	4.5
Particle number	#/km	-	-				$6 \cdot 10^{11}$
Non-methane HC	g/km	-	-		-	0.068	0.068

1.1.2 Drive Cycles

Defined emissions test cycles on chassis dynamometers are applied to determine the emissions. At first, the new european driving cycle (NEDC) was applied to determine the emission levels. Later on with the Euro 6 legislation, the more dynamic worldwide harmonized light vehicles cycle (WLTC) was introduced [17]. In contrast to the NEDC, it is longer with quicker accelerations and short breaks as can be seen in Figure 1.1.
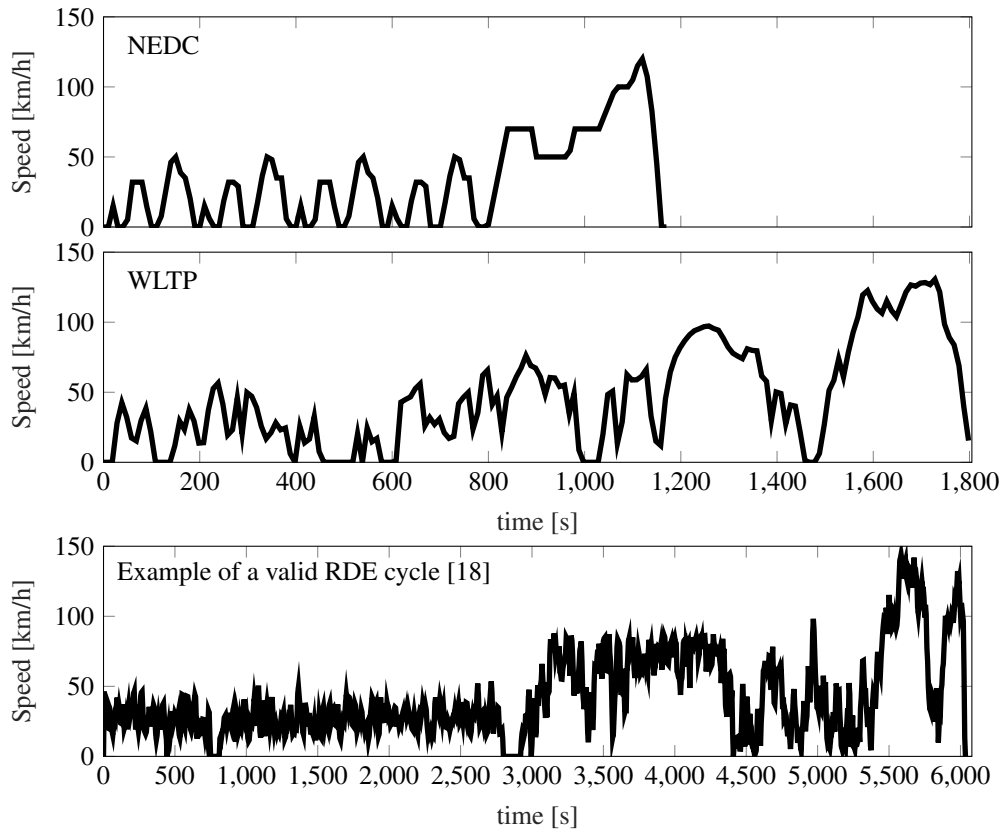
Figure 1.1: Velocity characteristics of a NEDC and WLTC as well as an example of a RDE driving cycle.

Since the actual emission reductions were in some instances lower than what would be expected from the gradual decrease in nominal emission limits [19], portable emission measurement systems (PEMS) were introduced to measure the emissions on the road. Especially, the measured emission level of diesel cars exceeded the one determined during emission test cycles [20–26]. For gasoline engines, these studies mostly focused on particle number (PN) emissions [27–31]. Thus, in a later stage of the Euro 6 legislation, real driving emissions (RDE) tests were introduced. During these tests, emissions are measured on the road using a PEMS. Due to the lower accuracy of the portable devices, certain conformity factors can be applied on the results. Also, certain limitations on the ambient temperature, altitude and speed are imposed for a measurement to be valid. In addition, the dynamic of the drive is monitored by the relative positive acceleration, which is the product of the acceleration and the velocity [32].

Still, the RDE legislation shifted the focus in the design of exhaust gas aftertreatment systems from legislated test cycle to critical driving scenarios. Previously, homologation tests with solely known driving scenarios at clear ambient conditions were applied as

valuation basis. New emission concepts and technologies could be evaluated applying steady-state operating conditions and few known transient driving scenarios [33]. Now, in a RDE test, all modes of operation as well as many highly dynamic transient maneuvers are possible. The extension of operating modes yields an enlarged range of temperature and space velocity conditions for the exhaust gas aftertreatment [34]. Next to the NEDC and WLTC, Figure 1.1 shows an example of a possible RDE velocity characteristics [18]. As can be seen, the RDE cycle also contains three stages. At first, a urban driving part with velocities below $60\,km{\cdot}h^{-1}$, however, in contrast to the NEDC and WLTC, the RDE cycle does not have a short idle period at the beginning but starts immediately with an acceleration. In the second part, the overland driving, velocities up to $100\,km{\cdot}h^{-1}$ are encountered. Here, also the velocity exhibits a more dynamic characteristics than for the WLTC or NEDC. The last part resembles highway driving at higher velocities up to $150\,km{\cdot}h^{-1}$. Again, the NEDC shows less acceleration than the WLTC or the exemplary RDE cycle.

The RDE legislation in Europe shifted the attention from emission levels to test conditions. A detailed understanding of the interaction between engine, ambient conditions and the aftertreatment system is necessary in order to create the necessary evaluation tests for the aftertreatment.

1.1.3 Composition of Three-Way Catalysts

In-engine modifications aiming to decrease the emissions of gasoline engines, like measures to enhance fuel/air mixing in the cylinder or exhaust gas recirculation can significantly reduce the emissions level [33, 35, 36]. Modern catalysts, however, usually operate above 90% conversion rates and are therefore the major contributor to the emission reduction.
Catalysts, in general, are substances that can increase the rate of a chemical reaction while remaining unchanged during the process. A heterogeneous catalyst describes a system with the catalyst and the reactants not in the same phase, e.g. gaseous and solid. Here, the reactants adsorb on the catalyst surface, often forming an intermediate which provides an alternative reaction pathway with a lower activation energy.

In the exhaust gas aftertreatment of gasoline engines, the three-way-catalyst (TWC), which can simultaneously abate CO, HC, and NO, utilizes precious metals as catalysts. To increase the active surface, these metals are incorporated in a washcoat made of γ-alumina

and different promoters, e.g. cerium, zirconium or lanthanum oxides [37–39]. Possible catalytic active precious metals were tested but not all are suitable for the application in the automotive industry [40, 41]. Ruthenium which is active for the NO reduction cannot be implemented in aftertreatment systems because it is poisonous [42]. For the same reasons and its low boiling point, iridium is not applied. Thus, the precious metals platinum, palladium and rhodium are most often applied. Whereas platinum is often employed for diesel engines due to its good oxidation performance of CO and HC, its low temperature stability makes the application for gasoline engines challenging. In consequence, most often palladium and rhodium are applied as active component [43–46].

To optimize pressure drop, thermal mass and surface area, the washcoat with the active components is deposited on a carrier. The structure of monolithic reactors applied here as a carrier consists of a vast number of small parallel channels, which build the flow passage for the exhaust gas. Figure 1.2 depicts an enlarged view on a coated monolith. As can be seen, the square channels are arranged in a honeycomb structure. Due to the coating process, the washcoat deposits more strongly in the corners than along the straight channel walls. The resulting shape of the channel is therefore rounded. The monoliths are called substrate and are nowadays mostly made of cordierite as the one in Figure 1.2. A second possible mechanical support are metal substrates, which are applied if the pressure drop is critical. They are composed of different layers of flat and corrugated steel foils, which are coiled into the desired shape [47, 48].
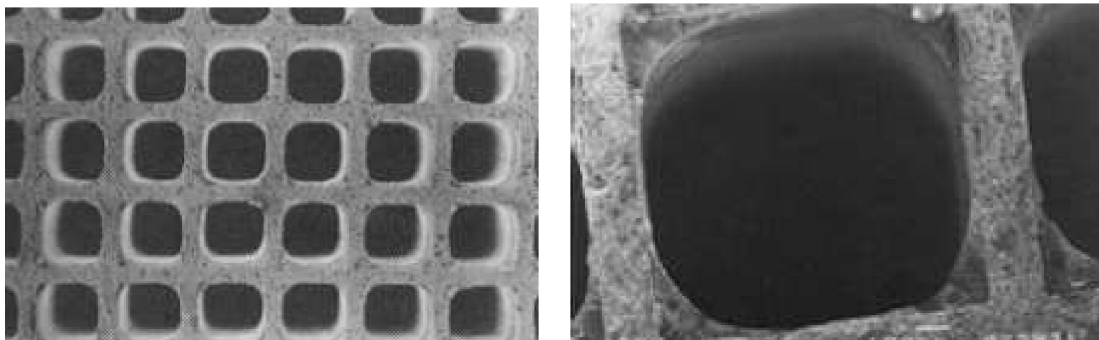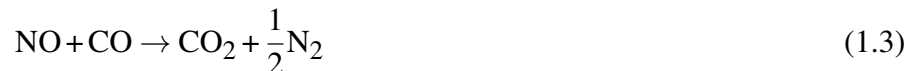

(a) Coated substrate matrice structure.   (b) Enlarged view of one channel.

Figure 1.2: A coated ceramic substrate taken from [49].

## 1.1.4 Catalytic Exhaust Gas Aftertreatment of Gasoline Engines

The reactions of the main pollutants, CO, HC and NO can be described by the following three global reaction pathways:

$$CO + \frac{1}{2}O_2 \rightarrow CO_2 \tag{1.1}$$

$$C_mH_n + (m + \frac{n}{4})O_2 \rightarrow mCO_2 + \frac{n}{2}H_2O \tag{1.2}$$

$$NO + CO \rightarrow CO_2 + \frac{1}{2}N_2 \tag{1.3}$$

For the TWC to simultaneously reduce all three species, the inlet feed needs to be in a narrow range around the stoichiometric point. If there is an excess of CO and HC (a rich inlet feed), the O_2 and NO is not sufficient to oxidize all of it. At lean conditions with oxygen and NO in excess, the NO conversion will decline. The stoichiometry is usually expressed with the air to fuel ratio λ

$$\lambda = \frac{\text{amount of air provided for fuel oxidation}}{\text{amount of air necesary for total fuel oxidation}} \quad . \tag{1.4}$$

However, the λ-value not only influences the reactions in the catalyst but also the combustion characteristics of the engine. Figure 1.3a qualitatively illustrates the engine out emissions at various λ-values. The NO emissions are highest around the stoichiometry point. CO and HC sharply increase under rich conditions. At λ-values above one, the oxygen content increases and all emissions decrease. The influence of the combustion's λ-value on conversions is shown in Figure 1.3. The high CO concentration at low λ-values poisons the catalyst and decreases the NO conversion as well. A minor conversion of HC and CO is possible at low λ-values due to steam reforming and the water-gas-shift reaction. As can be seen in Figure 1.3b, the homogeneous operation of the engine in a narrow range around a λ-value of 1 is essential to achieve a high conversion of pollutants in the catalyst at stationary warm operations.
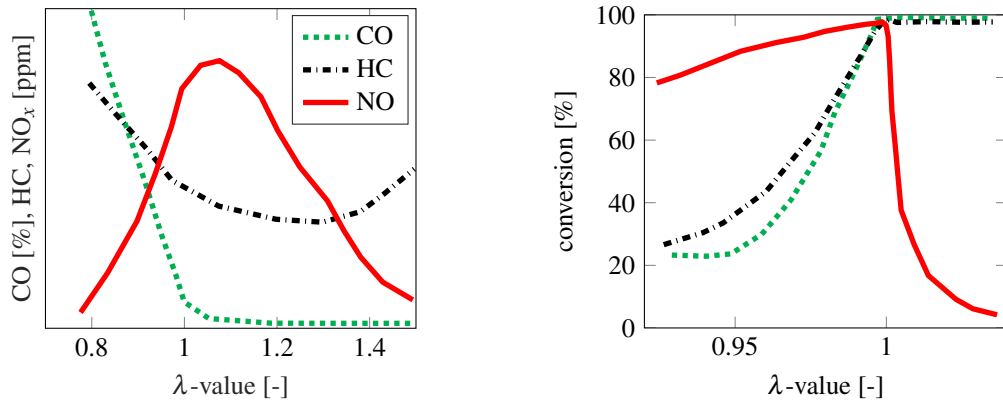
(a) Dependency of the emission on the λ-value (adapted from [50]).

(b) Dependency of the steady-state conversion on the λ-value (adapted from [15]).

Figure 1.3: Influence of the λ-value on the emissions and the conversion.

The highly dynamic operation of engines under practical driving conditions requires an air to fuel ratio control to achieve a stoichiometric operation of the engine. For this reason, cars are equipped with λ-sensors that can detect the air to fuel ratio by comparing the oxygen content of the exhaust gas and the ambient air. The scheme in Figure 1.4 depicts a typical positioning of λ-sensors. The wideband universal exhaust gas oxygen (UEGO) sensor measures the λ-value in a broad range. The engine adapts the fuel injection to meet the requested λ-setpoint according to this measurement. A second, more dynamic heated exhaust gas oxygen (HEGO) sensor detects if the mixture is lean or rich. Its value is applied to adjust the signal of the UEGO-sensor. To smooth small deviations in the λ-control as well as differences in the stoichiometry of the engine's cylinders, the catalysts have an oxygen storage. The cerium and zirconium oxides in the washcoat are oxidized at lean conditions and are reduced at rich conditions [51]. Thus, the catalysts (especially the second of the two bricks, see Figure 1.4) can buffer deviations from stoichiometric operations for short time interval.
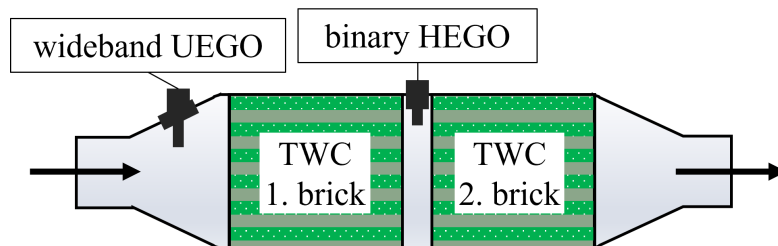

Figure 1.4: Schematic of the typical control loop for the exhaust gas stoichiometry.

1.2 Gasoline Particulate Filters

Increasingly stringent emission standards have prompted researchers in the area of engine exhaust emissions reduction to explore and develop technologies to significantly reduce emission levels from gasoline engines. Thus, next to the TWC a particulate filter was introduced to capture harmful aerosols. Previously, only diesel engines were equipped with a diesel particulate filter (DPF) [52–55]. But recent legislation forced the application of filters for direct-injection gasoline engines. Because of their better fuel economy and with it a reduction of CO_2 emissions, the market share of direct-injection gasoline engines is increasing [56, 57]. However, especially at transient cold start conditions or high velocity driving, the engine out particulate emissions are high [57–59]. Predominantly, for the early generation of these engines, the stratified combustion in combination with wetting of the piston and wall surfaces lead to an increase of emitted nanoparticles compared to port-fuel injection engines [60–64]. Due to their small size, nanoparticles are especially harmful [65, 66]. As a result, the European Union set a stringent particle number regulation [67]. To cope with this regulation and its counterpart in China, car makers introduced the gasoline particulate filter for gasoline engines [68–74]. Soon, the low particle mass limit in California will likely require the application of a filter in the US market as well [8, 75].

There were different concepts for the early diesel particulate filters, e.g. cylindrical cartridges or foam blocks / plates [76–78]. Nowadays, particulate filters are mainly extruded monoliths with square or hexagonal channels in a honeycomb structure [79, 80]. These channels are alternately plugged to force the fluid through the wall (see Figure 1.5). In the porous media, the particles are captured mainly through Brownian motion, interception or inertial deposition [81–85]. Other possible mechanism, e.g. sieving, are only of minor impact. The accumulated soot is then oxidized at fuel cut events during, e.g. highway driving, when the filter reaches a sufficient high temperature [74, 86].
An increase of catalytic volume compared to previous systems is necessary to ensure a sufficient conversion of gaseous pollutants under all possible driving cases (see 1.1.2). With the available space already limited by the filter, the integration of a three-way catalyst in the filter, resulting in a coated gasoline particulate filter (cGPF), helps to achieve the necessary conversion of pollutants in the available, predetermined space.

Similar to TWCs, the filter encounters a harsh environment in the automotive application regarding steep temperature gradients, high temperature peaks and exposition to water. There are five main requirements for particulate filters [88]:
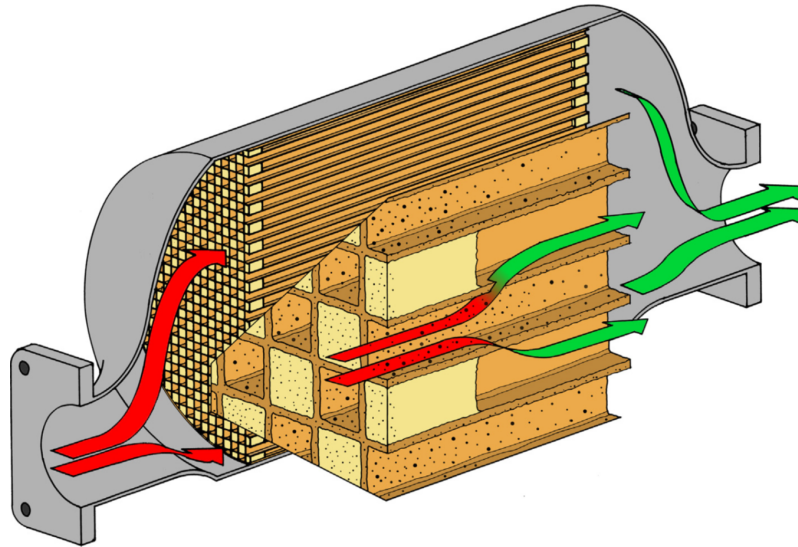
Figure 1.5: Schematic of a particulate filter taken from [87].

- *Filtration performance*: the filter should offer sufficient filtration performance to meet the regulatory standards at known engine out emissions.

- *Pressure drop*: a high pressure drop leads to more fuel consumption and less peak-power. Therefore, the pressure drop should be as low as possible.

- *Catalytic activity / coating possibility*: if the filter is coated then the catalytic activity and aging resistance should be as high as possible. Thus, in this case, the bare filter needs a high volumetric capacity to integrate washcoat.

- *Mechanical and thermo-mechanical robustness*: due to the harsh industrially relevant conditions, the filter needs to withstand the fast temperature gradients encountered at driving or during regeneration and the mechanical stress during the canning process.

- *Passive soot oxidation and soot mass limit*: the filter needs to withstand the exothermic peaks during severe regenerations and maximize the capability for passive soot oxidation.

To meet these requirements, different ceramics were proposed for GPFs, e.g. cordierite, aluminum titanate, silicon carbide, mullite or metall foams [30, 89–91]. However, due to the harsh operating conditions considering thermal shock resistance and the required low thermal mass, cordierite is the dominantly deployed material [92–94]. The monolith for TWCs are often made of this ceramic as well and it is known to not have a poisoning

effect on downstream catalysts or λ-sensors.

Beside the choice between a coated and an uncoated filter, the monolith is specified by its number of cells, wall thickness, porosity and pore size distribution. The latter is usually stated by the mean pore size (D50). Table 1.2 lists the specification range for typical filters.

Table 1.2: Specification range of typical GPFs [80, 86, 89, 90, 95]

	uncoated	coated
CPSI	200 - 300	300
wall thickness [mil]	6 - 12	8 - 12
porosity (prior to coating) [%]	40 - 60	60 - 70
mean pore size (prior to coating) [μm]	7 - 13	14 - 22

Next to the kind of filter, the placement in the exhaust gas system plays a vital role. A filter or a TWC can either be integrated close-coupled (CC) next to the turbocharger or in an underfloor (UF) position after the flex pipe. Additionally, a coated filter can be deployed. Figure 1.6 shows different possibilities to integrate a filter into the exhaust gas system. At close-coupled positions, the filter can be placed as first (CC1) or second (CC2) monolith. Naturally, an aftertreatment system with an uncoated filter in a CC1 position lacks the catalytic performance during the light-off. A close-coupled GPF will regenerate more often due to the higher temperature. If the filter is uncoated however, it will also be a heat sink which increases the time for catalysts downstream of the filter to reach light-off temperature.
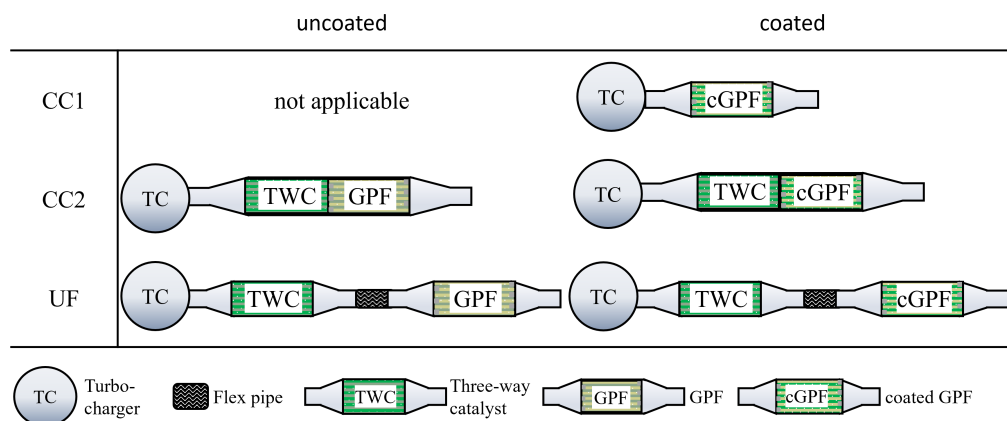

Figure 1.6: Possible exhaust gas aftertreatment architectures with particulate filters (additional possible underfloor catalysts are not shown).

cGPFs can be further distinguished in terms of the applied coating technology. Depending on the properties of the applied catalyst slurry and the washcoating method, the catalyst is either deposited in the wall or on the walls of either inlet or outlet channel [96, 97]. A mix of both, in-wall and on-wall, as well as an axial zoning is also possible depending on the washcoat loading. The interaction between the substrate and the washcoat is of great interest, since the final properties of the wall determine the filtration efficiency and pressure drop, which are crucial for the application of a filter. Also, the integration of a membrane on the inlet channel similar to an artificial ash layer in order to increase the filtration efficiency is possible [98, 99]. Figure 1.7 shows digital representations of a solely in-wall coated filter and one with a partial on-wall coating on the inlet channel. Here, the cordierite is presented in grey and the washcoat in yellow with streamlines colored by the local velocity magnitude.
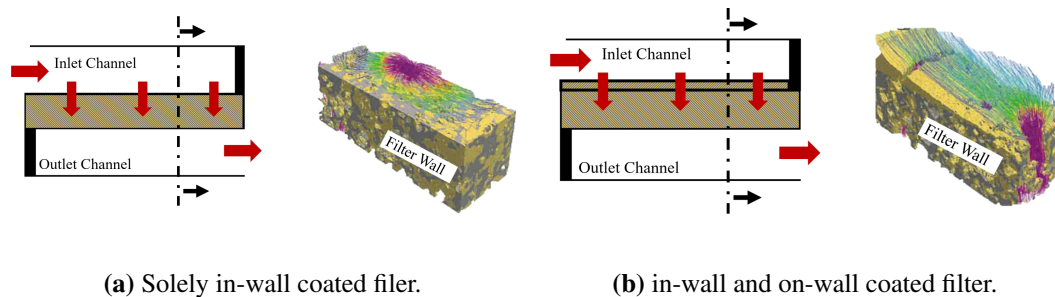

(a) Solely in-wall coated filer.

(b) in-wall and on-wall coated filter.

Figure 1.7: Schema and streamlines of representative pore scale 3D CFD calculations of a solely in-wall coated filter and a partially on-wall coated filter (reproduced from [100]).

1.3 Modeling of Coated Gasoline Particulate Filters

The experimental evaluation of aftertreatment systems with cGPF is time-consuming and expensive. Hardware that matches the later series production parts is only available at a late stage in the development process. Therefore, accurate models that can determine the performance of exhaust gas aftertreatment systems regarding the chemical conversion, filtration efficiency and pressure drop under practical driving conditions are necessary.
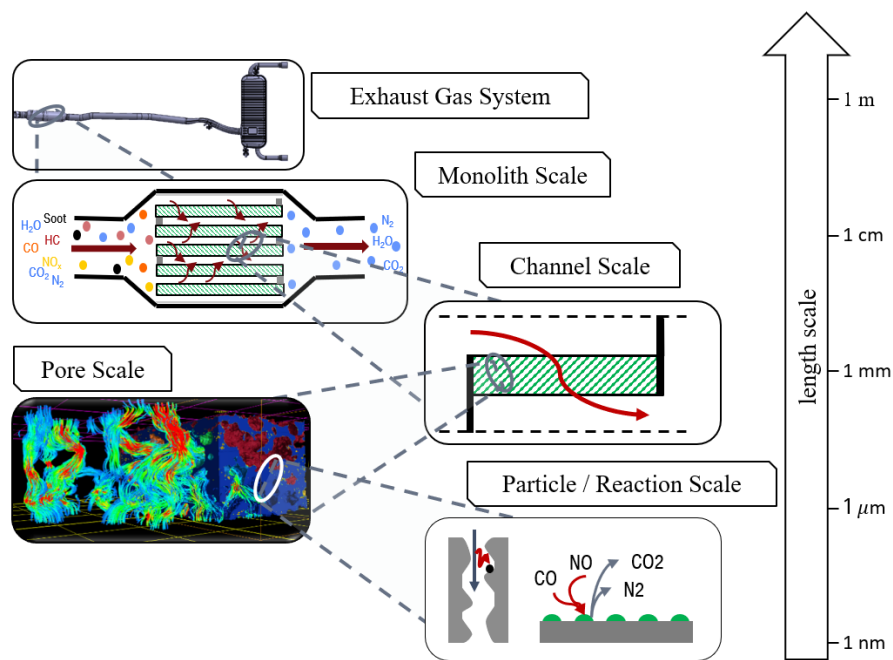
Figure 1.8: Size regimes in the exhaust gas aftertreatment design.

The predominant phenomena of filtration and chemical conversion are on a finer length scale than the monolith or the exhaust gas system as a whole. Figure 1.8 highlights the different scales with an in-wall coated GPF as example. In additions, highly transient driving scenarios are the key for system design but require a fine resolution of time. Thus, for the practical deployment, macroscopic, multiscale models with low computational costs are necessary. But, these models still need to address the physical and chemical processes with sufficient accuracy to allow a predictive evaluation of technologies and the interpretation of accompanying measurements.

1.3.1 Flowfield in Particulate Filters

Figure 1.9 shows a schematic of a 2D flow field in an inlet channel with two neighboring half outlet channels. After the exhaust gas contracts into the inlet channel, in most cases laminar flow develops in the inlet channel. Along the inlet channel, the velocity decreases as part of the fluid flows through the wall into the outlet channel. In contrast, the volume flow in the outlet channel increases due to the through-wall flow. On a simplified 1D level, there are five different contributions to the overall pressure loss in the filter which are marked with numbers. At first, the fluid contracts at the inlet channels's entrance (1). The second contribution is the wall friction in the inlet which decreases along the channel as the velocity sinks (2). The flow through the porous media is the third contribution to

the pressure drop (3). The friction in the outlet channel (4) and the expansion at the outlet (5) are the fourth and fifth contribution, respectively.
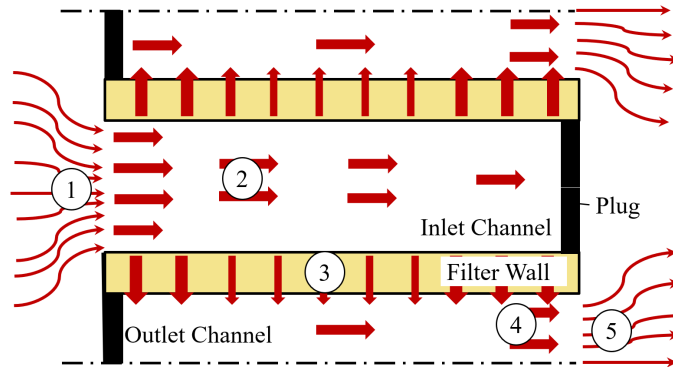

Figure 1.9: Schematic of the different contributions to the pressure drop of a GPF. (1) contraction (2) friction in the inlet channel (3) wall flow (4) friction in the outlet channel (5) expansion.

The expansion and contraction losses are only influenced by the incoming mass flow and the filter's open frontal area. The open frontal area is defined as sum of the cross-section areas of all inlet channel, thus the available part of the frontal area for the fluid to flow through. In contrast, the other contributions are strongly influenced by the length of the filter.

Figure 1.10 depicts the pressure drop of a filter substrate for different channel lengths. The pressure loss due to friction on the channel wall increases with the length. However, the through-wall velocity is decreasing with the filter length and with it the pressure drop due to the wall flow. In consequence, there is an optimal length with the lowest pressure drop, in this case, at approximately 100 mm. Since the pressure drop increases sharply at lower filter lengths and the length of filter plugs can differ during the production process and due to ash and soot depositions at the rear of the inlet channel, often a slightly longer filter length is applied. Therefore, in this work, all filters are 120 mm long.
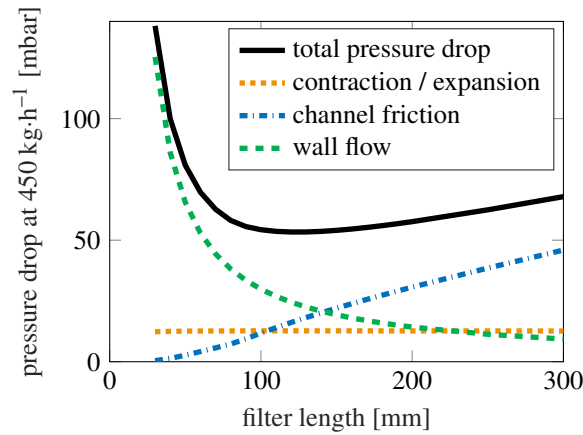
Figure 1.10: Pressure drop at $450 \, \text{kg·h}^{-1}$ and $800 \, ^\circ\text{C}$ for different filter lengths with a frontal area of $136 \, \text{cm}^2$.

1.3.2 Filtration Modeling

Filtration is defined as the process of separating dispersed particles from a dispersing fluid by means of a porous media [101]. Thus, filtration is a multiphase flow problem with the three phases particles, fluid and porous media. As a result, mostly the filtration efficiency, described by the fraction of particles deposited in the porous media (see Equation (1.5)), is of interest.

$$FE = 1 - \frac{c_{\text{particle}}^{\text{out}}}{c_{\text{particle}}^{\text{in}}} \tag{1.5}$$

Filtration models can be grouped in either microscopic, pore scale approaches with the particle trajectory resolved in the porous media by means of, e.g. lattice Boltzmann simulation (LBM) [102, 103], or macroscopic approaches with the porous media described by integral properties [104].

For general flow in porous media and accompanying filtration processes, there are numerous simulation works on pore scale. Tosco et al. [105] conducted single-phase flow simulations on synthetic porous media to extend the empirical Darcy-Forchheimer law. With a similar aim, Narsilio et al. [106] applied X-ray microtomography in order to calculate the hydraulic conductivity of porous media with a finite element approach. Long and co-workers [107, 108] modeled the filtration process via LBM CFD and thereby established new correlations for macroscopic approaches. Boccardo et al. [109] also studied the filtration process via pore scale CFD. Instead of LBM, they applied Eulerian

steady-state simulations and solved the corresponding advection–diffusion equations for the particles [109]. More specific studies with a focus on the pore scale modeling of GPFs and DPFs, however, are rare. Koči et al. [110] introduced the coupling of X-ray computed tomography (XRT) and LBM CFD in the GPF modeling. With this technique, Plachá et al. [87] established their pore scale filtration approach based on an Eulerian-Langrangian flow model. Their model matched the measured sensitivities of three differently coated GPFs well with the result that the partially on-wall coated filter had the highest filtration efficiency [87]. Belot et al. [103] also determined the filtration performance of cGPFs via pore scale simulations. Their numerical model relies on the reconstruction of XRT images, the computation of the flowfield via LBM CFD and lastly the prediction of the filtration efficiency by solving the Langevin equation [103].

Despite of their ability to gain access to detailed structures on a pore scale, these CFD models are, due to their numerical requirements and their focus on only a small part of the filter wall, still not applicable for simulations with a broader scope, e.g. driving cycle analysis or control-oriented modeling of filter behavior. Thus, usually macroscopic models with the so called unit-collector approach are applied. In this approach, the porous media is transferred into a bed of spheres with corresponding characteristics. As a result, it is possible to apply the flowfield solution derived by Kuwabara [111] or Happel [112] for creeping flow in a randomly packed bed of spheres. The collection efficiency of a single sphere can then be determined by solving the convection-diffusion equation. The most widely applied approach was proposed by Lee et al. [82]. They derived a single collector efficiency for two different filtration mechanism based on Kuwabara's flow model [111]. Lee et al. [82] treats particles as diffusion points under the assumption that they are small compared to unit collectors.

All macroscopic filtration models describe the filtration process with independent mechanisms. Figure 1.11 depicts the particle and fluid trajectory corresponding to the three main mechanisms. As the usual particle size in the exhaust gas stream of the here considered gasoline engines is below $200\,\text{nm}$ [62, 95, 113], diffusion is the dominant filtration mechanism. The Brownian motion of the fluid impacts nanoparticles enough that the particles do not follow the fluid anymore. The particle diffuses to the pore boundary and sticks there.

Large particles are not as much impacted by the Brownian motion of the surrounding fluid. Their trajectory does not deviate from the streamlines. They can be collected via the interception mechanism. The middle part of Figure 1.11 shows that the particles sticks
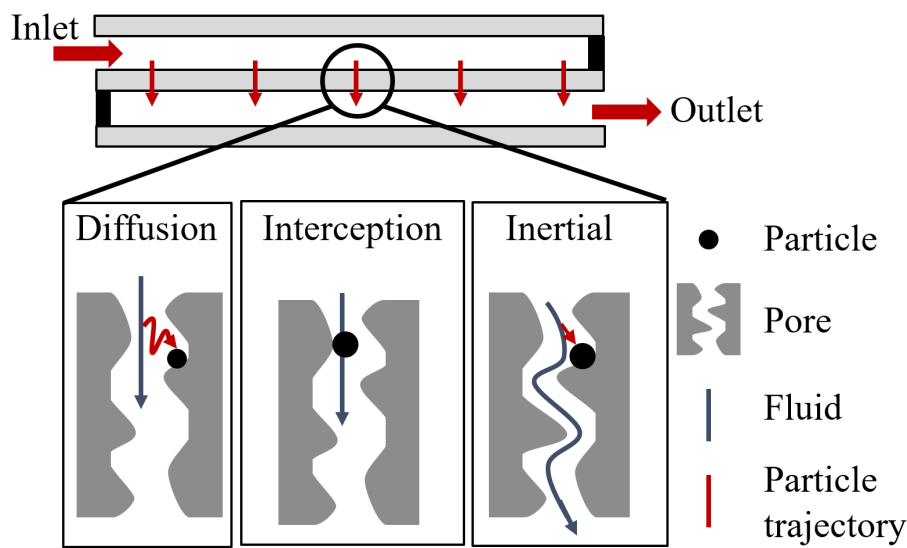
Figure 1.11: Schematic depiction of the three major filtration mechanisms in GPFs.

on the pore wall if the streamline brings the particle surface within the radius of the wall. The magnitude of the filtration efficiency due to this mechanism depends on the relative dimensions of the soot particle and the collector unit.

The last of the three considered mechanisms is the inertial deposition, shown on the right hand side of Figure 1.11. Due to the inability of particles to change their trajectory in order to follow the fluid, they leave the streamlines and are collected on the surface of the pores by impaction. The interaction of the particle mass, its velocity and the surrounding porous media characteristics determine the collection efficiency due to inertial deposition. Other possible filtration mechanisms, e.g. sieving, gravitational settling or electrostatic interception are assumed of minor impact in the considered system [114].

Especially for DPFs, homogeneous, simplified models achieve a high prediction quality [78, 84, 115–121]. However, Diesel engines emit a large particle mass which leads to a fast buildup of a soot layer on top of the filter wall. This layer enhances the filtration efficiency strongly. In consequence, the microstructure of the porous media is not so important for DPFs compared to GPFs. Also, Diesel engines have a lower exhaust gas temperature than gasoline engines. The DPF temperature is low enough that no spontaneous oxidation of the soot layer occurs. In contrast, an active regeneration is required if the pressure drop exceeds a critical limit at high soot loading. Therefore, the filtration efficiency of a fresh filter is not relevant for DPF applications. On the other hand, gasoline engines can easily heat the GPF above the necessary temperature for soot

oxidation. Therefore, the aim of GPF filtration models is to capture the fresh filtration efficiency as accurately as possible. Here, the correlations shown above based on the unit cell approach only utilize one averaged pore size and porosity to describe the porous media. The heterogeneous filtration model developed by Gong and co-workers [83, 85, 104, 122] incorporates a statistical description of the porous media within the classical filtration correlation based on the unit cell approach achieving a higher prediction quality for the fresh filtration.

1.3.3 Reaction Modeling

Ideally, chemical reactions are described on a molecular level by a set of quasi-elementary steps. These so called detailed reaction mechanisms can potentially predict the system's behavior outside the experimentally validated range, if all underlying phenomena are modeled correctly. However, for the simulation of automotive aftertreatment this approach is only used by few authors, e.g. [49, 123–125]. The majority of modeling works apply global kinetics [44–46, 126–130]. Detailed reactions mechanisms require the identification of all relevant reaction pathways on a detailed basis and the knowledge of the interaction with the surface structure as well as high computational effort. Global kinetics simplify the reaction networks into a descriptive subset of reaction pathways on a more macroscopic scale. Thus, it is necessary to calibrate the reaction mechanism for a catalyst formulation and the relevant external conditions. However, the number of parameters is lower compared to the detailed reaction mechanisms and the mechanisms are more easily transferred to different washcoat technologies.

Table 1.3 shows a reduced set of possible reaction pathways for three-way-catalysts without oxygen storage and the application in five representative mechanisms. The oxidation, water gas shift (WGS) and steam reforming (SR) reactions only differ in the considered hydrocarbon model species or the inclusion of the chemical equilibrium. In the NO_x and NH_3 reactions, the mechanisms differ more distinctively.

Starting with Voltz et al. [134], most models apply a Langmuir-Hinshelwood-Hougen-Watson (LHHW) rate equation. Compared to the alternatively often applied power law model (see Equation (1.6)), the LHHW type kinetic model has a better theoretical foundation and is therefore more robust for extrapolation.

$$r_j = A_j e^{-\frac{E_{A,j}}{R \cdot T}} \Pi_i C_i^{\alpha_j} \tag{1.6}$$

Table 1.3: Scheme of global reactions and the corresponding studies.

			Holder et al. [126]	Kwon et al. [131]	Tsinoglou et al. [132]	Ra-manathan et al. [44]	Mit-souridis et al. [133]
Oxidation	1	$CO + 0.5O_2 \rightarrow CO_2$	x	x	x	x	x
	2	$H_2 + 0.5O_2 \rightarrow H_2O$	x	x	x	x	x
	3	$C_3H_8 + 5O_2 \rightarrow 3CO_2 + 4H_2O$	x	-	x	x	-
	4	$C_3H_6 + 4.5O_2 \rightarrow 3CO_2 + 3H_2O$	x	x	x	x	x
	5	$CH_4 + 2O_2 \rightarrow CO_2 + 2H_2O$	x	-	-	-	x
WGS / SR	6	$CO + H_2O \rightarrow CO_2 + H_2$	x	-	x	-	-
	7	$CO + H_2O \rightleftharpoons CO_2 + H_2$	-	x	-	x	-
	8	$C_3H_8 + 3H_2O \rightarrow 3CO + 7H_2$	x	-	x	-	-
	9	$C_3H_6 + 3H_2O \rightarrow 3CO + 6H_2$	x	x	x	x	-
	10	$CH_4 + H_2O \rightarrow CO + 3H_2$	x	-	-	-	-
Reduction / SCR	11	$CO + NO \rightarrow CO_2 + 0.5N_2$	x	-	x	x	x
	12	$H_2 + NO \rightarrow H_2O + 0.5N_2$	-	x	x	x	x
	13	$C_3H_6 + 9NO \rightarrow 3CO_2 + 4.5\,N_2 + 3\,H_2O$	x	-	-	x	x
	14	$H_2 + 2NO \rightarrow H_2O + N_2O$	x	x	-	-	x
	15	$H_2 + N_2O \rightarrow H_2O + N_2$	x	-	-	-	x
	16	$CO + 2NO \rightarrow CO_2 + N_2O$	x	-	x	-	x
	17	$CO + N_2O \rightarrow CO_2 + N_2$	x	-	x	-	x
	18	$N_2 + 3H_2 \rightarrow 2NH_3$	-	x	-	-	-
	19	$2NH_3 + 1.5O_2 \rightarrow 2N_2 + 3H_2O$	-	x	-	-	-
	20	$2NH_3 + 2.5O_2 \rightarrow 2NO + 3H_2O$	-	x	-	-	-
	21	$2NH_3\ 2O_2 \rightarrow N_2O + 3H_2O$	-	x	-	-	-
	22	$2N_2O \rightarrow 2N_2 + O_2$	-	x	-	-	-
	23	$2NH_3 + 2NO + 0.5O_2 \rightarrow 2N_2 + 3H_2O$	-	x	-	-	-
	24	$NO + 2.5H_2 \rightarrow NH_3 + H_2O$	-	-	-	-	x
	25	$NO + 2.5CO + 1.5H_2O \rightarrow NH_3 + 2.5CO_2$	-	-	-	-	x
	26	$NH_3 + 1.5\,NO \rightarrow 2.5N_2 + 3H_2O$	-	-	-	-	x
	27	$2NH_3 \rightarrow N_2 + 3H_2$	-	-	-	-	-

LHHW models consider the adsorption on the catalyst surface. Under the assumptions that the active sites are equally distributed, that the heat of adsorption is independent of the coverage and that the rate of adsorption is linearly dependent on the number of vacant active sites, the Langmuir adsorption model describes the adsorption of a species A in a mixture as

$$\theta_A = \frac{K_{eq,A} \cdot p_A}{1 + \Sigma_{i=1}^{n} K_{eq,i} \cdot p_i} \qquad . \tag{1.7}$$

Here, K_{eq} describes the equilibrium constant of the adsorption-desorption process, p the partial pressure of a species i and θ_A is the surface coverage of species A. The coverage of all species and the fraction of vacant active sites sum up to one. For the reaction scheme,

$$A + B \rightarrow C + D \tag{1.8}$$

it is assumed that all educts and products adsorb to identical sites on the surface and the surface reaction is the rate determining step. The adsorption and desorption are in equilibrium. Applying Equation (1.7), the reaction rate can be expressed as follows

$$r_j = \frac{A_j e^{-\frac{E_{A,j}}{R \cdot T}} \cdot K_A \cdot K_B \cdot p_a \cdot p_B}{(1 + K_A \cdot p_A + K_B \cdot p_B + K_C \cdot p_c + K_D \cdot p_D)^2} \qquad . \tag{1.9}$$

The application of the LHHW kinetics as in Equation (1.9) requires the partial pressure of all model species in every reaction rate equation. Since the resulting system is numerically difficult to solve, and many species, e.g. CO_2, H_2O, have almost constant partial pressures under practical conditions, most studies simplify the rate equations. Except for the work of Kwon et al. [131] and Kang et al. [135], who considered the competitive adsorption of most species in every reaction rate, the majority follows the work of Voltz et al. [134] for the modeling of three-way catalysts. Here, the reaction rate expression contains an inhibition factor G.

$$r_j = \frac{A_j e^{-\frac{E_{A,j}}{R \cdot T}} p_A \cdot p_B}{G} \tag{1.10}$$

Voltz et al. [134] defined the inhibition as follows

$$G = (1 + K_{CO}[CO] + K_{HC}[HC])^2 \cdot (1 + K_{emp}([CO] \cdot [HC])^2) \cdot (1 + K_{NO}[NO]^{0.7}) \qquad . \tag{1.11}$$

The first part of Equation (1.11) is based on the LHHW model but only CO and HC are considered to adsorb. The middle part with the factor K_{emp}, was added by Voltz et al. [134] as an empirical addition to increase the CO and HC inhibition under strongly

rich conditions. Most models in literature still include this term. However, their resulting calibration led to so low values that the impact is negligible [44, 130]. The NO dependent term was introduced to capture the inhibition due to NO as non-reacting species. Since Voltz et al. [134] examined Pt catalysis with a strong focus on oxidation reactions, they considered NO as inert. The exponent was changed to one by some authors [45, 130] as the addition of NO reduction reactions requires adaption of Equation (1.11) if the NO concentration approaches zero. Later on, additional terms were introduced for different HC species or the inhibition of HC oxidation by excess oxygen [126, 132].

1.4 Scope of this Work

Coated gasoline particulate filters (cPGF) are a key element of future emission concepts. Their complex interaction of washcoat and filter substrate joint with the more stringent regulations that future cars must meet under a variety of operating conditions require a deep understanding of the underlying phenomena. The sizing and the substrate properties strongly influence the performance of the filter but also its costs. The aim of this work is to develop modeling approaches for cGPFs which allow a predictive evaluation of pressure drop, filtration and catalytic conversion under highly transient conditions. As a calibration and validation basis, experiments on dynamic engine test benches with industrially relevant full-sized samples are applied. With the help of pore-scale computed tomography measurements, the porous media is described in its integral properties. To address the specific operating conditions of GPFs, new modeling methods are incorporated into a transient modeling framework in Matlab [136]. The resulting model is then applied to determine optimal coating parameters. Figure 1.12 depicts the taken steps to develop and apply the simulation model that are grouped into the following chapters:

Chapter 2 presents a heterogeneous filtration model with a new approach for inertial deposition. The simulation can reliably predict the impact of pore size distribution and geometrical properties on the filtration at a dynamic cold start. This chapter was published in similar form as R. Walter, J. Neumann, O. Hinrichsen, "Extended Model for Filtration in Gasoline Particulate Filters under Practical Driving Conditions", **Environ. Sci. Technol. 2020** 54 (15), S. 9285–9294. DOI:10.1021/acs.est.0c02487.

Chapter 3 extends the heterogeneous filtration model to coated filters. The necessary pore scale properties are gathered via high resolution X-ray computed tomography. The simulation can sucessfully replicate the impact of washcoating on pressure drop and

filtration efficiency. The chapter was published in similar form as R. Walter, J. Neumann, A. Velroyen, O. Hinrichsen, "Applying 3D X-ray Microscopy to Model Coated Gasoline Particulate Filters under Practical Driving Conditions", **Environ. Sci. Technol.** 2022 56 (17), S. 12014-12023. DOI:10.1021/acs.est.2c01244.

Chapter 4 introduces a novel global reaction mechanism for three-way catalyst coated filters. Due to the vast variety of quasi steady-state calibration data, the model delivers a high quality prediction. With this approach it is possible to reproduce the behavior of a fresh cGPF in a driving cycle without a similar measurement in the calibration data set, proving the possibility to extrapolate with the presented approach. This chapter was published in similar form as R. Walter, J. Neumann, O. Hinrichsen, "Modeling the Catalytic Performance of Coated Gasoline Particulate Filters under Various Operating Conditions" **Ind. Eng. Chem. Res.** 2021 60 (47), S. 16993–17005. DOI:10.1021/acs.iecr.1c03631.

Chapter 5 applies the developed kinetics on a modeling study to evaluate different ways of coating filters. The comparison of zoning concepts demonstrates that in-wall as well as on-wall filters can perform better if axial zoning is utilized. The chapter was published in similar form as R. Walter, J. Neumann, O. Hinrichsen "A model-based analysis of washcoat distribution on zoned coated gasoline particulate filters" **Chem. Eng. J.** 2022 441, S. 135615. DOI: 10.1016/j.cej.2022.135615.

Chapter 6 summarizes the obtained findings and draws the conclusion of this work. Additionally, some suggestions for further investigation and perspective application outside the shown context are outlined.
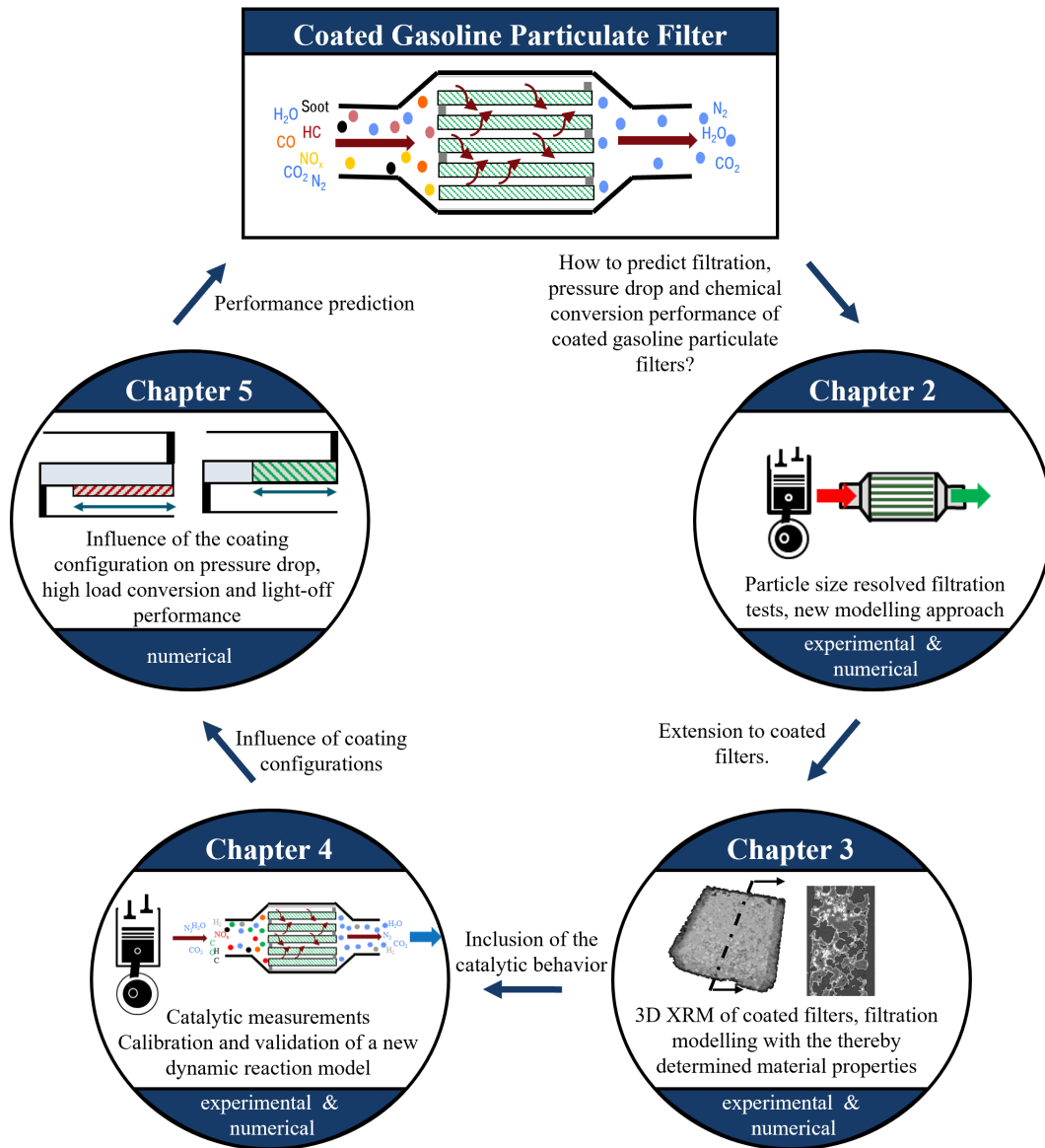
Figure 1.12: Graphical outline of the thesis. In order to develop a model of the transient behavior of cGPFs, the filtration characteristics of an uncoated filter are studied in a first step. Then, the model is incrementally extended by the introduction of coated filters, a reaction mechanism and the influence of coating parameters.

2 Extended Model for Filtration in Gasoline Particulate Filters under Practical Driving Conditions

Summary of the publication:

In order to reliably predict the particle number filtration of Gasoline Particulate Filters (GPF) under practical driving conditions, an extension to established filtration models is developed. For the validation of this approach and in order to close a gap of available measurement data at high space velocity in the literature, the particle-size resolved fresh filtration efficiency of seven different cordierite filters is determined experimentally. Moreover, the experiments on a dynamic engine test bench focus on the impact of the pore size distribution and the filter wall thickness under steady-state as well as transient, cold-start conditions. In order to model all trends observed, a new correlation for the particle collection due to inertial deposition is proposed and embedded in a heterogenous multiscale model framework for a GPF. The presented approach can predict all trends observed in the measurements, including a stabilization of the filtration efficiency with increasing space velocities above a certain level. A comparison of several modeling approaches reveals the partly different behavior at varying space velocities for the here presented model as well as for established filtration models.
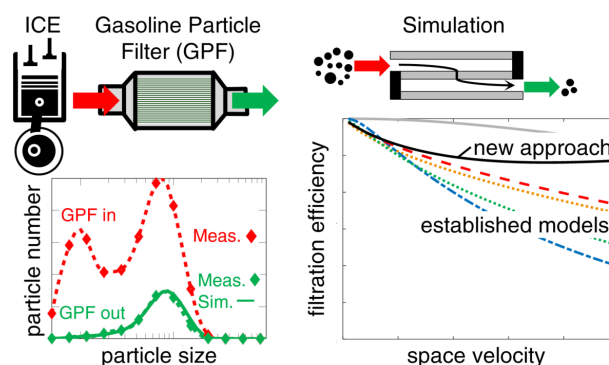
Individual Contributions of the Candidate

The contribution of the candidate to this publication included the conduction and analysis of the experiments as well as the conception and implementation of the model. Also the manuscript was written by the candidate. Jens Neumann help planning the experiments and supervised the modeling process. Prof. Olaf Hinrichsen helped reviewing and editing the manuscript.

2.1 Introduction

The worldwide increasingly stringent legislation regarding the emissions of particles of gasoline engines requires a reduction of the particle emissions [67, 70]. One way to achieve this reduction is the usage of Gasoline Particulate Filters (GPF) in exhaust gas aftertreatment [67, 68]. The basic technology is already established for Diesel engines that are equipped with Diesel Particulate Filters (DPF) for several years now. Both filter types exist of a wall-flow device consisting of square channels plugged at alternate ends in adjacent channels such that the exhaust gas mixture passes through the walls of a porous substrate [79, 80].

The main difference between GPF and DPF are the operating conditions. Diesel engines emit a relatively high particle mass that leads to a fast buildup of a soot layer on top of the filter wall. This soot cake captures most of the particle emissions [80, 117]. The exhaust gas temperature of Diesel engines is low enough that no spontaneous oxidation of the particulate matter on the filter wall occurs. As a result of this, an active regeneration of the DPF is triggered when the filter's backpressure exceeds a critical point. Most modeling tools for DPF's aim to reproduce the increasing filtration efficiency and backpressure as the soot loading rises [84, 119, 137]. The strategy then is to reduce the soot buildup enough for lower backpressure without reducing the filtration efficiency. Thus, the filtration efficiency of a fresh filter is not as relevant for DPF applications. On the other hand, gasoline engines easily reach exhaust gas temperatures that suffice for spontaneous soot oxidation under real-world conditions [86]. Therefore, models for system design of gasoline engine's exhaust gas aftertreatment should aim to capture the fresh filtration efficiency as accurately as possible since it is possible to have a soot-free GPF in almost any driving scenario. Next to the higher importance of fresh filtration, the higher space velocity due to hotter exhaust gas distinguishes the particulate aftertreatment of Diesel and gasoline engines.

Additionally, the introduction of Real Driving Emission (RDE) tests enforces the validation of the filtration performance in a variety of driving scenarios. These tests include operating conditions with high mass flow and temperature that exceed conditions in conventional test cycles [19, 138]. As a result of a literature survey, the experimental operating conditions in terms of temperature and space velocity that are used for model validation of existing filtration models are shown in Table 2.1. If not provided by the authors, the space velocity is determined by given face velocities or mass flows with densities derived by the ideal gas law. This comparison clearly shows a lack of model

validation data for high space velocities and high temperatures.

The present work aims to present a framework for a GPF filtration model that can reproduce the filter behavior under realistic operating conditions, which exceed the validation basis of current models shown in Table 2.1. For this purpose, we compare different existing approaches to calculate the fresh filtration efficiency of a GPF. As a novel aspect, the role of the inertia term inside the filtration model is addressed with respect to the GPF operating conditions. Therefore, particle-size resolved measurements were conducted on gasoline engine test benches using several filters and different test conditions. In addition to steady-state operating conditions, an acceleration with a cold engine validates the model for dynamic cycles. These measurements build an experimental validation basis for filtration models with high volume flow rates and temperatures typical for gasoline engines.

Table 2.1: Comparison of experiments used for model validation in literature.

Source	Used for model validation by	Particle generation	T_{max} [°C]	SV [s^{-1}]
[119]	Tandon et al. [119]	Particle generator	300	6
[139]	Konstandopoulos et al. [140]	Diesel engine	113	14
[140]	Konstandopoulos et al. [140]	Diesel engine	353	81
[54]	Konstandopoulos et al. [140]	Diesel engine	210	39
[78]	Konstandopoulos et al. [78]	Diesel engine	260	14
[141]	Serrano et al. [84]	Diesel engine	300	18
[142]	Serrano et al. [84]	Diesel engine	260	6
[143]	Serrano et al. [84], Gong et al. [83]	Particle generator	-	24
[83]	Serrano et al. [84], Gong et al. [83]	Particle generator	175	0.4
[116]	Gong et al. [83]	Particle generator	20	82
[116]	Ohara et al. [116]	Particle generator	20	328
[62]	Gong et al. [122]	1 cyl. gasoline engine	398	28

2.2 Numerical Methods

2.2.1 Filtration Modeling

2.2.1.1 Existing Approaches

There are numerous methods to reproduce the behavior of filters for exhaust gas aftertreatment[83, 84, 116, 119, 140]. A 2D- or 3D-CFD particle-scale simulation using the Lattice-Boltzmann Method can help to understand the local particle movement [102, 144]. To avoid the high computational expense of this approach, Korneev et al. used 2D-CFD to solve the channel flow and advection-reaction equations to model the filtration. However, at their current stage, the filtration model is not dependent on the filter structure or operating conditions [145]. Nevertheless, 1D or 1D+1D models are still mostly used for filtration simulation due to their fast computation time and sufficient accuracy [117, 146].

Starting with Konstandopoulos et al. [140], a series of unit collector models for the filtration in wall-flow filters were published and validated using either engine test benches or particulate generators. The description of the porous media as a packed bed of spheres with the same hydrodynamic diameter as the pore network build the basis for all these models. This assumption allows predicting the collection efficiency η_{total} of particles on a single sphere (unit collector) with the diameter d_c, that is then integrated across the filter wall. Equation 2.1 expresses the resulting filtration efficiency due to the contribution of each unit collector in a filter wall with the thickness th_w and the porosity ε as:

$$FE = 1 - exp(-\frac{3(1-\varepsilon)}{2\varepsilon}\frac{\eta_{total} \cdot th_w}{d_c}) \quad . \tag{2.1}$$

Three main mechanisms contribute to the collection efficiency: Brownian diffusion η_D, direct interception η_R and inertial deposition η_I [80, 83, 84]. Other mechanisms, e.g. sieving, are considered of minor impact. Assuming that all mechanism are independent of each other, the resulting collection efficiency is expressed as:

$$\eta_{total} = 1 - (1-\eta_D) \cdot (1-\eta_R) \cdot (1-\eta_I) \quad . \tag{2.2}$$

Konstandopoulos et al. [140] applied the correlation for diffusion and interception, derived by Lee et al. [82] for a randomly packed bed of spheres and Stokes flow regime on a ceramic filter substrate. Their work set the basis for most DPF and GPF modeling approaches. An axial discretization of the channel extended the model [120] to represent

the difference in velocity along the channel wall (1D+1D). Afterwards, many authors tried to improve the model fit with additional correlations and methods to calculate the enhanced filtration efficiency due to soot deposition in the filter [78, 119]. Only Ohara et al. [116] applied a different set of correlations for diffusion and interception. They employed empirically determined correlation for the collection efficiency of Otani et al. [81].

Approaches that describe the filter's micro-structure only by the mean pore size (MPS) and the porosity are accurate for the operating conditions of DPF's. There, the soot layer enhances the filtration performance enough to keep the filtration almost independent of the microstructure. On the other hand, the deep bed filtration of a clean GPF is very sensitive to the microstructure of the filter [83, 147, 148]. Therefore, Gong et al. [83] developed a heterogeneous model that includes a pore size distribution to reproduce the deep bed filtration behavior.

2.2.1.2 Used Approach

Brownian Diffusion
The simulations in this work utilizes the correlations of Lee et al. [82], who analytically solved the convection and diffusion of particles in a packed bed of spheres. Equation 2.3 expresses the the collection efficiency due to diffusion as:

$$\eta_D = 2 \left(\frac{3\pi}{4} \right)^{\frac{2}{3}} \left(\frac{\varepsilon}{K(\varepsilon)} \right)^{\frac{1}{3}} \cdot Pe^{-\frac{2}{3}} \tag{2.3}$$

with the Peclet number *Pe* defined as:

$$Pe = \frac{U_i \cdot d_c}{D_D} \quad . \tag{2.4}$$

Here U_i represents the interstitial velocity, d_c is the respective unit collector size and D_D the particle diffusion coefficient. $K(\varepsilon)$ is Kuwabara's hydrodynamic factor [111], that is given by Equation 2.5.

$$K(\varepsilon) = 1 - \frac{9}{5}(1-\varepsilon)^{\frac{1}{3}} + (1-\varepsilon) - \frac{1}{5}(1-\varepsilon)^2 \tag{2.5}$$

Direct Interception
If the fluid transports a particle within the radius of the unit collector's surface, the particle

collection is named interception. Again, the established correlation of Lee et al. [82] is used

$$\eta_R = \frac{3(1-\varepsilon)}{2K(\varepsilon)} \cdot \frac{N_R^2}{(1+N_R)^2} \qquad (2.6)$$

with the interception parameter N_R defined as the ratio between particle and unit collector size:

$$N_R = \frac{d_p}{d_{c,i}} \quad . \qquad (2.7)$$

Inertial Deposition

The inertia mechanism of particulate capture describes the inability of particles to follow the streamlines of the gas due to their own inertia. The mechanism can be related to the Stokes number St, that is defined as the ratio between the particle relaxation or stopping time and its residence time [149]. Hereby the Stokes-Cunningham factor (SCF) corrects the drag force of small particles:

$$St = \frac{1}{9}SCF\frac{\rho_{soot,eff} \cdot U_i \cdot d_p^2}{\mu \cdot d_c} \quad . \qquad (2.8)$$

$\rho_{soot,eff}$ describes the density of an ideal spherical particle with the mobility diameter as particle size. In this work $\rho_{soot,eff}$ is assumed constant at $800\,\text{kg/m}^3$, because for particles of relevant size the density does not have a strong dependency on the diameter [113].
Gal et al. [150], D'Ottavio et al. [151] and Otani et al. [81] each introduced an effective Stokes number St_{eff} to reproduce the influence of the Reynolds number and the porosity on filtration. Otani et al. [81] and Gal et al. [150] proposed a correction factor based on Ergun's equation to correct the Stokes number, whereas D'Ottavio et al. [151] utilized Happel's hydrodynamic factor. Similarly to the work of D'Ottavio et al. [151], we are using Kuwabara's hydrodynamic factor $K(\varepsilon)$, since this flow field calculation is employed by all other collection efficiency correlations as well. Applying Kuwabara's hydrodynamic factor leads to the following definition of the effective Stokes number St_{eff}:

$$St_{eff} = St \cdot (1 + \frac{Re}{K(\varepsilon)}) \quad . \qquad (2.9)$$

The resulting correlation for the collection efficiency due to inertia η_I, defined in Equation 2.10, follows the same form as in Otani et al., Rosner et al., D'Ottavio et al. [81, 149, 151] with the experimentally determined coefficients a and b

$$\eta_I = \frac{St_{eff}^a}{(b + St_{eff})^a} \quad . \tag{2.10}$$

There are other approaches available in literature which show an increase of filtration efficiency with increasing fluid velocity. Otani et al. [81] modeled the diffusion with a Reynolds number dependent coefficient of the Peclet number (see Equation 2.3) instead of the constant one. Kirsh et al. [152] proposed a dramatically increased collection efficiency at Reynolds numbers larger than one due to the effect of interception. Long et al. [107] introduced new correlations for diffusion, interception, and inertial deposition of particles based on Lattice-Boltzmann simulations. The correlations for the collection efficiencies were, in part, chosen to the best match of available measurements of filters under automotive conditions. Also, the underlying fundamentals are already validated against lab-scale measurements [83].

Pore Size Distribution
The model utilizes a pore size distribution according to Gong et al. [83]. The pore size distribution is transformed into a probability density function (*pdf*) using a log-normal fit. Afterwards, by applying Equation 2.11, the *pdf* of the corresponding unit collectors is determined:

$$pdf_{d_c} = \frac{2\varepsilon}{3 \cdot (1 - \varepsilon)} \cdot pdf_{d_{pore}} \quad . \tag{2.11}$$

The collection efficiency is first calculated for each unit collector size and then combined using a relative area approach

$$\eta_{total}(d_p) = \frac{\int \eta_{total}(d_c, d_p) \cdot d_c^2 \cdot pdf_{d_c} \quad d(d_c)}{l_{d_c}^2} \tag{2.12}$$

with l_{d_c} as the root of the mean area:

$$l_{d_c} = (\int pdf_{d_c} \cdot d_c^2 \quad d(d_c))^{\frac{1}{2}} \quad . \tag{2.13}$$

2.2.2 Filter Model

The filter model used in this study solves the governing equations for the momentum and enthalpy transport along a representative inlet - and outlet channel pair. According to a 1D+1D approach, one-dimensional temperature and velocity profiles are calculated along the channel length [120, 133]. Thereby, the channel wall is divided into slabs for more detailed temperature profiles in case of transient simulation. Note that in an a priori grid sensitivity study, a discretization of 100 axial and three wall elements yields grid-independent results. For all simulations presented here, the x-coordinate is assigned as radial direction and the z-coordinate as axial direction.

The channel velocity v_j is determined by Equation 2.14 [153].

$$\frac{dp_j}{dz} = -\beta \frac{d(\rho v_j^2)}{dz} - 2\frac{\mu}{D_j^2} \cdot C_f(Re_w) \cdot v_j \tag{2.14}$$

The coefficient β and the friction coefficient C_f are interpolated using the tables provided by Bissett et al. [153]. The wall Reynolds number Re_w has an upper bound of three. As recommended by Bissett et al. [153], for Re_w greater than three the table lookup delivers the value for $Re_w = 3$. These authors suggested this upper bond, since higher Re_w generated an unphysical behavior and no fully developed solution in their detailed calculation was possible. Cooper et al. [154] compared the calculation of Bissett et al. [153] with magnetic resonance imaging measurements of the gas flow in a filter. Despite a large error for the friction factor at the front of the inlet channel due to the non-developed flow at high Reynolds numbers, the model prediction for the axial wall velocity profile is in good agreement with the measurements [154].

The channel velocity v_j is calculated using the continuity equation:

$$D_j^2 \frac{d\rho v_j}{dz} = (-1)^j \cdot 4D_j \cdot \rho v_w \tag{2.15}$$

with the index j as 1 for the inlet channel and 2 for the outlet channel. The channel pair is coupled using Darcy's law without Forchheimer's extension:

$$\Delta p = \frac{\mu \cdot v_w}{k_w} \cdot th_w \quad . \tag{2.16}$$

Hereby, the permeability k_w is fitted to pressure drop measurements for each filter and is supplied in the supporting information for each filter. The temperature of the gas phase in the channel is assumed as quasi-steady according to Equation 2.17.

$$c_p \rho_j v_j \frac{dT_j}{dz} = \frac{4}{D_j} \cdot (\alpha_j + (-1)^j \cdot c_p \rho v_w) \cdot (T_w - T_j) \quad (2.17)$$

The heat transfer coefficient α is derived via a Nusselt correlation of Bissett et al. [153]. The porous media is assumed as homogeneous, and the ideal gas law is used. All substance data are calculated with correlations from [155]. The temperature of the wall T_w is calculated using the enthalpy balance with axial heat conduction:

$$\rho_s c_s \cdot \frac{dT_w}{dt} = \lambda_s \cdot \frac{d^2 T_w}{dz^2} + H_{conv} + H_w \quad (2.18)$$

$$\text{with} \quad H_{conv} = \alpha_1 \cdot \frac{4}{D_1} \cdot (T_1 - T_w) + \alpha_2 \cdot \frac{4}{D_2} \cdot (T_2 - T_w)$$

$$\text{and} \quad H_w = \frac{4}{D_1} \rho_1 \cdot v_{w,1} \cdot c_{p,1}(T_1 - T_w) - \frac{4}{D_2} \rho_2 \cdot v_{w,2} \cdot c_{p,2}(T_2 - T_w) \quad .$$

Here again, the index 1 stands for the inlet channel and 2 for the outlet channel. The object oriented model is implemented in Matlab using ode15s and bvp4c to solve differential equations [136].

2.3 Experimental

2.3.1 Setup

A dynamic engine test bench equipped with a direct injection spark ignition gasoline research engine is used for all measurements in this study. The main technologies are exhaust gas turbocharging, a fully variable valvetrain, and gasoline direct injection with homogeneous operation. The four cylinder engine has a displacement volume of $1998 \, \text{cm}^3$ and utilizes a 350 bar injection system [156]. Figure 2.1 shows a schematic of the measurement setup. The GPF placement, approximately 2 m downstream of the close-coupled catalyst, aims to resemble an underfloor position with a defined, idealized inflow to minimize effects of flow maldistribution across the filter's front face.

Particles are measured using a Cambustion DMS500 particulate analyzer. The device determines the electrical mobility of beforehand charged particles in parallel using a high
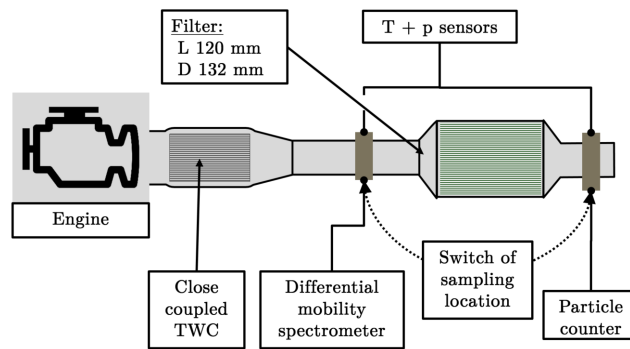
Figure 2.1: Measurement setup.

voltage electrode surrounded by 22 grounded electrometers [157]. Thus, the DMS500 allows the transient measurement of the particle size-resolved number concentrations. An additional particle counter (Horiba MEXA 2100 SPCS) is placed either downstream or upstream of the GPF. The analyzer utilizes laser scattering condensation particle counting with a built-in cyclone [158]. Therefore, only particles above 23 nm are measured. The highly automated engine test bench allows the usage of the same measurement device for the calculation of the filtration efficiency. For this, the sampling locations for the particle analyzers are switched during repetitive measurements. The engine is fueled with standard gasoline (ROZ95 E10).

Before each measurement point, an in-situ regeneration procedure, using a lean operation of the combustion engine as well as several fuel cuts, guarantees a soot-free filter. For the steady-state experiments, the engine runs at operating temperature of the corresponding load and speed settings. Since the steady-state experiments showed a high reproducibility in a preliminary test, these experiments are not repeated. A preconditioning process achieves stable starting conditions before each measurement of a driving maneuver. This process cools the engine and its periphery down until a standardized set of temperatures (engine oil and coolant temperature, the temperature at the filter's inlet) is reached. All dynamic measurements are repeated four times for each sampling location. During all filtration experiments the engines operates stoichiometrically, thus the oxygen content in the exhaust gas is not sufficient for a partial oxidation of the particles.

2.3.2 Used Filters

For model validation, seven different uncoated cordierite filters are tested. All these research samples have the same diameter of 132 mm and a length of 120 mm. The pore

size distribution is fitted to a log-normal distribution using the $d10$, MPS ($d50$) and $d90$ values obtained by mercury intrusion porosimetry. Here, the MPS is set as median, and the fitting procedure iterates the variance to achieve the best fit with the measured $d10$ and $d90$ values. The result is a variance of $120\,\mu m$ for the filters with MPS $12\,\mu m$ and $40\,\mu m$ for all other filters. Table 2.2 shows the specification of the two base filters GPF A and GPF B as well as the five adaptions of GPF B used in the later sensitivity study. These adaptions are covering variations of the wall thickness and the mean pore size. Within the two variations, all other filter characteristics (i.e. porosity, cell density) are similar to the properties of GPF B.

Table 2.2: Filter characteristics for substrates used in this study.

	GPF A	**GPF B**	**Adaptions of GPF B**				
			MPS7	MPS8 / WT8	MPS12	WT10	WT12
Porosity [-]	50%	55%	55%	55%	55%	55%	55%
Wall thickness [mil]	6	8	8	8	8	10	12
Cell density [cpsi]	200	200	200	200	200	200	200
MPS [μm]	12	8	7	8	12	8	8

The permeability for the simulation is tuned to fit pressure drop data at the engine test bench. The used values are listed in Table 2.3.

Table 2.3: Tuned permeabilities used for the channel scale flow field calculation

Filter	**Permeability** $[\mu m^2]$
GPF A	0.83
GPF B	0.57
GPF B - MPS7	0.53
GPF B - MPS8 / WT8	0.57
GPF B - MPS11	1.5
GPF B - WT10	0.42
GPF B - WT12	0.46

2.4 Results and Discussion

2.4.1 Steady State Filtration

As described above, there is a lack of filtration experiments with high flow velocity and temperature. Therefore, we have conducted a set of steady-state experiments with rising

temperature and space velocity. The utilized engine conditions are typically found during dynamic driving operations. The result was used to calibrate the inertia coefficients a,b of Equation 2.10. These coefficients are then held constant in all simulations in this study. The best fit to the tested filters GPF A and GPF B was obtained with $a = 0.7817$ and $b = 2.4363$. Next to these two coefficients, only the permeability, which is detailed in the supporting information, is calibrated to match backpressure and wall-flow behavior for each filter. All other input parameters are either measured inlet conditions, e.g. temperature, or properties of the filter.

(a) *SV*: 90 s^{-1}, T: 715 °C

(b) *SV*:170 s^{-1}, T: 790 °C

(c) *SV*: 180 s^{-1}, T: 780 °C

(d) *SV*: 215 s^{-1}, T: 810 °C
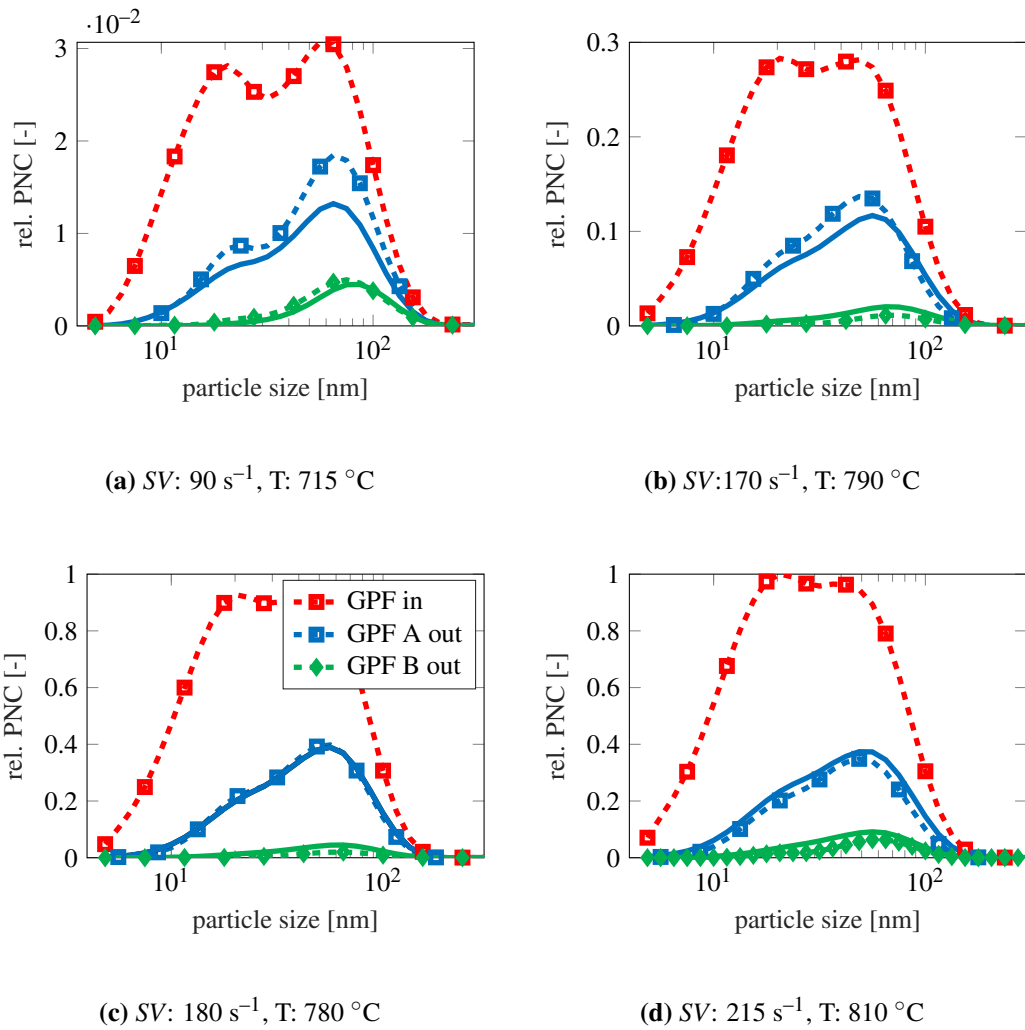
Figure 2.2: Particle number concentration normalized to the highest upstream concentration and the model prediction for different steady-state points (dashed lines with symbols: experimental data; solid lines: simulation).

Figure 2.2 shows the particle emissions upstream and downstream of GPF A and B with the characteristics from Table 2.2. The emissions values are normalized to the maximum upstream particle concentration (see Figure 2.3 d). GPF B has lower tailpipe emissions,

which can be mainly attributed to the smaller mean pore size. The particle size distribution upstream of the filter shows a plateau around 50 nm with steep flanks towards larger particles, similar to the measurements of Viswanathan et al. [62]. In all tests, small particles below 23 nm are reduced notably due to diffusion as dominant filtration mechanism.

The model prediction (solid lines) and the measurement data (dashed line) are in good agreement for the diffusion dominated particle sizes. The peak in downstream particles is underestimated for GPF A, but the simulation predicts the most penetrating particle size correctly in each case.

Figure 2.3 compares the corresponding filtration curves for the different working conditions. Here the model prediction and the measurements differ for large particles above 100 nm. This discrepancy can be explained in part by the low particle concentration of large particles at the inlet and the corresponding lower measurement accuracy of the particle analyzer. Figures 2.3 e,f depict the contribution of each filtration mechanism for the last operating point. Note that the mechanisms are not additive due to Equation 2.2. For both filters, small particles are almost exclusively captured via diffusion. However, its impact is deceasing with the particle size. The collection efficiency of interception is small compared to the impact of inertia under these operating conditions, because of the high space velocity (*SV*) as well as the small particle size.

As the *SV* rises, the filtration efficiency stagnates and even slightly increases. This behavior is, to the best of the authors' knowledge, not recorded for filters in the automotive context before, due to the lack of comparable measurements in the literature. The extensive GPF cleaning procedure before each steady-state measurement, as well as the usage of only the first 20 s of the measurement time, minimizes the possible influence of soot loading. During this time interval, no trend towards higher filtration efficiencies was detected. To model the stagnation and slight increase in filtration efficiency, it is necessary to enhance the particle capture to due inertial deposition. The interception is independent of the filtration velocity, since it is understood as a phenomena of the ratio of pore size to particle size. However, with increasing velocity, the inertia of the particles increases as well. Thus, particles are no longer able to follow the streamlines of the fluid and hit the porous medium.

(a) *SV*: 90 s^{-1}, T: 715 °C

(b) *SV*: 170 s^{-1}, T: 790 °C

(c) *SV*: 180 s^{-1}, T: 780 °C

(d) *SV*: 215 s^{-1}, T: 810 °C

(e) Contributions of different filtration mechanisms for GPF A at *SV*: 215 s^{-1}, T: 810 °C

(f) Contributions of different filtration mechanisms for GPF B at *SV*: 215 s^{-1}, T: 810 °C
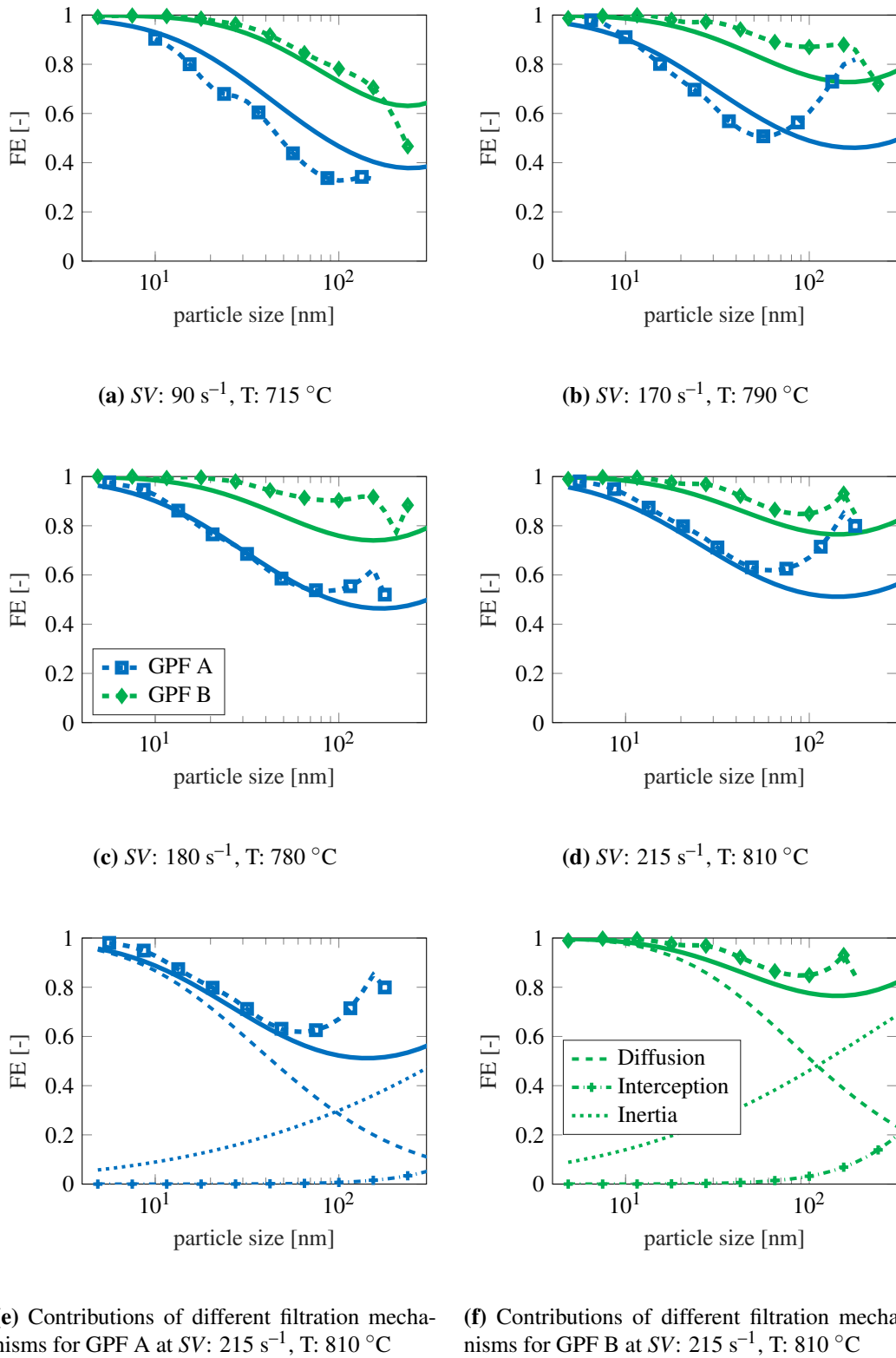
Figure 2.3: Comparison of simulated and measured filtration efficiencies for the steady-state points (dashed lines with symbols: experimental data; solid lines: simulation).

2.4.2 Driving Maneuver Simulation

Academic studies typically utilize steady-state operating points for filtration experiments [62]. However, in practice, dynamic drive cycles are an essential design criterion. Therefore, models used for system design should be able to reproduce transient scenarios. With filtration measurements, there are two main obstacles for reliable transient measurements under industrially relevant conditions. Firstly, the reproducibility of particle emissions is not as high as for gaseous emissions, since the particles are strongly affected by the experimental conditions, e.g., temperatures in the engine. Secondly, the length of the transient measurement has to be short to minimize the impact of soot deposition in the filter since this study is about fresh filtration, which is, next to the pressure drop, the key criterion for choosing a GPF [83, 90]. For these reasons, the dynamic driving maneuver in this study consists of a short acceleration with a cold engine. Since, the cold-start is responsible for most particle emissions [8, 94], this test is an important aspect for the design of the exhaust gas aftertreatment.
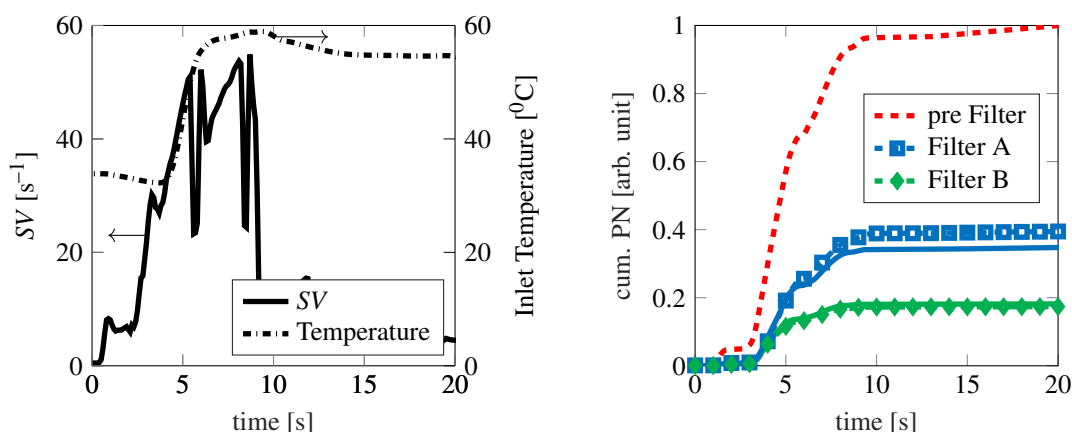
(a) Measured space velocity and temperature.

(b) Cumulative particle number normalized to the inlet's emissions: simulation versus measurement.

Figure 2.4: Dynamic filtration experiment - used profile and corresponding simulation (dashed lines with symbols: experimental data; solid lines: simulation).

The course of space velocity and temperature of this driving maneuver is shown in Figure 2.4 a. Since a recorded profile of a vehicle was used, the *SV* drops during gear shifts. Note that the temperature never exceeds the dew point in the measurements. Figure 2.4 b illustrates the cumulative particle emissions normalized to the emissions upstream of the filter. Again, the setup employs the same GPFs as for the steady-state experiments. As expected, GPF B with the smaller mean pore size yields lower emissions. Overall, the

model achieves a high prediction quality of the cumulative emissions.

(a) GPF A normalized time-integrated particle distribution

(b) GPF B normalized time-integrated particle distribution

(c) GPF A filtration efficiency

(d) GPF B filtration efficiency
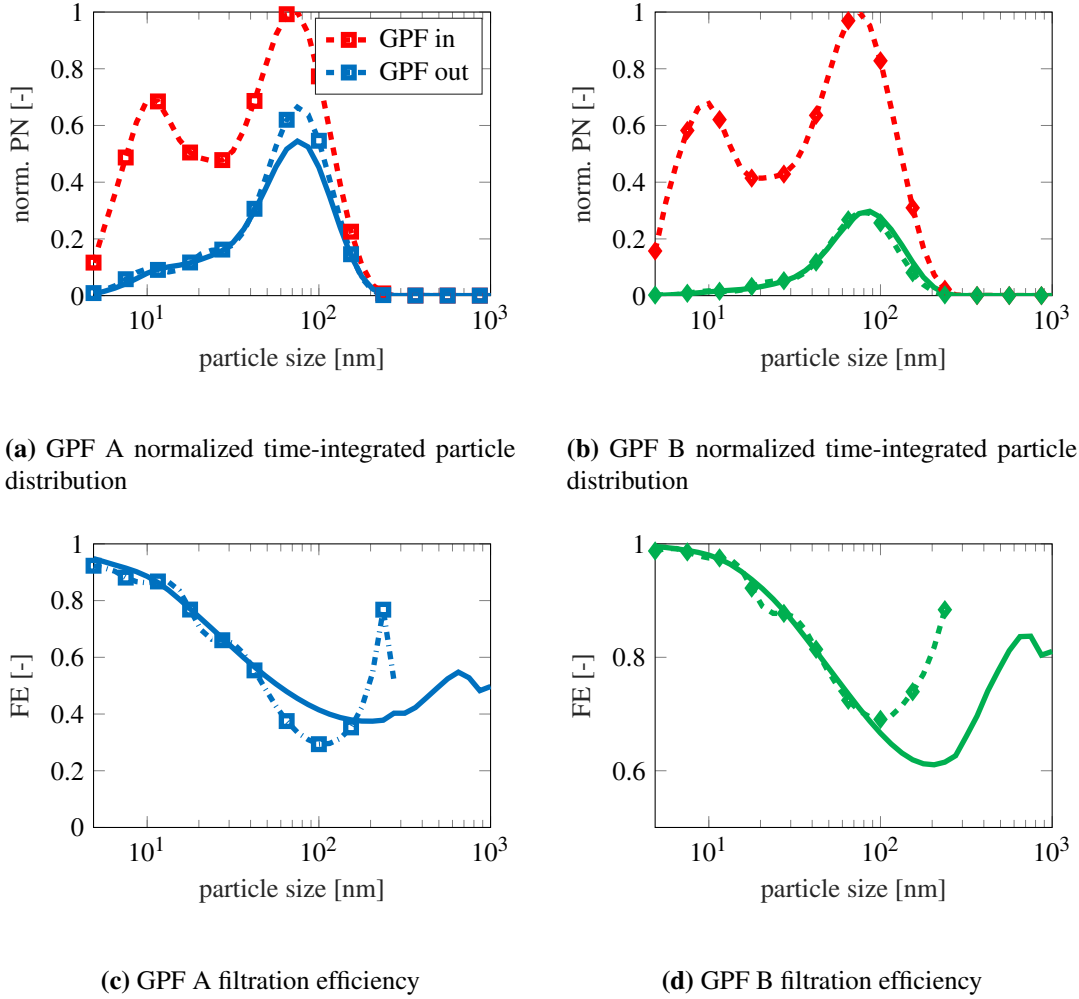
Figure 2.5: Time-integrated size-resolved particle flow normalized to the peak upstream of the GPF and resulting overall filtration efficiency: simulation vs. measurement (dashed lines with symbols: experimental data; solid lines: simulation).

In Figure 2.5, the particle size distribution of the whole driving maneuver is displayed. Hereby, the transient particle number flow of each particle size is integrated over time, according to Equation 2.19, to determine the resulting time-integrated particle size distribution of a transient measurement:

$$PN(d_p) = \int_{t=0}^{t_{end}} \frac{\dot{m}(t)}{\rho_{exh}} \cdot PNC(d_p, t) dt \quad . \tag{2.19}$$

The exhaust gas density ρ_{exh} at standard conditions for E10 fuel is used [159]. Figure 2.5 a,b shows the particle size distribution at the inlet as well as the downstream particles for GPF A and B, together with the corresponding model fit. The particle numbers are normalized to the maximum value of the measured upstream value at approximately 70 nm. When comparing the result to the steady-state measurements, a shift

towards larger particles can be seen. Again, the most penetrating particle size is around 80-100 nm. The subfigures 2.5 c,d show the corresponding filtration efficiencies. Here, the model prediction differs from the measurement for larger particles. The divergence is caused in part by the low upstream particle flow of this size and, by the corresponding lower measurement accuracy.

Due to temperatures below the dew point as well as space velocities around 50 1/s, the filtration efficiency is lower than for the steady-state measurements above. The simulation quality demonstrates that these effects are predicted accurately by the model. In summary, the shown accuracy validates the proposed correlation for the usage in system design.

2.4.3 Sensitivity on Filter Characteristics

An additional variation of the pore size and the wall thickness provides a validation of the determined inertia coefficients. For this, we have tested five adaptions of GPF B with controlled pore-size distribution employing the same procedure as before. For clarity, only the steady-state measurements at 750 °C and 90 s^{-1} are stated. The particle counter is used to validate the simulation. Thus, the analysis of the filtration efficiency consists only of particles above 23 nm.
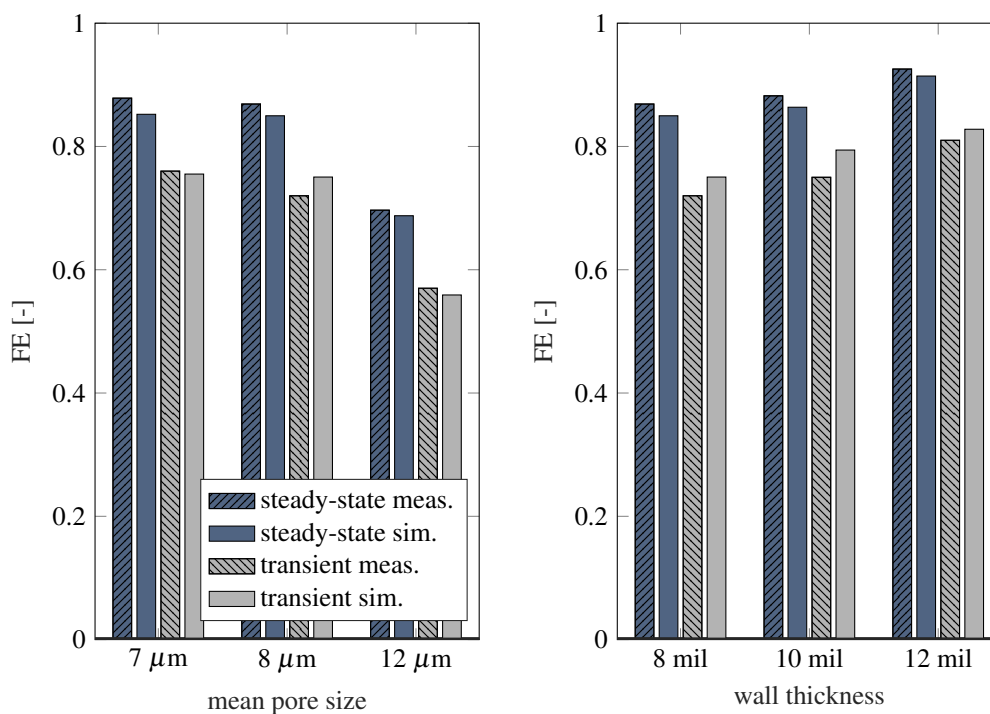
Figure 2.6: Sensitivity on mean pore size and wall thickness of the filtration model.

Figure 2.6 illustrates the measured and simulated filtration efficiencies. The variation of the mean pore size on the left side shows the expected decrease in filtration efficiency with rising pore size. The variation of the channel wall thickness from 8.5 mil to 12 mil results in higher FE as well. Nevertheless, in this case, the differences are smaller compared to the variation of the pore size. Naturally, the pressure drop that is not part of this study increases with the wall thickness as well as with smaller pore sizes.

The results of the model prediction (hatched bars) follow the trend correctly in both variations. Except for the permeability to correctly capture the wall velocity in the channel, no further adaption of parameters is necessary to simulate the filtration efficiency. Thus, the above-found coefficients for the inertial deposition are valid in a wide range of different GPF properties.

Note that the cell width is dependent on the wall thickness and the cell density. Therefore, the variation of the wall thickness at constant cell densities yields a slightly different cell width of the channels. To address this issue, a simulation of the wall thickness variation with constant cell width was conducted. This test has shown less than 1% deviation from the reference simulation.

2.4.4 Simulation Study - Sensitivity on Operation Conditions

A simulation study using GPF A and B is conducted to explain the influence of the operating parameters temperature and space velocity.

The first numerical experiment evaluates the impact of temperature at a fixed space velocity of 40 s^{-1}. A second analysis varies the space velocity at a constant temperature of 500 °C. The temperature variation in Figure 2.7 a,b shows that the temperature mainly influences the diffusion process. Especially the FE of smaller particles is increasing with higher temperature, whereas large particles above 200 nm are collected less efficiently. The latter effect of decreasing FE, which is of low practical interest, since few particles exceed the size 100 nm in gasoline exhaust gas, can be explained with the dependence of the Stokes number on the fluid density. Additionally, the most penetrating particle size is shifted towards larger particles with increasing temperature. The bottom half of Figure 2.7 depicts the influence of the space velocity. A low space velocity yields a completely diffusion-controlled filtration curve with high FE for small particles. A slight increase in the volume flow results in lower FE because of a decrease in collection efficiency due to diffusion. A further increase in space velocity reverses the trend. The FE is increasing again, because of the enhanced inertia of the particles. Especially heavy particles with large diameter are captured better with increasing volume flow.
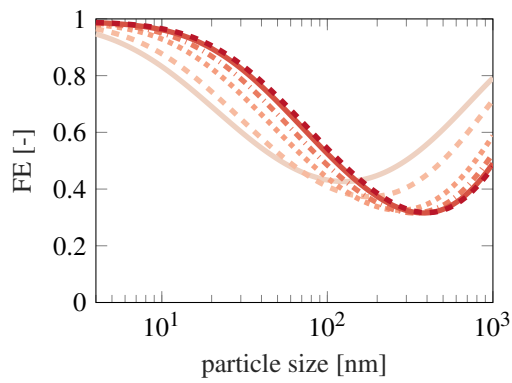
(a) GPF A (S$_V$: 40 s^{-1})
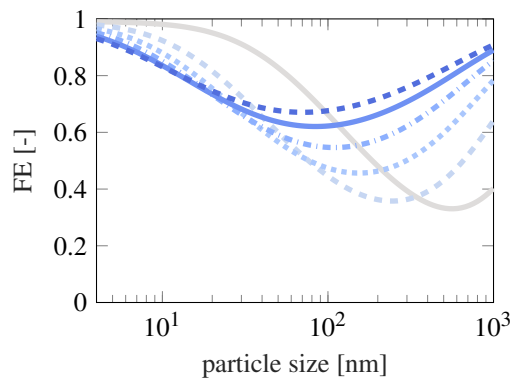
(b) GPF A (T: 500 °C)
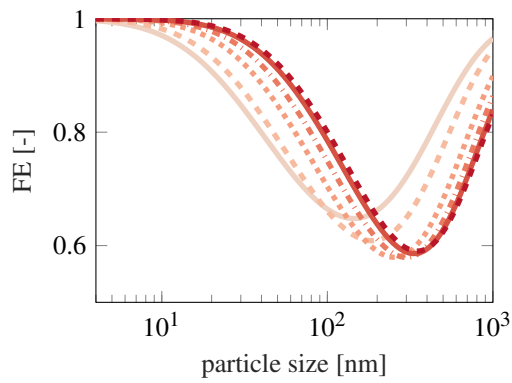
(c) GPF B (*SV*: 40 *s*$^{-1}$)
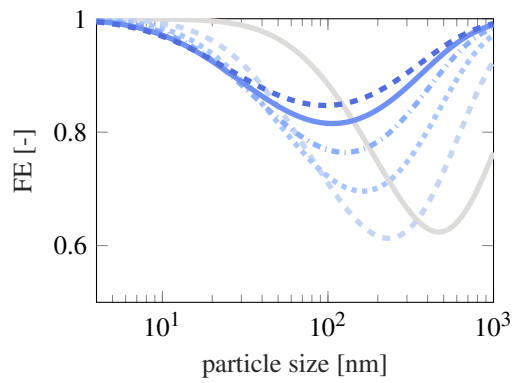
(d) GPF B (T: 500 °C)
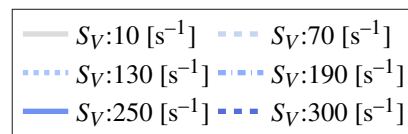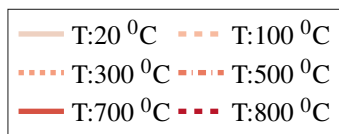
Figure 2.7: Simulation of the influence of temperature and space velocity on fresh filtration efficiency.

2.4.5 Comparison of Modeling Approaches

To further investigate the interaction of the used correlation and the space velocity, a comparison of different modeling approaches using a representative inlet particle size distribution (see Figure 2.2 c) with the characteristics of GPF B is conducted. Each case utilizes the same, here presented model framework for the channel scale simulation to avoid discrepancies due to different axial wall velocity distributions. Only the correlations for the filtration mechanisms and the usage of a pore size distribution versus one mean pore size ($d50$) are changed. If a model includes additional calibration factors, e.g. interception length scale [83] or a sticking probability [84], the parameters are set to the default value, which is normally one. For the soot penetration in the Serrano et al. [84] series, a lower bound of the effective filter wall thickness is utilized to achieve a smooth characteristic at SV approaching zero.
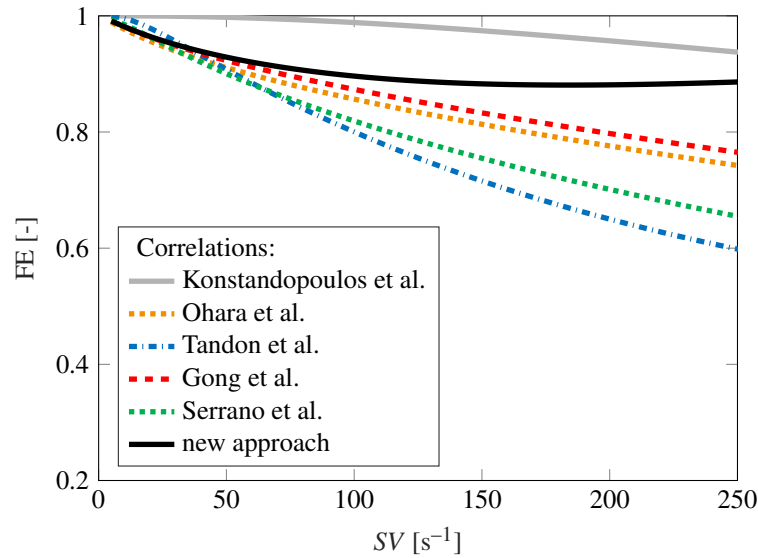
Figure 2.8: Filtration efficiency for a representative particle size distribution (taken from Figure 2.2 c) calculated with different filtration models.

Figure 2.8 shows the resulting filtration efficiency as a function of the space velocity for each model. Note that, the validated range of SV is different for the approaches (see Table 2.1) and the highest measured space velocity for the here proposed model is 210 s^{-1}. When comparing the new approach of this study with established filtration models for space velocities smaller than 50 1/s, the results for most modeling approaches - including our approach - are similar since many of these researchers utilized the same set of experiments for model validation and very similar correlations. The model prediction of Konstandopoulos et al. [78] differs from the other approaches because the authors only

considered a mean pore size instead of a pore size distribution. The flow distribution between different pore sizes drastically reduces the FE due to diffusion. Tandon et al. [119] did not correct the drag force on small particles using the *SCF* correction. Therefore, the calculated diffusivity of particles decreases considerably. Gong et al. [83] as well as Ohara et al. [116] utilize an effective Stokes number and different coefficients for the inertial deposition compared to Tandon et al. [119] and Serrano et al. [84], which leads to their slower decrease in filtration efficiency. The variable soot penetration in the approach of Serrano et al. [84] dampens the FE decrease compared with Tandon et al. [119].

The new approach follows the model of Gong et al. [83] for low space velocities. In several studies, this model was validated against experimental data in the literature [83, 85, 122]. However, when further increasing the space velocity, the model approaches differ. Only this approach yields a complete stagnation and even a slight increase again because of the proposed correlation for inertial deposition. Modelers should use this method when predicting filtration at high volume flow. To further investigate the interaction of space velocity and filtration, the particle-size resolved development of the filtration efficiency for different space velocities as well as temperatures are shown in the supporting information.

3 Applying 3D X-Ray Microscopy to Model Coated Gasoline Particulate Filters under Practical Driving Conditions

Summary of the publication:

Recent progress in 3D X-ray microscopy allows to analyze coated Gasoline Particulate Filters on a detailed pore scale level. However, derivable detailed three-dimensional models for filter simulation are not applicable under transient driving conditions of automotive aftertreatment systems due to their inherent complexity. Here, we present a novel concept to utilize highly resolved 3D X-ray microscopy scans and their quantitative analysis for a macroscopic model of coated Gasoline Particulate Filters intended to be applied in a driving cycle. A previously developed filtration model build on a 1D+1D flow model on the channel scale of a filter is utilized. Accompanying measurements conducted on a dynamic engine test bench serve as validation for pressure drop and filtration characteristics. With the determined properties from 3D X-ray microscopy, the macroscopic model successfully replicates the measurements. Regarding the filter coating, the reduced porosity and a decrease of medium sized pores relative to an uncoated substrate reduce the filtration efficiency under steady-state as well as transient conditions.
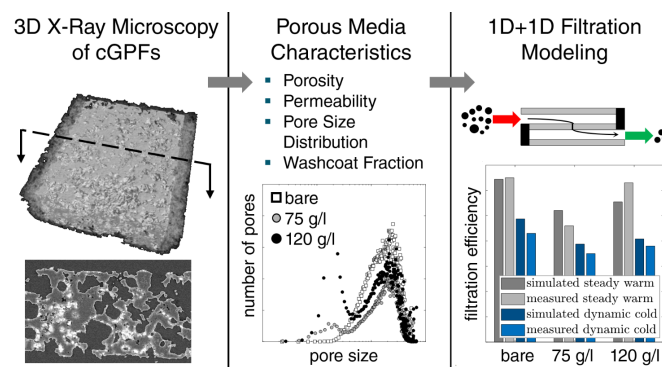
Individual Contributions of the Candidate

The contribution of the candidate to this publication included the preparation of the samples as well as the latter analysis of the filtration and 3D X-ray microscopy measurements. Astrid Velroyen conducted the 3D X-ray microscopy measurements and organized the necessary time slots and the software resources for the 3D analysis. The candidate also carried out the conception and implementation of the model as well as writing the manuscript. Jens Neumann help planning the experiments and supervised the modeling process. Prof. Olaf Hinrichsen reviewed and edited the manuscript.

3.1 Introduction

To cope with the increasingly stringent legislation regarding the particle number emissions [70], Gasoline Particulate Filters (GPF) are a relatively new technology [68, 80] applied in automotive aftertreatment systems. In addition to the filtration purpose, the GPF can be optionally coated to incorporate the function as three-way-catalyst (TWC) in order to decrease the necessary packaging volume and costs. The washcoat made of Pd/Rh with cer supported by alumina [90, 160] is usually deposited in the wall [110]. This process influences the porous media [97] and therefore strongly impacts the filtration and pressure drop behavior of the filter.

Recently, progress in X-ray tomography (XRT) allows to elucidate structures inside the porous walls of coated wall-flow filters on a pore scale. Especially, X-ray microscopy (XRM), that combines computed tomography with an optical lens system, offers high resolution of these small structures. This opens up the possibility to simulate the fluid flow, chemical reaction kinetics or even filtration behaviour by means of three-dimensional (3D) computational fluid dynamics (CFD) approaches. For flow behaviour with focus on pressure drop and permeability, XRM scans can be analyzed by 3D CFD [97, 161, 162]. Kočí et al. [110] and Greiner et al. [163] introduced such a methodology for a pore-scale simulation of flow, diffusion and reaction in a coated catalytic filter. Also with focus on catalytic reactions, Belot et al. [144] investigated the impact of the washcoat distribution by 3D CFD. Recently, Plachá et al. [87] developed a 3D CFD model for filtration to analyze its interplay with the washcoat distribution.

Despite of its ability to gain access to detailed structures on a pore scale, 3D CFD is – due to its numerical requirements – still not applicable for simulations with a broader scope, e.g. driving cycle analysis or control-oriented modeling of filter behaviour. For this purpose, Gong et al. [85] developed a workflow to incorporate the pore size distribution of low-resolved XRT scans in a previously developed macroscopic filtration model [83, 122] for uncoated GPF's. This type of filtration model usually works on channel scale and is an established approach since many years for Diesel and Gasoline particulate filters [78, 84, 116, 119, 140, 164, 165]. In a previous work of us, we extended a macroscopic filtration model to high space velocities by suggesting a new correlation for the particle collection due to inertial deposition [95].

The aim of the present study is to combine the XRM-based access to pore scales of a GPF with a macroscopic filter model. As the novel aspect here, we extend the general workflow of Gong et al. [85] for the first time to a coated GPF (cGPF). Also, the XRM technique that allows for finer resolution is utilized.

In our workflow presented below, pressure drop and filtration efficiency behavior of two differently coated filters and their corresponding bare substrate are measured on a specifically equipped dynamic engine test bench. Also, XRM scans are conducted. In the postprocessing of the scans, porosity, pore size distribution and permeability are derived by volumetric analysis as well as via a subsequent 3D CFD simulations. Finally, the determined characteristics of the porous media are applied in our previously published macroscopic 1D+1D filtration model [95].

3.2 Materials and Methods

For the validation of the different experimental and numerical methods applied in this work, three research cGPFs samples are tested: two differently coated filters and the corresponding bare substrate. The nominal cell density of the cordierite substrate is 300 cpsi and its wall thickness is 8 mil (0.2 mm) nominal. All samples have the same diameter of 132 mm and a length of 120 mm. The two coatings differ in the amount of washcoat applied. The first cGPF, denoted as C1 in the following, is coated with 75 g/l. For the second one, 120 g/l are applied and the notation C2 is used.

3.2.1 3D X-Ray Microscopy Tomographic Imaging

In a defined preparation procedure, every filter is divided up axially through the centerline to extract two filter halves with original length. From the axial middle of the filters, 3×4 mm sized samples are then manually extracted using a scalpel. Hereby, attention was paid to avoid damaging the vulnerable channel structure of the sample.

The XRM scans were conducted on a Zeiss Xradia 620 Versa at 60 kV source voltage and 20x optical magnification. During the scanning, the sample rotated stepwise. In every position, a transmission image with an exposure of 20 s was captured which

leads to a total scan time of 25 h per sample. Due to the high optical magnification, a resolution of $0.3\,\mu$m/voxel is obtained. The resulting scans contained approximately $1500{\times}700{\times}1800$ voxels.

In a postprocessing of the scans, it is necessary to determine the interface between solid and void as well as to distinguish the washcoat from the cordierite. Within the VGSTU-DIO MAX software [166], a specified surface determination workflow was developed to obtain a realistic representation of the solid-to-void surface. It includes several steps of the OpeningClosing function to remove false particles or voids and to finally obtain a realistic representation of the surfaces. Note that the washcoat of sample C1 and C2 has a significantly higher density than the cordierite substrate opening the option to distinguish them by the radiodensity value. Thus, it was possible to segment washcoat and cordierite by their grey values into distinct volume portions for further analysis.

Next, the characteristics of the porous media are determined. For the porosity of the samples, a workflow utilizing a defect ROI is applied [166]. The maximum sphere inscription method (see e.g. [167]) is used for the pore size distribution. The permeability of the samples is determined by 3D CFD simulations of the discretized sample volumes directly in the Transport Phenomena Simulation Module of the VGSTUDIO MAX software [166]. A Lattice Boltzmann method (LBM) is utilized based on the assumptions of a steady-state, incompressible and low-Reynolds number creeping flow. Boundary conditions in flow direction are specified as planes with constant pressure adjacent to the inlet/outlet channel surface, whereas all in-wall boundaries are defined by a no-slip condition.

3.2.2 Pressure Drop and Filtration Measurements

For the validation of pressure drop and filtration efficiency, measurements are conducted on a dynamic engine test bench equipped with a direct injection spark ignition gasoline research engine. Its main technologies are exhaust gas turbocharging, a fully variable valvetrain, and gasoline direct injection with homogeneous operation. The engine is fueled with standard gasoline (ROZ95 E10). Figure 3.1 shows a schematic of the measurement setup. The GPF placement, approximately 2 m downstream of the close-coupled catalyst, aims to resemble an underfloor position with a defined, idealized inflow to minimize effects of flow maldistribution across the filter's front face. The pressure is measured directly before and after the filter to avoid any influence of the cones. The setup and the engine are identical with the procedure described in reference [95]. The preparation

55

procedure for the XRM described above has been carried out after completion of the measurements in order to visually analyze the identical filter samples measured before. Particles are measured with two particle counters (Horiba MEXA 2100 SPCS) [158], placed downstream and upstream of the GPF with switches of these sampling location after a number of repetitions. The filtration efficiency is always calculated with data of one particle counter. Thus, slight differences between the measurement devices have no impact on the filtration efficiency value. The analyzer has a built-in cyclone. Therefore, only particles above 23 nm are measured. In order to avoid condensation of hydrocarbons the sampling lines between the analyzers and the exhaust gas system are heated.
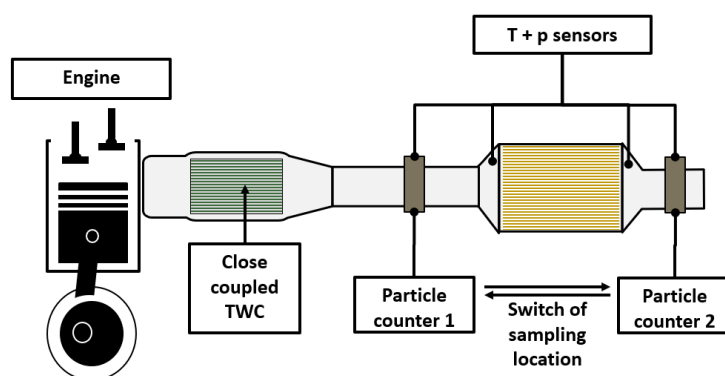
Figure 3.1: Measurement setup for the determination of pressure drop and filtration performance.

Steady-state experiments are carried out for the analysis of the pressure drop and filtration efficiency. Here, the engine runs at operating temperature of the corresponding load and speed settings. 11 defined operation points are measured, ranging up to an exhaust mass flow of about 500 kg/h and a pre-filter temperature of ca. 820 °C. Additionally, a second set of measurements is performed to validate the transient filtration performance. It consists of a highly dynamic cold-started sequence of a driving cycle with a duration of 150 s. Before each measurement point and driving sequence, respectively, an in-situ regeneration procedure, using a lean operation of the combustion engine as well as several fuel cuts, guarantees a soot-free filter. A preconditioning process achieves stable cold starting conditions before each driving sequence. This process cools the engine and its periphery down until a standardized set of temperatures (engine oil and coolant temperature, the temperature at the filter's inlet) is reached. All measurements are repeated sufficiently for each sampling location to achieve a saturated statistics of all measured quantities. The interested reader is referred to our previous study [95] for more measurement details including time traces of the transient driving cycle. Since the installed particle counter cannot determine the particle size distribution, we apply a previously measured engine out particle size distribution [95]. The measurement procedure as well as the engine are identical to the earlier study. The particle size was determined with DMS500 particle

counter. Again, the vacuumed sampling pipes were heated in order to avoid condensation. Figure 3.2 shows the normalized GPF in particle size distribution for the steady-state operating points and the mass flow average particle size distribution (in black) for the transient cycle. The characteristics are normalized to their individual maximal value, respectively.
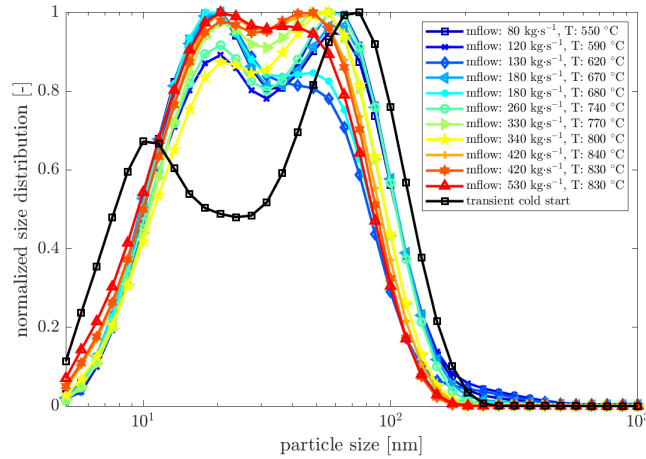
Figure 3.2: A priori determined particle size distributions. The size distribution of the transient cycle (in black) is averaged via the mass flow. All characteristics are normalized to their peak value.

3.2.3 Modeling Approach

The macroscopic filtration model [95] described below in Section Filtration Modeling is used based on the determined characteristics of the porous filter media from XRM. It is based on a flow model of the cGPF, explained first in Section Flow Model. Further details can be found in Ref. [95, 168].

3.2.3.1 Flow Model

Following a 1D+1D approach [133, 169, 170], a channel pair and the porous filter wall are discretized in axial and through-wall direction. All quantities, e.g. the through-wall velocity and the homogeneous wall temperature, are calculated on this grid. In the following equations, the index j is 1 for the inlet channel and 2 for the outlet channel.

Equation (3.1) couples the channel velocity v_j with the wall velocity $v_{w,j}$ via the continuity equation:

$$D_j^2 \frac{\partial \rho_j v_j}{\partial z} = (-1)^j \cdot 4 D_j \cdot \rho_j \cdot v_{w,j} \tag{3.1}$$

Assuming no radial deviation of the pressure in the channel, the 1D-pressure profile p is determined by:

$$\frac{\partial p_j}{\partial z} = -\beta_j (Re_w) \cdot \frac{\partial (\rho_j \cdot v_j^2)}{\partial z} - 2 \cdot \frac{\mu_j}{D_j^2} \cdot C_{f,j} (Re_w) \cdot v_j \tag{3.2}$$

Hereby, the momentum flux factor β_j and friction coefficient $C_f(Re_w)$ are applied to better match the characteristic flow in the channels of wall-flow filters. The values are interpolated using the tables provided by Bissett et al. [153] with an upper bound of three for the wall Reynolds number Re_w as recommended in the literature [153, 171]. The channels are coupled via Darcy's law (3.3).

$$p_1 - p_2 = \mu \cdot \frac{v_w}{k_w} \cdot t_w \tag{3.3}$$

Here, k_w describes the homogeneous wall permeability. To incorporate the additional pressure loss due expansion and contraction at the filter's inlet and outlet, Equation (3.4) is applied with the resistance coefficient ζ_j set to 1.25 [162]:

$$\Delta p_j = \frac{\zeta_j}{2 \rho_j} \cdot (\frac{\dot{m}}{D_j^2})^2 \tag{3.4}$$

3.2.3.2 Filtration model

Our macroscopic filtration model [95], which is based on the flow model, applies the established concept of a unit collector [140]. Hereby, the porous media of a wall-flow filter is described as a packed bed of spheres with the same hydrodynamic diameter as the pore network of the filter. This assumption allows predicting the collection efficiency η_{total} of particles on a single sphere (unit collector) with the diameter d_c, that is then integrated across the filter wall. Equation 3.5 expresses the resulting filtration efficiency due to the contribution of each unit collector in a filter wall with the thickness t_w and the porosity ε as:

$$FE = 1 - exp(-\frac{3(1-\varepsilon)}{2\varepsilon} \frac{\eta_{total} \cdot t_w}{d_c}) \quad . \tag{3.5}$$

Three main mechanisms contribute to the collection efficiency: Brownian diffusion η_D, direct interception η_R and inertial deposition η_I [80, 83, 84]. Other possible mechanisms are considered negligible. With the assumption that all mechanism are independent of each other, the resulting collection efficiency is expressed as:

$$\eta_{total} = 1 - (1 - \eta_D) \cdot (1 - \eta_R) \cdot (1 - \eta_I) \quad . \tag{3.6}$$

Brownian diffusion

We utilize the correlations of Lee and Gieseke [82], who analytically solved the convection and diffusion of particles in a flowfield described by Kuwabara's solution for a packed bed of spheres [111]. Equation 3.7 expresses the the collection efficiency due to diffusion as:

$$\eta_D = 2 \left(\frac{3\pi}{4} \right)^{\frac{2}{3}} \left(\frac{\varepsilon}{K(\varepsilon)} \right)^{\frac{1}{3}} \cdot Pe^{-\frac{2}{3}} \tag{3.7}$$

with the Peclet number *Pe* defined as:

$$Pe = \frac{U_i \cdot d_c}{D_D} \quad . \tag{3.8}$$

Here, U_i represents the interstitial velocity, d_c is the respective unit collector size and D_D the particle diffusion coefficient. $K(\varepsilon)$ is Kuwabara's hydrodynamic factor [111], that is given by Equation 3.9.

$$K(\varepsilon) = 1 - \frac{9}{5}(1 - \varepsilon)^{\frac{1}{3}} + (1 - \varepsilon) - \frac{1}{5}(1 - \varepsilon)^2 \tag{3.9}$$

Direct interception

If the fluid transports a particle within the radius of the unit collector's surface, the particle sticks on the unit collector and is intercepted. For this mechanism, the established correlation of Lee and Gieseke [82] is applied

$$\eta_R = \frac{3(1 - \varepsilon)}{2K(\varepsilon)} \cdot \frac{N_R^2}{(1 + N_R)^2} \tag{3.10}$$

with the interception parameter N_R defined as the ratio between particle and unit collector size:

$$N_R = \frac{d_p}{d_{c,i}} \quad . \tag{3.11}$$

Inertial deposition

The inertia mechanism of particulate capture describes the inability of particles to follow streamlines of the gas due to their own inertia. For the modeling, the Stokes number *Stk* is applied. This number describes the ratio between the particle stopping time and its residence time [149]. Hereby, the Stokes-Cunningham factor (*SCF*) corrects the drag force of small particles:

$$Stk = \frac{1}{9} SCF \frac{\rho_{soot,eff} \cdot U_i \cdot d_p^2}{\mu \cdot d_c} \quad . \tag{3.12}$$

Hereby, the effective density of the soot particles $\rho_{soot,eff}$ is assumed constant at $800\,\mathrm{kg/m^3}$ [113].

Similarly to the work of D'Ottavio and Goren [151], we are using Kuwabara's hydrodynamic factor $K(\varepsilon)$, since this flow field calculation is employed by all other collection efficiency correlations as well. This assumption leads to the following definition of the effective Stokes number Stk_{eff}:

$$Stk_{eff} = Stk \cdot (1 + \frac{Re}{K(\varepsilon)}) \quad . \tag{3.13}$$

Following the same form as in Ref. [81, 149, 151], the resulting correlation for the collection efficiency due to inertia η_I is defined in Equation 2.10 with experimentally determined coefficients [95]

$$\eta_I = \frac{Stk_{eff}^{0.7817}}{(2.4363 + Stk_{eff})^{0.7817}} \quad . \tag{3.14}$$

Pore size distribution

The pore size distribution acquired from XRM analysis is integrated into the macroscopic filter model by transforming it into a discrete probability density function (*pdf*) similar to Gong and Rutland [83] with the main difference that we do not apply a log-normal fit [164]. Afterwards, by applying Equation 3.15, the *pdf* of the corresponding unit collectors is determined:

$$pdf_{d_c} = \frac{2\varepsilon}{3 \cdot (1-\varepsilon)} \cdot pdf_{d_{pore}} \quad . \tag{3.15}$$

The collection efficiency is first calculated for each unit collector size and then combined using a relative area approach

$$\eta_{total}(d_p) = \frac{\int \eta_{total}(d_c, d_p) \cdot d_c^2 \cdot pdf_{d_c} \quad d(d_c)}{l_{d_c}^2}$$ (3.16)

with l_{d_c} as the root of the mean area:

$$l_{d_c} = (\int pdf_{d_c} \cdot d_c^2 \, d(d_c))^{\frac{1}{2}} \quad .$$ (3.17)

3.3 Results and Discussion

3.3.1 3D X-Ray Microscopy Results

Figure 3.3 shows sectional views of the filter wall of the three samples taken from XRM scans. In the lower row, a finer scan of the middle of the horizontal wall between two neighboring crossings of vertical and horizontal walls is depicted. A representative part, the so called region of interest (ROI) is used for later analysis. Additionally, corresponding coarser scans located at crossings are depicted in the upper row of Figure 3.3. The two different solid materials cordierite and washcoat and the void can be clearly distinguished between white (washcoat), gray (cordierite) and black (void). A highly porous structure of the cordierite substrate wall becomes visible with a collection of different pore sizes, ranging from small pores up to some – in relation to the wall thickness – very large pores.
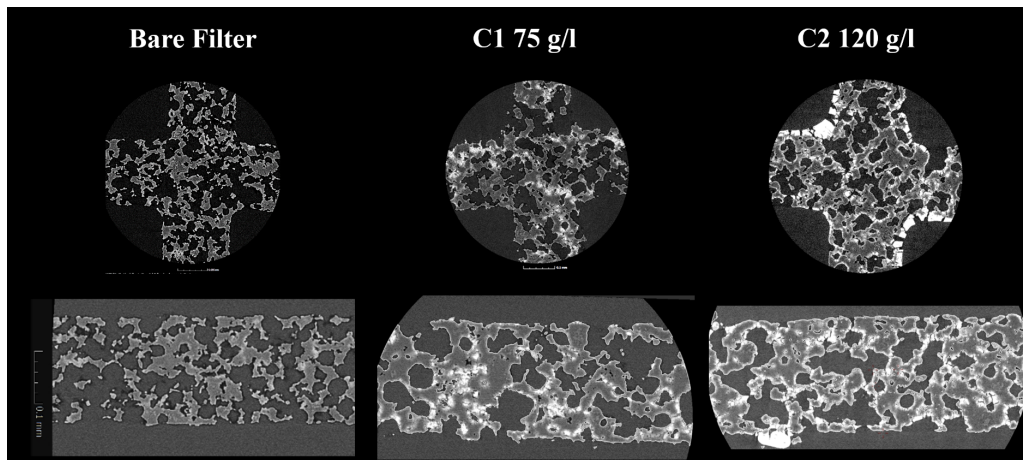
Figure 3.3: 3D X-ray microscopy scans.

The washcoat for the samples C1 and C2 is distributed quite heterogeneously. Whereas small pores are often completely filled with coating material, larger pores are covered by washcoat only at its margins. All scans of C1 and C2 show that the washcoat is located in-wall independently of the washcoat amount. However, for C2 with 120 g/l washcoat amount, it becomes visible from the view of the crossing ROI that there is a thin layer of washcoat deposited on the wall in addition to the in-wall coating. This on-wall layer is discontinued by cracks which likely stem from a thermal impact [110]. Note that no such layer can be detected in the mid-wall ROI (Figure 3.3, lower row, right), with one local exception of a single visible spot with high washcoat concentration at the lower wall. Therefore, similar to classical on-wall coating the excess washcoat of in-wall coated filters concentrates on the corner of the channels. Since there is only negligible through-wall flow at the corner as the symmetric pressure gradients of four channels cancel each other at the crossing point, the on-wall layer at this location is not considered in the model. A possible impact on the friction losses in the channel is assumed to be minor because the layer only slightly changes the square geometry.
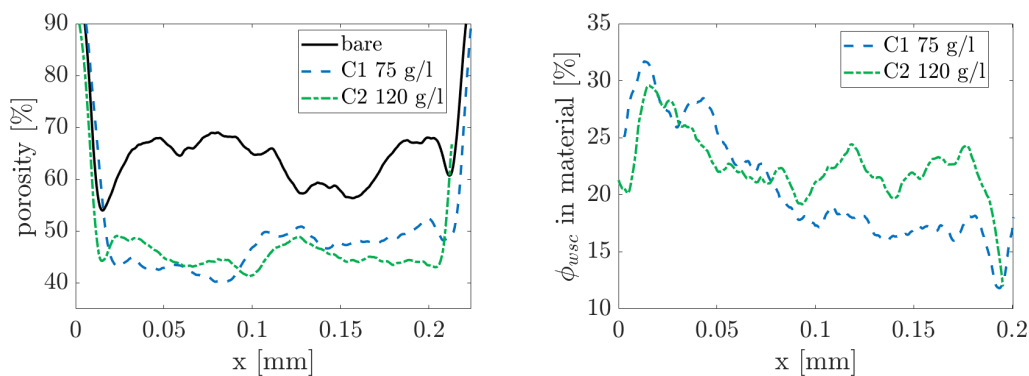
(a) Porosity along the x-direction.

(b) Volumetric washcoat fraction along the x-direction.

Figure 3.4: Porosity and volume fraction of washcoat along the through-wall direction.

An analysis of the porosity distribution in through-wall direction is shown in Figure 3.4a. In order to collect these characteristics, the ROI is divided into layers with a thickness of two voxels. For every layer, the porosity is determined, resulting in a continuous characteristic along the through-wall direction. At the boundaries to the channel, no uncoated or coated solid material exists and obviously the porosity of all samples degrades to 100%. To further focus on washcoat distribution, corresponding characteristics of the volumetric ratio of washcoat related to the overall solid volume are depicted in Figure 3.4b for the two cGPF samples.

In the accompanying Table 3.1, the corresponding porosities are listed as scalar values, which are derived from a third averaging along the through-wall direction. The XRM technique allows a detailed analysis of the characteristics of a coated filter. Without this analysis, no simulation of the filtration efficiency would be possible as the porosity and pore size distribution of cGPFs are necessary.

Table 3.1: Porous media properties determined by XRM.

		Bare Filter	C1 75 g/l	C2 120 g/l
porosity [%]		63.2	46.4	45.0
D50 [μm]		22.3	23.2	20.9
permeability by measurement fit [μm^2]		2.2608	0.85941	0.8466
permeability by LBM simulation [μm^2]		4.05	1.21	0.39
	Bare	2.26	1.03	0.859
permeability by Kuwabara's law [μm^2]	C1	1.89	0.859	0.717
	C2	2.23	1.01	0.847

By closing the volume balance of the washcoat, cordierite and void fractions and comparing the results with the bare filter, the accuracy of the segmentation is evaluated. Around 5% of solid material is wrongly recognized as cordierite instead of washcoat. Considering possible deviations of the bare substrate's porosity and the small scales, the deviation is low.

For the bare filter, the local porosity fluctuates around its averaged value of 63% with a deviation amplitude of around 5%. However, no clear trend of increasing or decreasing porosity is detectable. The porosity of the samples C1 and C2 is significantly decreased relative to the bare substrate, i.e. the additions of washcoat reduced the porosity by up to 18%. The analysis of the washcoat fraction inside the solid material volume from Figure 3.4b reveals that the washcoat is distributed slightly non-homogeneous, especially for C1. The trend from higher fractions at lower y-positions to lower fractions at the other channel side is visible for both C1 and C2, however, with a lower gradient for C2.

The pore size distributions for the three samples are determined by the maximum sphere inscription (MSI) method [167]. Václavík et al. compared this method with the classical mercury porosimetry concluding that the pore size distribution determined by MSI could be closer to reality than the classical mercury intrusion value. Exemplary, Figure 3.5a depicts the results of the analysis of the pore size with the gathered sizes distributed across

a cross-section of the ROI. As shown in Figure 3.5b, the resulting volume-averaged distributions reveal a common maximum frequency of occurrence at approximately $20\,\mu$m. The exact values of the corresponding mean pore size D50 vary between 21 and $23\,\mu$m as listed in Table 3.1. The number of pores per unit volume at this $20\,\mu$m peak – and particularly in the size range between 4 and $20\,\mu$m – is lower for the coated filters C1/C2 than for the bare substrate.
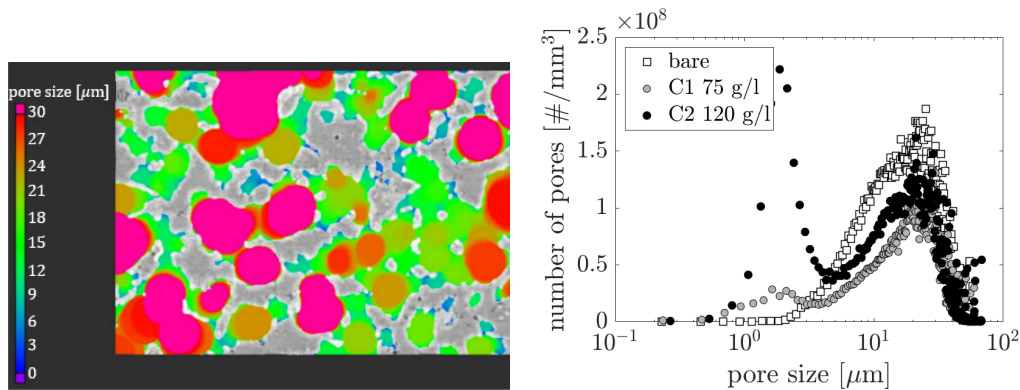
(a) Determination of the pore size via maximum sphere inscription method.

(b) Resulting pore size distribution for the three tested filters.

Figure 3.5: Pore size distribution of the three filters determined via maximum sphere intrusion method.

For the cGPF's C1 and C2, a second statistical frequent pore size of $2\,\mu$m is evident from Figure 3.5b. This can be interpreted as a high number of small pores and cracks which are located inside the washcoat, as the bare substrate apparently reveals no such peak of occurrence. Nevertheless, we assume that this $2\,\mu$m peak is of minor importance for pressure drop and filtration behaviour, as those pores cover only a small cumulative volume relative to the substrate-originated pores with a one order of magnitude larger size. Also, the porosity/inclusion analysis [166] yielded a lot of enclosed cavities at this pore size.

Summarizing, the material additions of washcoat for the cGPF's reduce the porosity by up to 18% but as can be seen in Figure 3.5b, the number of large pores is almost constant. Hence, mostly pores between 4 and $20\,\mu$m are filled during the coating process. Additionally, the washcoat itself contains very small pores.

3.3.2 Permeability and Pressure Drop
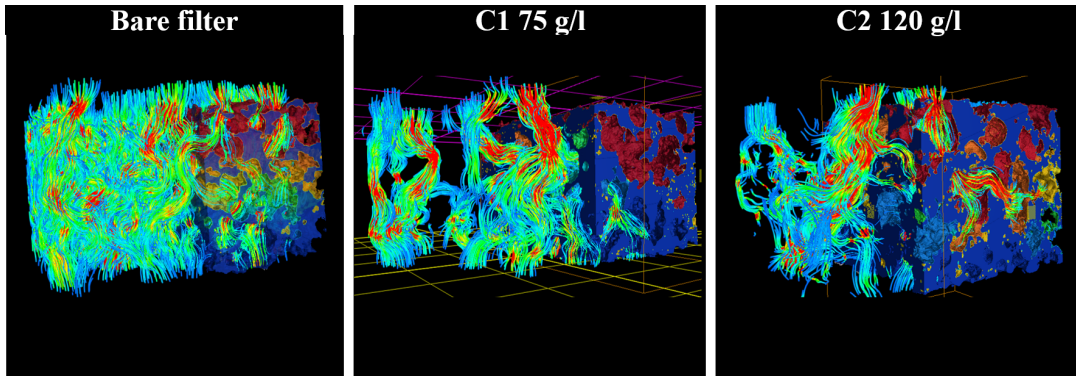
Figure 3.6: Comparison of streamlines derived from Lattice-Boltzmann simulation.

The flow behavior for the different samples is analyzed by LBM simulation which in turn is used to determine the permeability. A comparison of streamlines is provided in Figure 3.6. The streamlines are colored with the local velocity magnitude (plotted in the same color/magnitude range). Obviously, the flow is more evenly distributed for the bare filter than for the coated ones C1/C2 where locally concentrated streams with high peak velocities occur. This behaviour can be attributed to the reduced overall porosity in conjunction with lack of small and medium sized pores between 4 and 20 μm. Table 3.1 lists the derived permeabilities from LBM simulation. Consistent with the visual impression of the streamlines, the permeability of the bare filter is clearly higher than for the coated ones. Also, the permeability derived from LBM simulation for C2 is apparently lower than for C1, which, in contrast, is not explicitly observable from the streamline representations.

A comparison of the measured and the simulated pressure drop behaviour demonstrated in Figure 3.7 gives further insights into the permeability of the three sample filters. Since the temperature is increasing with the massflow the slope of the pressure drop is steeper than a comparable measurement at constant temperature due to the different densities. Figure 3.7 also includes a breakdown of the pressure drop contributions of every operating point. Here, *contr.exp* are the pressure losses due to the contraction into the channel and the expansion at the outlet. As can be seen, the losses due to the friction on the wall is the highest contributor even for the coated filters. As the flow through the porous walls only contributes moderately to the total pressure drop, the permeability will have a wide confidence interval.

The measured pressure drops plotted for different massflows reveal a lower pressure drop for the bare filter than for C1 and C2, whereas the pressure drop for C1 and C2 is
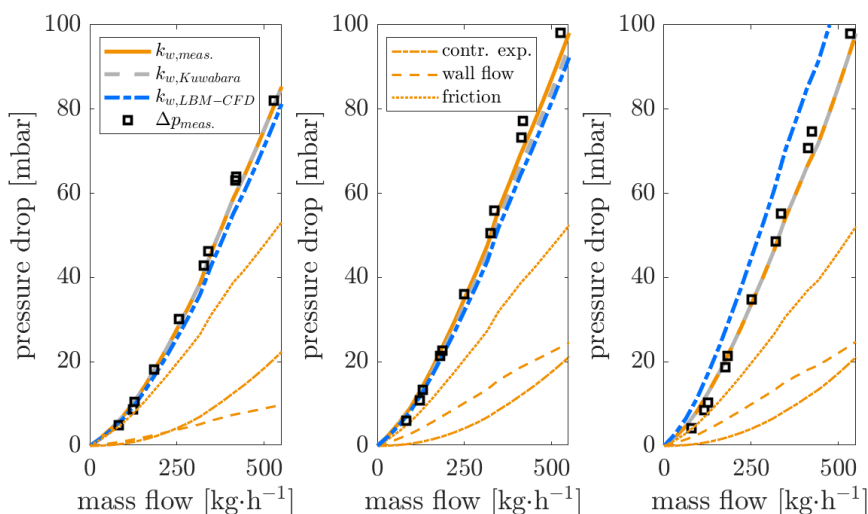
Figure 3.7: Measured and simulated pressure drop of the three tested filters (left: bare; mid: C1; right: C2). The simulation is conducted with different permeabilities. Additionally, the figure shows the different pressure drop contributions for the simulation with fitted permeability.

apparently at the same level. A possible explanation for this behavior is the very similar porosity. A major part of filter C2's additional washcoat is not in the wall but on-wall in the corner. The fitted permeabilities of the Darcy' law simulation in combination with the expansion/contraction effects (see Equations (3.3) and (3.4)) fit the measured characteristics: C1 and C2 with a similar permeability of about $0.85\,\mu\mathrm{m}^2$, which is lower than for bare filter at $2.3\,\mu\mathrm{m}^2$. As can be seen, the permeabilities from LBM simulation are not in full concordance with ones from the measurement fit. Possible reasons for this mismatch can be local effects from the selected sample location (axial middle at centerline position), e.g. a different washcoat distribution in the outer filter zones. Also, effects like the observed local on-wall layer of C2 can lead to differences. Eventually, the fact that even for the bare filter, the LBM-based permeability does not match the measurement fit, might be a hint that already the filter substrate could have a slight axial or radial anisotropy.

With the aim to predict the permeability with known macroscopic characteristics and a reference filter, the results of an additional study are also listed in Table 3.1. By applying Kuwabara's law (Equation (3.9)), the permeability for a filter is calculated relatively to its counterpart from a selected base filter.

$$k_w = k_w^{\mathrm{base}} \cdot \frac{K(\varepsilon)}{K(\varepsilon^{\mathrm{base}})} \qquad . \tag{3.18}$$

Thus, the porosities derived by XRM analysis are applied in Equation (3.18) with every filter set alternating as the base filter. This leads to the three by three matrix shown at the bottom of Table 3.1. Applying the bare filter as base filter leads to a high deviation in the empirical prediction of the permeability of filter C1 and C2. Due to its high permeability, the wall flow is not the dominant contributor to the pressure drop for the bare substrate. In consequence, the permeability, calibrated with the measurement data, is not as accurate as for the coated filter [162]. However, if one of the coated filters is applied as a base filter, the empirical correlation matches the measurement results well and also the bare filter's permeability is estimated reasonably well. For completeness, the corresponding pressure drops based on the Kuwabara-based permeabilities with filter C1 as reference filter are also plotted in Figure 3.7 demonstrating a high degree of agreement to the measured raw data.

It is worth mentioning here that even though the detailed anaysis of permeabilies from XRM is not directly connected to the general focus of this study on filtration, there is an important interplay between permeability and filtration on the modeling level. Both the permeability itself and the resulting wall-flow characteristics in axial direction of the modeled channel pair play a crucial role in all of the submodels of the macroscopic filtration model [95].

3.3.3 Filtration
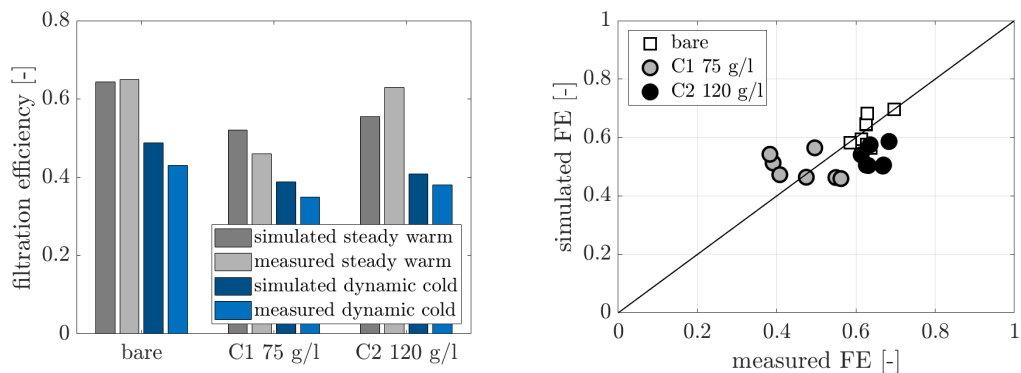
(a) Measured and simulated filtration efficiencies with the steady-state results as average value of eleven operating points.

(b) Parity plot of the statistical significant steady-state operating points.

Figure 3.8: Simulated and measurement filtration efficiency for steady-state operating points and a transient cold start acceleration.

Having gathered the porosity, pore size distribution and permeability of the three different filters from the XRM scans and the above described analyses, we are able to incorporate these data into our macroscopic 1D+1D filtration model [95]. The porous media characteristics is necessary to model the filtration and the XRM scans allowing us to examine an industrial state-of-the-art cGPF after coating. The operating conditions and the applied particle size distribution for the inlet feed are listed in Figure 3.2. The results are summarized in Figure 3.8. Hereby, the steady-state values in Figure 3.8a are averaged filtration efficiencies of the statistically significant operating points and the corresponding simualation. The first operating point and the last two operating points are neglected in Figure 3.8. The former is omitted due to the low absolute value of the tailpipe particle counter signal. The latter is neglected due to possible soot influence at high mass flows. The filtration efficiency of the transient cycle is the integral value [95]. Generally, the filtration efficiency of the cold-started transient driving cycle is markedly lower than at steady-state operation which can be explained mainly by the shift in the particle size distribution towards large particles during the cold start. For both steady-state and transient operation, the bare filter has the highest filtration efficiency (FE). With increasing washcoat amount, the cGPF C2 has a slightly higher FE than C1, without reaching the level of the bare substrate. These general trends from the measured data are well reproduced by the macroscopic simulation model. An accuracy of about 5% FE is achieved which is similar to the level documented in reference [95] for uncoated GPF's when substrate properties are varied. Still, the deviation in the prediction for coated filters is higher than for the bare substrate which could be due to anisotropies of the washcoat distribution. The successful application also demonstrates the robustness of the macroscopic 1D+1D model as the filters are quite different between the present study (D50 about $20\,\mu$m) and our previous work (D50 in the range of 7 to $12\,\mu$m) [95].

In Figure 3.9, the resulting FE curve of the macroscopic simulation model is the depicted as a function over the size of the integral oncoming soot particles for transient cycle. The low efficient filtration at a particle size of about $200\,$nm is a characteristic common feature for all three samples. Typical particles from gasoline direct injection engines have sizes up to about this value. The dominating filtration mechanism in the range below $200\,$nm is filtration via Brownian diffusion [82]. Here, C1 and C2 have apparently a lower FE than the bare substrate (Figure 3.9). The reason lies in the lower porosity as well as in the lower amount of pores with small and medium size (4 to $20\,\mu$m). Both factors lead to a reduced FE due to diffusion as can be seen in the bottom part of Figure 3.9.

It is safe to point out that due to the high computational requirements of a 3D filtration model taken from Liu et al. [102] as an example, it would not be feasible to simulate
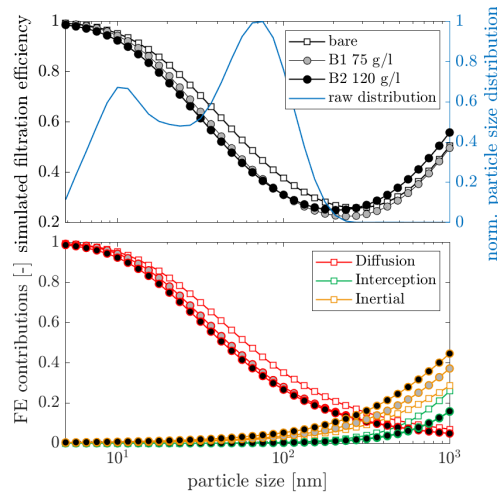
Figure 3.9: Particle size resolved filtration efficiency during the cold start with a breakdown of the contribution of each filtration mechanism.

a driving cycle like the one presented here using such a model. Hence, our approach of combining detailed XRM analysis combined with macroscopic modeling opens up a niche for application-oriented filter engineering.

To summarize, for the design of exhaust gas aftertreatment systems, it is crucial to have accurate models of particulate filters that can also predict the performance under realistic driving conditions. On the other hand, to simulate the filtration efficiency of cGPF's, an understanding of the substrate's microstructure after the coating process is necessary. 3D X-ray microscopy (XRM) is used here.

XRM scans of different cGPF's are analyzed with respect to porosity, pore size distribution and permeability characteristics. Also, local features are visualized to obtain possible limitations of the macroscopic modeling approach. Applying the determined microscopic properties in our 1D+1D filtration model [95], we can successfully replicate the filtration behavior of the filter on the engine test bench. The lower porosity of the cGPF and the decrease of medium sized pores reduce the filtration efficiency under steady-state as well as transient high-load cold start conditions. Generally, combining XRM with a macroscopic modeling approach for cGPF's is found a suitable approach for exhaust aftertreatment design.

4 Modeling the Catalytic Performance of cGPFs

Summary of the publication:

Coated gasoline particulate filters (cGPF) can reduce gaseous as well as particulate emissions with the same device. However, their more complex design compared to conventional open monoliths requires accurate models in the development phase. We therefore present a new global kinetic model for cGPFs considering standard three-way-catalyst (TWC) reactions and extend it with the impact of lean-rich cycling, referred to as dithering. Submodels are introduced for the oxygen storage and for the extent of oxidation of the active centers. Thereby, the model captures the enhanced conversion of the catalyst under various dithering as well as steady-state conditions. Several steady-state and transient experiments were conducted on a specially equipped dynamic engine test bench in order to calibrate the approach. The proposed model accurately predicts the tailpipe emissions released in a WLTP driving cycle that is not part of the original calibration data.
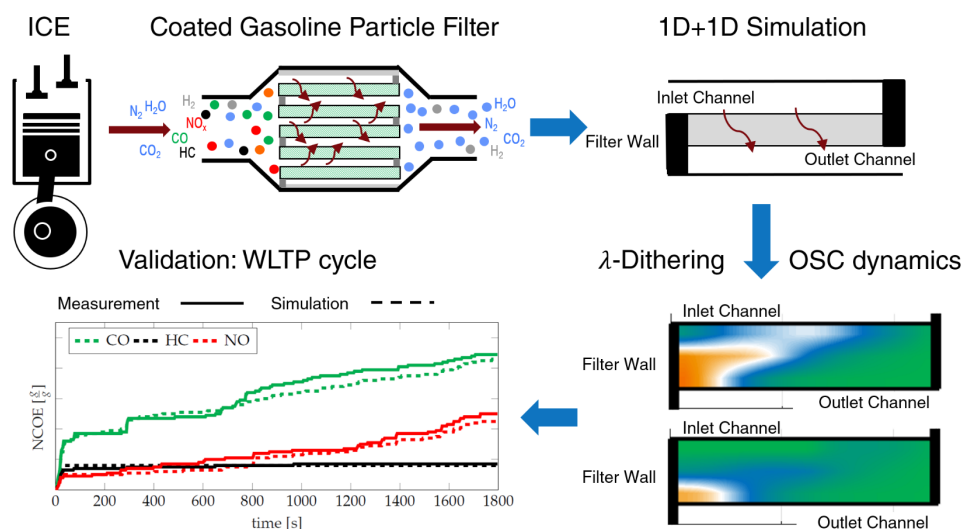
Individual Contributions of the Candidate

One of the contributions of the candidate to this publication was the analysis catalytic measurements, which served to investigate and conceptualize the scope of this publication. The methodology as well as the implementation as software were also carried out by the candidate. Jens Neumanns supervised the modeling process and help in the organization of resources and equipment. Prof. Olaf Hinrichsen helped reviewing and editing the manuscript.

4.1 Introduction

To meet the increasingly stringent legislation regarding automotive emissions, the complexity of exhaust gas aftertreatment systems is increasing [67]. Modern gasoline engines usually contain at least two three-way catalysts (TWC) and a gasoline particulate filter (GPF), that is optionally also catalytically coated. To tailor the aftertreatment systems to a specific vehicle, accurate models that yield the catalytic performance, pressure drop and filtration performance of the system are necessary.

Depending on the purpose, models for exhaust gas aftertreatment are divided into distinct groups. Table 4.1 shows the different scopes and corresponding studies. Detailed micro-kinetic approaches aim to assist in the development of new materials or new structures, e.g. the addition of NO storage components [173]. Pore scale simulations of coated Gasoline Particulate filter (cGPF) analyze the washcoat deposition and the influence of the coating on the diffusion [110, 163]. The kinetics of these models are usually calibrated by synthetic gas test benches with simplified inlet feeds or via DFT (density function theory) calculations [49, 174, 175]. Because of the high computational effort and the broad parameter space, these approaches are not suitable for the simulation of transient driving cycles [176].

The second group of modeling approaches aims to assist in the system engineering of the exhaust gas aftertreatment[44, 126, 130, 187]. Hereby, macro-kinetic approaches utilizing global Langmuir-Hinshelwood kinetics capture the chemical behavior of the monolith. On a channel scale, the enthalpy and species transport is simulated in detail. In Table 4.1, these approaches are further divided to highlight the differences in the corresponding scope. Depending on the aim, some authors utilized only light-off measurements with simplified inlet feeds because their goal was e.g. to distinguish the effects of aging [43]. Other authors fitted their kinetics with measurements of the total vehicle [44, 185] but the low-pass deformations of the measurements influence the result [186]. Thus, kinetic parameters are usually calibrated with synthetic gas test benches, which produce a steady inlet feed for the catalyst with a higher accuracy. Under real-driving conditions on the other hand, the air-to-fuel ratio is oscillating around the stoichiometry point, due to the λ-control loop of combustion engines. When a high-frequency λ-oscillation is enforced, this operation is called dithering, which is grouped between drive cycle and light-off simulation in Table 4.1. Several studies already described the higher catalytic activity under dithering conditions [174, 193–197]. Dithering leads to two major differences compared to the results of corresponding steady-state operations. First, the light-off

Table 4.1: Key approaches for the simulation of TWCs and cGPFs with their corresponding scope. The aim of this work is to create a robust cGPF model suitable for light-offs, dithering and drive cycles, respectively.

Scale	Scope	TWC	cGPF
Micro-kinetic / pore scale	Fundamental characteristics	Balenovic et al. [177], Chatterjee et al. [49], Tischer et al. [124], Koči et al. [174], Xu et al. [178], Kota et al. [173], Stotz et al. [125]	Koči et al. [110], Greiner et al. [163], Belot et al. [103]
Macro-kinetic	Light-off	Voltz et al. [134], Koltsakis et al. [128], Kwon and coworker[131, 179], Kang et al. [43]	Opitz et al. [170], Allouche et al. [180]
	Dithering	Shamim et al. [181], Shamim [182], Su et al. [183], Zeng et al. [184]	
	Driving cycle	Holder et al. [126], Ramanathan and coworker [44, 185], Weilenmann, Della Torre et al. [187], Okajima et al. [46]	Mitsouridis et al. [133]
Control oriented	Real-time oxygen storage dynamics	Auckenthaler et al. [129], Kumar et al. [188], Bickel et al. [189], Guardiola et al. [190], Schürholz et al. [191]	Arunachalam et al. [192]

temperature is lower [198]. Second, the conversion efficiency after light-off is higher and the operating window with respect to the mean λ-values enlarges [199]. These important effects decrease the tailpipe emissions. Still, there are only few modeling approaches, which are all also focused on a conventional TWC [181, 184, 198, 200]. Mainly because of the wall flow, a cGPF has a different behavior than a TWC [201]. As can be seen in Table 4.1 only Mitsouridis et al. [133] simulated the transient catalytic performance of cGPFs. However, the authors did not validate their approach with measurements.

The third group of models is control orientated. These methods are often capable of real-time estimation of the current oxygen storage level using the λ-sensor or a raw exhaust gas composition model as input but are calibrated to a specific catalyst design[129, 189, 191]. Therefore, these approaches do not offer possibilities for design parameter variation. As can be seen in Table 4.1 for the relatively new cGPF technology, there are only few modeling approaches available yet.

The present work aims to close the gap between steady-state experiments and real-word driving scenarios for a cGPF. We develop a global reaction mechanism that can predict the steady-state light-off and high-load conversion in a broad λ-window and the behavior with highly transient inlet feed. The kinetic are embedded in a previously published filtration model that is extended for this purpose [95].

Measurements of a degreened cGPF on a specially equipped engine test bench yield a diverse data set, which is used to calibrate and validate the proposed reaction mechanism. An in-depth analysis of the behavior of the filter under dithering conditions shows how the dynamics of the oxygen storage and the coverage of the active centers affects the conversion.

4.2 Material and Methods

4.2.1 Applied Model Species

Starting with Voltz et al. [134], there have been many efforts to model the behavior of three-way-catalysts (TWC) with Langmuir-Hinshelwood-Hogen-Watson (LHHW) kinetics. The applied model species and the consideration of the oxygen storage mostly distinguish the mechanisms. Dubien et al. [202] proposed the partition of the various hydrocarbons (HC) into fast- and slow-oxidizing HC. This assumption was widely adopted by splitting the HC into C_3H_6 (fast HC) and C_3H_8 (slow HC) [44, 126, 128, 130]. Later, model approaches resume applying only one HC model species [133]. In order to verify this issue for our experimental setup, we have conducted an a priori experiment. Hereby, a FTIR-analyzer was used to distinguish the light-off behavior of different HC species of a commercial three-way catalyst on an engine test bench. Even though the results show a different behavior of the hydrocarbons depending on their structure similar to the work of Kang et al. [203], there is one HC species (ethene C_2H_4) that matches the light-off curve of the total hydrocarbons over a wide range of inlet feeds.

Figure 4.1 shows light-off curves for the total HC and C_2H_4, respectively. Over the wide range of inlet λ-values, C_2H_4 matches the total HC conversion measured by FID (flame ionization detector), which is the standard measurement device. Note that the negative conversion at low temperatures can be attributed to a formation of C_2H_4 via cracking. The low value can be explained by the low overall C_2H_4 fraction of 0.1 and 0.18. Due to the similarity of the C_2H_4 and the total HC characteristics, a splitting of the hydrocarbons into slow and fast does not seem necessary for the considered use case. Nevertheless, our

HC model species is still C_3H_6 because the calibration gas of the measurement equipment is propene. The deviation of reaction enthalpy of the HC-reaction per C-atom between propene and the complex HC-mixture is considered negligible.
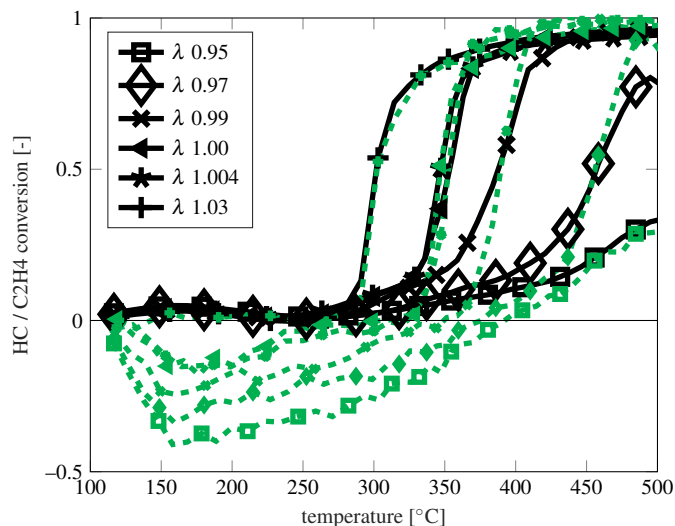
Figure 4.1: A priori study with a FTIR analyzer: total hydrocarbon measured by FID (black) compared with the C_2H_4 conversion (green) for steady-state light-offs at different λ-values.

4.2.2 Applied Reaction Mechanism

Table 4.2 shows the applied reaction pathways. We adopt established reactions for TWCs and include an oxygen storage model with two different ceria sites (fast, slow). The equilibrium of the OSC reactions [204, 205] and the water-gas-shift (WGS) and steam reforming (SR) reaction is considered via equilibrium constants, which are, in turn, a function of the Gibbs energy [206]. We group the reaction pathways into oxidation (R1-R4), NO reduction (R7-R11), ceria sites (R12-R21) and WGS or SR (R5-R6) reactions. It would be possible to add reactions for NH_3 [45, 185, 207] or CH_4. For the interested reader, the choice of model species and reaction pathways is further illustrated in the supplementary information. The direct reduction of NO with hydrogen is omitted, because it is a major pathway towards NH_3 [208], which is not in the scope of this study. Compared with the formation of NH_3, the direct reduction to N_2 is assumed to be negligible.

LHHW kinetics have in common that adsorption and desorption are assumed to be in equilibrium. Under highly transient conditions, this assumption will no longer be valid. Therefore, to include the effects of transient adsorption-desorption, the model should

Table 4.2: Reaction pathways.

	Reaction	Rate law
R1	$CO + 0.5O_2 \rightarrow CO_2$	$\dot{r}1 = \phi_{wsc} \cdot k_1 c_{CO} c_{O_2}/G1$
R2	$H_2 + 0.5O_2 \rightarrow H_2O$	$\dot{r}2 = \phi_{wsc} \cdot k_2 c_{H_2} c_{O_2}/G1$
R3	$C_3H_6 + 4.5O_2 \rightarrow 3CO_2 + 3H_2O$	$\dot{r}3 = \phi_{wsc} \cdot k_3 c_{C_3H_6} c_{O_2}/(G1 \cdot G2)$
R4	$CH_4 + 2O_2 \rightarrow CO_2 + 2H_2O$	$\dot{r}4 = \phi_{wsc} \cdot k_4 c_{CH_4} c_{O_2}/(G1 \cdot G2)$
R5	$CO + H_2O \rightleftharpoons CO_2 + H_2$	$\dot{r}5 = \phi_{wsc} \cdot \xi (k_5 c_{CO} c_{H_2O} - \frac{k_5}{K_{WGS}} c_{CO_2} c_{H_2})/G1$
R6	$C_3H_6 + 3H_2O \rightleftharpoons 3CO + 6H_2$	$\dot{r}6 = \phi_{wsc} \cdot (k_6 c_{C_3H_6} c_{H_2O} - \frac{k_6}{K_{SR}} c_{CO} c_{H_2})/G3$
R7	$CO + NO \rightarrow CO_2 + 0.5N_2$	$\dot{r}7 = \phi_{wsc} \cdot k_7 c_{CO} c_{NO}/(G1 \cdot G2)$
R8	$C_3H_6 + 9NO \rightarrow CO_2 + 0.5\,N_2$	$\dot{r}8 = \phi_{wsc} \cdot k_8 c_{NO} c_{C_3H_6}/(G1 \cdot G2)$
R9	$H_2 + N_2O \rightarrow H_2O + N_2$	$\dot{r}9 = \phi_{wsc} \cdot k_9 c_{H_2} c_{N_2O}/G1$
R10	$CO + 2NO \rightarrow CO_2 + N_2O$	$\dot{r}10 = \phi_{wsc} \cdot k_{10} c_{CO} c_{NO}/G1$
R11	$CO + N_2O \rightarrow CO_2 + N_2$	$\dot{r}11 = \phi_{wsc} \cdot k_{11} c_{CO} c_{N_2O}/G1$
R12	$0.5O2 + fCe_2O_3 \rightarrow 2fCeO_2$	$\dot{r}12 = \phi_{wsc} \cdot \Gamma_{fast} \cdot k_{12} c_{O_2} (1 - \Theta_{fast})$
R13	$H_2 + 2fCeO_2 \rightleftharpoons fCe_2O_3 + H_2O$	$\dot{r}13 = \phi_{wsc} \cdot \Gamma_{fast} \cdot (k_{13} c_{H_2} \Theta_{fast} - \frac{k_{13}}{K_{eq}} c_{H_2O} (1 - \Theta_{fast}))$
R14	$CO + 2fCeO_2 \rightleftharpoons fCe_2O_3 + CO_2$	$\dot{r}14 = \phi_{wsc} \cdot \Gamma_{fast} \cdot (k_{14} c_{CO} \Theta_{fast} - \frac{k_{14}}{K_{eq}} c_{CO_2} (1 - \Theta_{fast}))$
R15	$C_3H_6 + 12fCeO_2 \rightarrow 6fCe_2O_3 + 3CO\ 3H_2O$	$\dot{r}15 = \phi_{wsc} \cdot \Gamma_{fast} \cdot k_{15} c_{C_3H_6} \Theta_{fast}$
R16	$NO + fCe_2O_3 \rightarrow 2fCeO_2 + 0.5N2$	$\dot{r}16 = \phi_{wsc} \cdot \Gamma_{fast} \cdot k_{16} c_{NO} (1 - \Theta_{fast})$
R17	$0.5O_2 + Ce_2O_3 \rightarrow 2CeO_2$	$\dot{r}17 = \phi_{wsc} \cdot \Gamma_{slow} \cdot k_{17} c_{O_2} (1 - \Theta_{slow})$
R18	$H_2 + 2CeO_2 \rightleftharpoons Ce_2O_3 + H_2O$	$\dot{r}18 = \phi_{wsc} \cdot \Gamma_{slow} \cdot (k_{18} c_{H_2} \Theta_{slow} - \frac{k_{18}}{K_{eq}} c_{H_2O} (1 - \Theta_{slow}))$
R19	$CO + 2CeO_2 \rightleftharpoons Ce_2O_3 + CO_2$	$\dot{r}19 = \phi_{wsc} \cdot \Gamma_{slow} \cdot (k_{19} c_{CO} \Theta_{slow} - \frac{k_{19}}{K_{eq}} c_{CO_2} (1 - \Theta_{slow}))$
R20	$C_3H_6 + 12CeO_2 \rightarrow 6Ce_2O_3 + 3CO\ 3H_2O$	$\dot{r}20 = \phi_{wsc} \cdot \Gamma_{slow} \cdot k_{20} c_{C_3H_6} \Theta_{slow}$
R21	$NO + Ce_2O_3 \rightarrow 2CeO_2 + 0.5N_2$	$\dot{r}21 = \phi_{wsc} \cdot \Gamma_{slow} \cdot k_{21} c_{NO} (1 - \Theta_{slow})$
R22	$PGM \rightleftharpoons PGM - O$	$\dot{r}22 = k_{22} \cdot (1 - \xi) c_{Ox} - k_{23} \cdot \xi \cdot c_{Red}$

include the time-dependent surface coverage of each species on the active sites as well as the resulting extent of oxidation of the active centers after prolonged exposure. But as stated above, these detailed models are unsuited for application or model design purposes because of their high computational effort and the high number of kinetic parameters to estimate.

In order to capture the core of the catalyst dynamic behavior, Koltsakis et al. [127] as well as Arvajová et al. [209] introduced an oxidation extent of the active centers in their models. Koltsakis et al. [127] applied an empirical Rh-oxidation status to capture catalyst transient behavior. They stated that the typical PGM and oxygen storage materials (OSM) are active for WGS as long as the catalyst's surface sustained some extent of oxidation [210–212]. Therefore, they scaled the WGS reaction with a factor that corresponds to the fraction of Rh-sites that are oxidized.

Similar to the work of Koltsakis et al. [127], we apply a factor ξ to capture the catalyst transient behavior in a global model. If the surface is completely covered by reductive species (CO,C_3H_6,H_2), then ξ is 0. Contrarily, if the surface is covered by oxidative species (O_2, NO,N_2O), ξ is 1. At these points, we assume that the adsorption is at its

equilibrium. In between these two points, the impact of the inhibition is reduced and the catalyst is more active. A prolonged exposure to a rich inlet feed decreases ξ and at the same time increases the impact of inhibition due to CO and HC. Equation (4.1) and (4.2) show the implementation of the factors $K_{\xi,Ox}$ and $K_{\xi,Red}$ with the considered model species. The empirical additions of Voltz et al. [134] are removed similar to the work of Ramanathan et al. [44] and the resulting terms are extended by the dynamic impact of ξ.

$$G1 = \left(1 + \frac{K_1 c_{CO} + K_2 c_{C_3H_6}}{1 + K_{\xi,Ox} \cdot \xi} + \frac{K_3 c_{NO}}{1 + K_{\xi,Red} \cdot (1-\xi)}\right)^2 \tag{4.1}$$

$$G2 = 1 + \frac{K_4 c_{O_2}}{1 + K_{\xi,Red} \cdot (1-\xi)} \tag{4.2}$$

Note that the SR reaction has an individual inhibition factor similar to the work of Holder et al. [126], since dithering does not influence it:

$$G3 = (1 + K_5 c_{C_3H_6}) \tag{4.3}$$

The inhibition constants K_i are determined via Equation (4.4) with the parameters A and H_{Ad} stated in the supporting information.

$$K_i = A_i \cdot exp(\frac{H_{Ad,i}}{R \cdot T}) \tag{4.4}$$

The empirical factor ξ changes over time depending on the gas composition in the same manner as in Koltsakis et al. [127]. Reductive and oxidative species are lumped according their oxygen balance:

$$c_{ox} = 2c_{O_2} + c_{NO} + c_{N_2O} \tag{4.5}$$

$$c_{red} = c_{CO} + 9c_{C_3H_6} + 4c_{CH_4} + c_{H_2} \tag{4.6}$$

The gradient of ξ is then determined via two Arrhenius type rate constants k_{red} and k_{ox}:

$$\frac{d\xi}{dt} = k_{ox} \cdot c_{ox} \cdot (1-\xi) - k_{red} \cdot c_{red} \cdot \xi \tag{4.7}$$

We assume that the capacity of the PGM surface is very small compared to the OSM capacity. Therefore, in contrast to the ceria reactions no coupling between ξ and the species balance is done.

4.2.3 Model Structure
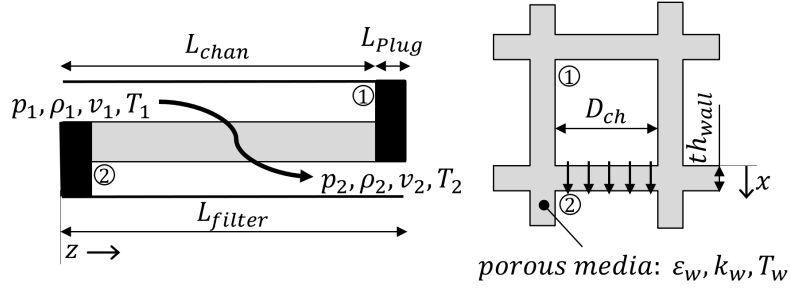
Figure 4.2: Model description.

In order to model the chemical behavior of a cGPF, we extend our previously published GPF model [95]. A reactor model solves the governing equations for the conservation of energy, species and momentum for one representative pair of an inlet and an outlet channel and the separating porous wall as can be seen in Figure 4.2. Whereas the species conservation and, with it, the oxidation status of the oxygen storage is treated as transient, the fluid energy and momentum balance are solved quasi-steady, leading to a significant decrease in computation time. For the solid temperature, an increased time step is applied because of the lower gradients compared to the species balance. The fluid is assumed as incompressible and a constant pressure boundary of 1.2 bar is applied downstream of the outlet channel.

Following a 1D+1D approach [133, 169, 170], the channel pair and the wall are discretized in axial and through-wall direction. All quantities including the homogeneous wall temperature are calculated on this grid. In the following equations, the index j is 1 for the inlet channel and 2 for the outlet channel. Equation (4.8) couples the channel velocity v_j with the wall velocity v_w via the contunuity equation:

$$D_j^2 \frac{\partial \rho_j v_j}{\partial z} = (-1)^j \cdot 4 D_j \cdot \rho_j \cdot v_w \tag{4.8}$$

In the channels, no radial deviation of the pressure is considered. Therefore, the 1D-pressure profile p is determined by:

$$\frac{\partial p_j}{\partial z} = -\beta_j(Re_w) \cdot \frac{\partial(\rho_j \cdot v_j^2)}{\partial z} - 2 \cdot \frac{\eta_j}{D_j^2} \cdot C_{f,j}(Re_w) \cdot v_j \qquad (4.9)$$

The coefficient β and the friction coefficient $C_f(Re_w)$ are interpolated using the tables provided by Bissett et al. [153]. The wall Reynolds number Re_w has an upper bound of three as recommended in the literature [153, 171]. The channels are coupled via Darcy's law (4.10).

$$p_1 - p_2 = \eta \cdot \frac{v_w}{k_w} \cdot t_w \qquad (4.10)$$

The permeability k_w is fitted to pressure drop measurements. The additional pressure loss due expansion and contraction at the filter's inlet and outlet are determined with Equation (4.11).

$$\Delta p_j = \frac{\zeta_j}{2\rho_j} \cdot (\frac{\dot{m}}{D_j^2})^2 \qquad (4.11)$$

Here the local resistance coefficient ζ_j is set to 1.25 according to Leskovjan et al. [162]. The heat transfer coefficient h is derived via the Nusselt correlation of Bissett et al. [153]. The porous media is assumed as homogeneous, and the ideal gas law is used. All material properties, e.g. viscosity, heat capacity or diffusion coefficients are calculated with correlations from the VDI Heat Atlas [155].

The channel gas phase temperature is assumed quasi-steady:

$$c_p\rho_j v_j \cdot \frac{\partial T_j}{\partial z} = \frac{4}{D_j} \cdot (h_j + (-1)^j \cdot c_p\rho_j v_w) \cdot (T_w|_{x=-(1-j) \cdot t_w} - T_j) \qquad (4.12)$$

In the wall, the solid temperature is derived by:

$$\rho c_w \frac{\partial T_w}{\partial t} = \lambda_s \cdot \frac{\partial^2 T_w}{\partial z^2} + \lambda_s \cdot \frac{\partial^2 T_w}{\partial x^2} + \frac{v_w \rho_w c_p \partial T_w}{\partial x} + \Sigma \dot{r}_i \cdot H_B^0 \qquad (4.13)$$

with ρc_w as the thermal mass of the wall defined by Equation (4.14).

$$\rho c_w = (1 - \varepsilon_w)\rho_s c_s + \varepsilon_w \rho_w c_p \qquad (4.14)$$

To achieve consistency between the channel and wall modeling, the through-wall enthalpy flux term is set to

$$\rho c_w \frac{\partial T_w}{\partial x}\Big|_{x=-(1-j)\cdot t_w} = \frac{4}{D_j} \cdot (h_j + (-1)^j \cdot c_p \rho_j v_w) \cdot (T_w|_{x=-(1-j)\cdot t_w} - T_j) \qquad (4.15)$$

at the boundaries.

The species balance is solved fully transient in the channels:

$$\frac{\partial c_j}{\partial t} = -v_j \cdot \frac{\partial c_j}{\partial z} - \frac{4}{D_j} \cdot (k_j \cdot (c_j - c_w|_{x=-(1-j)\cdot t_w}) + (-1)^j \cdot v_w \cdot c_j) \qquad (4.16)$$

with the mass transfer coefficient k derived from the Sherwood correlation of Bissett et al. [153]. In the wall, radial diffusion is considered via an effective diffusion coefficient D_{eff}. The species balance in the wall, given in Equation (4.17) with $\dot{r}$ as the reaction rate of the respective species, is determined by the reaction network of Table 4.2.

$$\frac{\partial c_w}{\partial t} = \frac{\partial (v_w \cdot c_w)}{\partial x} - D_{eff} \cdot \frac{\partial^2 c_w}{\partial x^2} + \dot{r} \qquad (4.17)$$

In analogy to the enthalpy balance, the boundary conditions are set to

$$D_{eff} \cdot \frac{\partial c_w}{\partial x}\Big|_{x=-(1-j)\cdot t_w} = k_j \cdot (c_w|_{x=-(1-j)\cdot t_w} - c_j) \qquad . \qquad (4.18)$$

For effective diffusion coefficient D_{eff}, the parallel pore model is used:

$$D_{i,eff} = D_{i,M} \cdot \frac{\varepsilon_w}{\tau} \qquad (4.19)$$

Here, $D_{i,M}$ is the diffusion coefficient of the species i in the mixture, ε_w is the current void fraction of the substrate, including possible effects of soot or coating, and τ is the tortuosity, which is an empirical correction factor. The calculated $D_{i,eff}$ corresponds well to the measured values of Kröcher et al. [213].

All governing equations are solved in Matlab. For the momentum and overall mass balance Equation (4.8) to Equation (4.10), the solver bpv4c is applied. The quasi-steady enthalpy balance in the channels (Equation (4.12)) is solved via ode15s and coupled with the mass and momentum balance with a recursive scheme due to faster performance and better stability. These solvers are triggered if the gradients of the inlet mass flow, the

inlet temperature or the wall temperature exceed a defined threshold. A method of lines approach with the 1D+1D discretization of the channel pair integrates Equation (4.12)-(4.18) for the species and enthalpy balance utilizing the solver ode15s. For a faster performance, the sparsity patterns of the corresponding Jacobi matrix are supplied and the order is set to two. Additionally, all quantities are normalized to the same order of magnitude to achieve consistent tolerances.

4.2.4 Measurement Setup
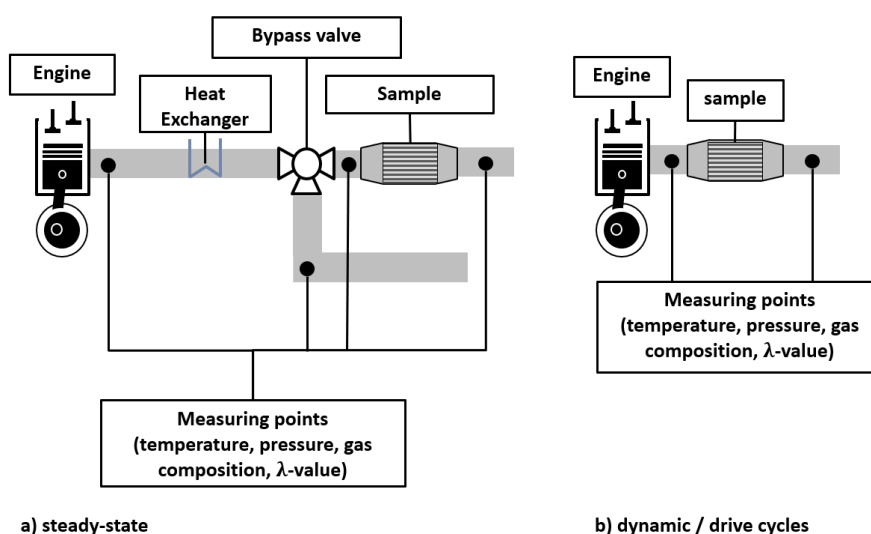
Figure 4.3: Measurement setup.

A dynamic engine test bench equipped with a direct injection spark ignition gasoline research engine was used for all measurements in this study. The key technologies of the engine are exhaust gas turbocharging, a fully variable valvetrain, and gasoline direct injection with homogeneous operation. Figure 4.3 shows the two measurement configurations. An underfloor positioning (4.3 a) allows controlled measurements with slow temperature ramps similar to catalyst test benches with synthetic gas. During drive cycle tests, the cGPF is attached in a close-coupled position (4.3 b) to achieve realistic temperature dynamics. Note that the λ-control of the engine is not adapted to the cGPF.

Table 4.3 summarizes the conducted experiments with their respective conditions. For the steady-state light-offs, the valve is switched to the bypass-stream, and the engine is set to a low-load operation point. When the bypass valve is switched to the cGPF, the exhaust gas system between the valve and the sample is at ambient temperature. Then, the engine is set to the steady-state point applied for the light-off. Because of the thermal inertia as

Table 4.3: Conditions in the experiments.

Experiment	Inlet Temperature [°C]	Mass flow [kg·h^{-1}]	λ [-]	GHSV [h^{-1}]	Setup	Figure
steady-state light-off	20 - 450	115	0.97-10.3	5.42E+04	(a)	4.4 a,d
steady-state λ-sweep at medium load	≈600	260	0.92-1.06	1.22E+05	(a)	4.4 e
steady-state λ-sweep at high load	≈780	460	0.92-1.05	2.17E+05	(a)	4.4 f
dithering λ-sweep at medium load	≈600	260	0.99-1.012 ±2% at 1.5 Hz	1.22E+05	(a)	4.5 a, 10
dithering λ-sweep at high load	≈780	460	0.99-1.011 ±2% at 1.5 Hz	2.17E+05	(a)	4.5 b, 10, 11
dithering light-off	20 - 450	115	0.99 ±2% at 1.5 Hz	5.42E+04	(a)	4.5 a
dynamic light-off	110 - 450	115	0.99 ±2% at 1.5 Hz	5.42E+04	(a)	4.55 b
oxygen storage	≈590	120	0.9-1.05	5.65E+04	(a)	4.7
WLTP cycle	20 - 650	0-200	0.9-16	0- 9.42E+04	(b)	4.8, 4.9

well as supported by the active cooling of a heat exchanger, the temperature in front of the sample increases at a constant rate of $0.4\,\text{K}\cdot\text{s}^{-1}$. This allows the measurement of a quasi-steady light-off with an engine test bench. For a more dynamic light-off with temperature ramps of $28\,\text{K}\cdot\text{s}^{-1}$, the engine is set to a higher load operation during the pre-treatment, thus the exhaust gas system up to the bypass valve is already hot and the thermal inertia of this part is negligible. Additionally, the coolant flow of the heat exchanger is switched off.

The two-line exhaust gas analyzer system (Horiba Mexa 7000) allows the measurement of the gas composition simultaneously at the filter's inlet and outlet. The system measures the hydrocarbons via flame ionization detection (FIA726-N), the oxygen concentration via paramagnetic oxygen sensor (MPA-720), the NO and content with chemiluminescence (CLA-750-A) and CO, CO_2 and N_2O via non-dispersive infrared spectroscopy (AIA-72). Two additional mass spectrometers (Balzers HLT260) determine the H_2 concentration. Six universal exhaust gas oxygen sensors (UEGO) deliver the λ-value. Additionally, six fast heated exhaust gas sensors (HEGO) can differentiate between lean and rich gas composition. When these signals are compared with the simulation, the λ-value is determined by the gas composition with the stoichiometric relationship [129]

$$\lambda = \frac{2 \cdot O_2 + NO + N_2O + 2 \cdot CO_2 + H_2O}{CO + H_2 + 9 \cdot C_3H_6 + 4 \cdot CH_4 + 2 \cdot CO_2 + H_2O} \qquad . \tag{4.20}$$

The steady-state results are analyzed with their conversion X, which is defined as

$$X = 1 - \frac{y_j^{out}}{y_j^{in}} \qquad . \tag{4.21}$$

For transient data, the normalized outlet emissions (NOE) in Equation (4.22) as well as the normalized cumulative outlet emissions (NCOE) in Equation (4.23) are used to normalize the shown results to the measured inlet and outlet data, respectively.

$$NOE = \frac{w_j^{out,sim}}{w_j^{out,meas}} \tag{4.22}$$

$$NCOE = \left(\frac{1}{\int_{t_0}^{t_{end}} \dot{m} \cdot w_j^{in} dt}\right) \cdot \int_{t_0}^{t} \dot{m} \cdot w_j^{out} dt \tag{4.23}$$

The measurement values in front of the filter are applied as inlet conditions for the simulation. In the case of high-frequency λ-oscillation an additional preprocessing step is necessary because the time response of the gas analyzers is not fast enough. This method is explained in the supplementary information.

4.2.5 Used Filter

For calibration and validation purposes, the catalytic performance of a single industrially available, in-wall coated GPF was determined. Before the measurements, the filter is degreened using a degreening run, which consists of one hour of high load driving (up to $500 \, \mathrm{kg \cdot h^{-1}}$ at $750 \, \mathrm{°C}$) on the engine test bench. Table 4.4 shows the material data.

Table 4.4: Filter characteristics for substrates used in this study.

diameter [mm]	136
length, L [mm]	120
cell density [cpsi]	300
wall thickness, th [mil]	8
porosity, ε_{bare} (prior to coating) [-]	0.64
tortuosity, τ [-]	3.5
washcoat loading [g/l]	75
washcoat volume fraction, ϕ_{wsc} [-]	0.17
porosity, ε_w [-]	0.47
PGM ratio Pt:Pd:Rh [-]	0:7:2
permeability, k_w [m^2]	3.08E-13
density, ρ [kg/m^3]	2500
heat capacity, c [J/kg·K] (see [126])	$\dfrac{-3.44\cdot10^7[\frac{\text{K}\cdot\text{J}}{\text{kg}}]}{T^2} + 1071[\frac{\text{J}}{\text{kg}\cdot\text{K}}] + 0.156[\frac{\text{J}}{\text{kg}\cdot\text{K}^2}]\cdot T$

4.3 Results and Discussion

4.3.1 Determination of the kinetic parameters

4.3.1.1 Steady-State

In order to fit the kinetic parameters to the measurement results, parameters from several sources [44, 126, 131, 185] are used as initial values. The kinetic parameters are then adjusted in three steps. In a first broad search, a particle swarm optimization algorithm [214] delivers the starting point for the second step which is a genetic algorithm optimizer. The particle swarm optimization in the first step is better suited to search broad parameter spaces, whereas the genetic algorithm yields the better convergence towards a minimum [215]. In a last step the *fminsearch* function of Matlab, utilizing the Downhill-Simplex algorithm, calibrates the parameters in a more narrow range [216]. The definition of the objective function and the resulting set of kinetic parameters can be found in the supplementary data.

The experimental results yield a diverse set of calibration data in a broad λ- and temperature range with the addition of steady-state measurements at oscillating λ. Note that a more accurate model fit would be possible with a smaller set of measurement data, e.g. only stoichiometric light-offs as often shown in the literature (see Table 4.1). However,

(a) LO at λ: 0.97

(b) LO at λ: 0.99

(c) LO at λ: 1.005

(d) LO at λ: 1.03

(e) λ-scan at 260 kg·h^{-1}

(f) λ-scan at 460 kg·h^{-1}
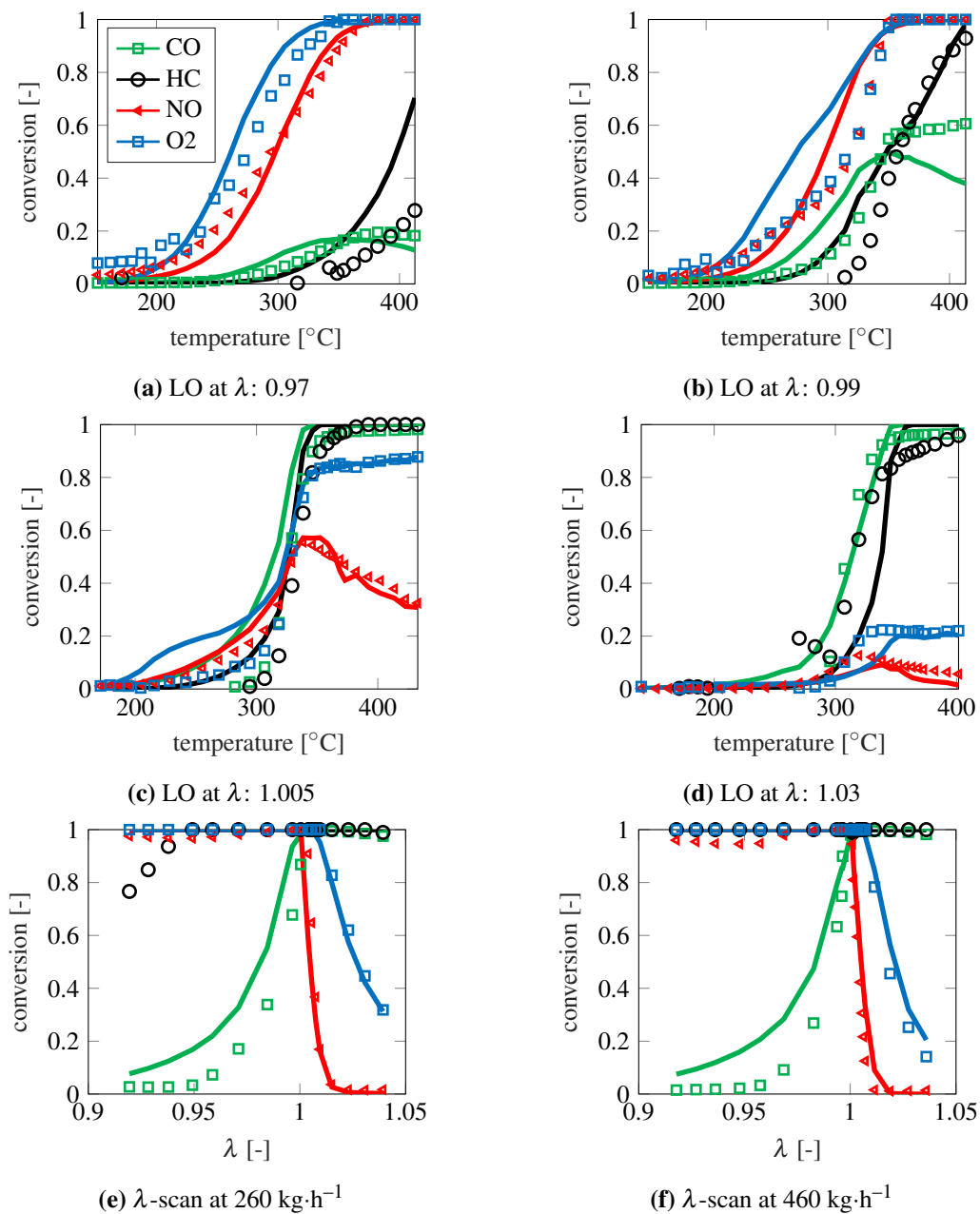
Figure 4.4: Model calibration: quasi-steady-state light-off at 115 kg·h^{-1} for different λ-values and λ-scans at 260 kg·h^{-1} and 460 kg·h^{-1}. Measurement results are symbols and simulation results are lines.

we choose to obtain a more global model, aiming at robust application in a wide range of operating conditions.

Figure 4.4 shows the comparison between measurement and simulation of light-off curves at different λ-value with a constant mass flow of $115 \, kg \cdot h^{-1}$. Already at low temperatures, the λ-value of the inlet feed has a great impact on the results. In a rich regime, the reduction of NO and O_2 begins at lower temperature than at lean operations. After the light-off, stoichiometry dictates the maximum available conversion. Taking into account the diversity of the data set, the model yields a high quality of prediction for the relevant emission species CO, HC and NO. In addition to the light-offs, the bottom part of Figure 4.4 depicts two λ-sweeps at different mass flows and approximately at $600 \, °C$ and at $780 \, °C$, respectively. The temperature depends on the engine exhaust gas temperature under these working conditions. Here, the prediction quality is significantly high. Only at rich conditions, the decrease in NO conversion (Figure 4.4) and HC conversion (Figure 4.4e) is not predicted correctly. An improved model prediction for HC could likely be achieved by adding a ξ-dependent term to G_3 (Equation (4.3)). However, the small potential increase in accuracy is not seen worth the increase of the parameter space. Additional information on the H_2 and N_2O model prediction can be found in the supplementary information.

Stationary experiments are easier to calibrate, due to their faster computation time and stable inlet feeds. In realistic driving scenarios however, the λ-value of the exhaust gas periodically changes due to the engine's λ-control loop. Applying a fast modulation of the λ-signal during the experiment, the so-called dithering [193], yields a more realistic inlet feed. This inlet feed is closer to practical operations but still allows in-depth analysis because of constant mass flow and temperature. Therefore, besides the steady-state feed conditions, several experiments under dithering conditions are utilized. These measurement results are not used for the calibration of the PGM kinetics but rather of the OSC model and the PGM redox model. A direct comparison of these steady-state experiments with and without λ-modulation is added in the supplementary information.

The experiment shown in Figure 4.5 is similar to the λ-sweeps in Figure 4.4 e,f with the difference that the inlet feed's λ-value oscillates. The x-axis value is the mean λ-value that is modulated with an amplitude of 2.5% at a frequency of $1.5 \, Hz$. Similar to the trends reported by Gong et al. [199] the conversion window of NO on the lean side enlarges because of the λ-oscillation.
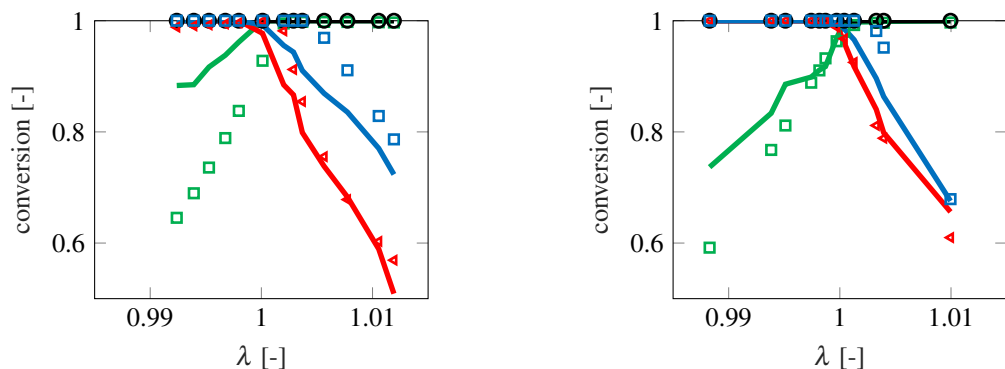
(a) λ-scan from rich to lean at $230\,\text{kg}\cdot\text{h}^{-1}$.   **(b)** λ-scan from rich to lean at $460\,\text{kg}\cdot\text{h}^{-1}$.

Figure 4.5: Measured and simulated λ-scan at $230\,\text{kg}\cdot\text{h}^{-1}$ and $460\,\text{kg}\cdot\text{h}^{-1}$. Solid lines represent simulations, dashed lines represent measurement results. The inlet feed has an oscillating λ-value (2.5% 1.5 Hz).

The PGM redox submodel's parameters are adjusted via a light-off experiment at dithering conditions with an averaged λ-value of 0.99. This value achieves a periodically cycling between rich and lean inlet feeds. The dominant coverage of the active centers therefore switches from oxidative to reductive species and no complete equilibrium is reached. A comparison between the measurement and the simulation is shown in Figure 4.6 a. In accordance to the measurement, a rapid light-off of all important species at roughly the same temperature is achieved. Additionally, Figure 4.6 b depicts a transient light-off with the same inlet feed as for the steady-state light-off but a temperature increase of $28\,\text{K}\cdot\text{s}^{-1}$ for validation purposes. Only moderate accuracy is achieved here. A possible explanation could be an increased mass and heat transfer at the front part of the filter due to developing flow. The applied correlations for the Nusselt and Sherwood numbers of Bissett et al. [153] do not include effects of developing flow. An sensitivity study revealed that an increase of the heat and mass transfer in the front part of the inlet channel decreases the simulated NCOE. If this increase is applied at a steady-state Light-Off however, the impact is negligible due to the more even distribution of temperature in the steady case.

Lastly, the oxygen storage kinetics are determined with low frequency λ-jumps. For this, the λ-value switches periodically between 0.9 for 6 s and 1.05 for 3 s. Figure 4.7 shows the model prediction of the cumulative outlet emissions. The dynamics of the measurement is better resolved by the UEGO and HEGO sensors. Their results and the corresponding simulations, gained by applying equation (4.20) on the predicted outlet emissions, are shown in Figure 4.7 b. The modeled and measured tailpipe λ-value are similar. Only during the rich phases the simulation deviates strongly from the measurement characteristics. This can be attributed to the cross sensitivity of the UEGO-sensor to hydrogen. An alternative explanation is the oxidation of the oxygen storage by water
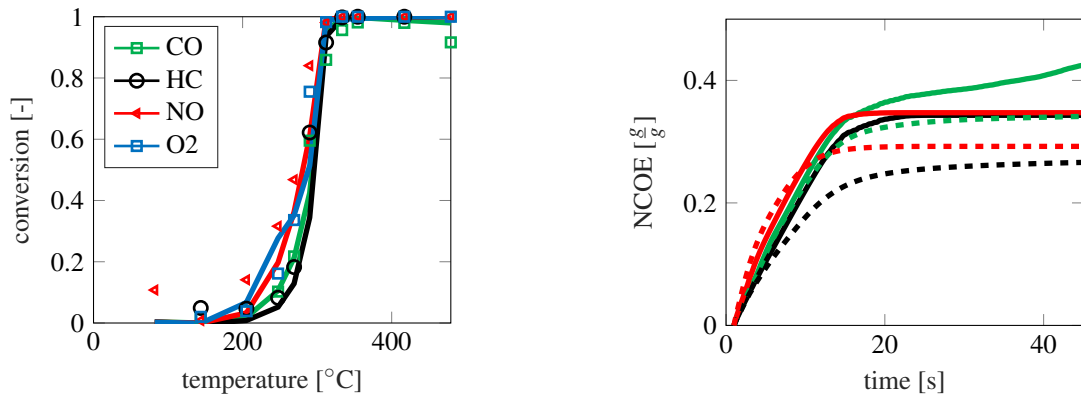
(a) Quasi-steady light-off (0.4 K·s^{-1}).

(b) Transient light-off (28 K·s^{-1})

Figure 4.6: Measured and simulated light-off at 115 kg·h^{-1}. Solid lines represent simulations, dashed lines or symbols depict the measurement results. The inlet feed has an oscillating λ-value (2.5%, 1.5 Hz).

or CO_2 [189], which leads to a lower outlet than inlet λ-value for a short period of time. However, when the equilibrium is reached, the λ-value will approach the inlet feed's λ-value.
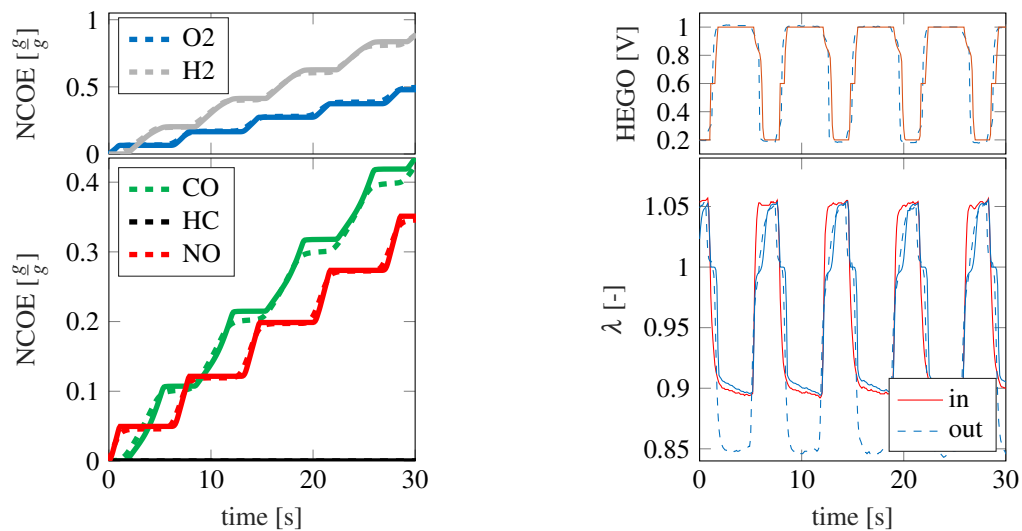
(a) Normalized cumulative outlet emissions (NCOE) to the inlet feed.

(b) Simulated vs. measured λ-sensor signal.

Figure 4.7: Simulation (solid lines) and measurement (dashed lines) of an OSC experiment. The measured inlet λ-value is also plotted (solid line).

4.3.1.2 Application on Drive Cycles

In order to gain a robust, predictive model, separate validation and calibration data are necessary. In our case, we apply the (pseudo-) steady-state experiments for calibrations

as shown above and present here the validation of the model with a WLTP drive cycle. Figure 4.8 shows a zoom of the first 70 s of the cycle. The model prediction of the main pollutants are close to the measurement results regarding the cumulative emissions as well as the peak height. The spatially averaged ξ-values in Figure 4.8 c depict that from an oxidized starting value reducing species rapidly cover the active centers until the light-off around 20 s. Then, the fast ceria sites are also active and the θ_{fast} characteristics shows oxygen storage. The θ_{slow} characteristics shows less dynamic behavior and only increases during a fuel cut at 45 s.
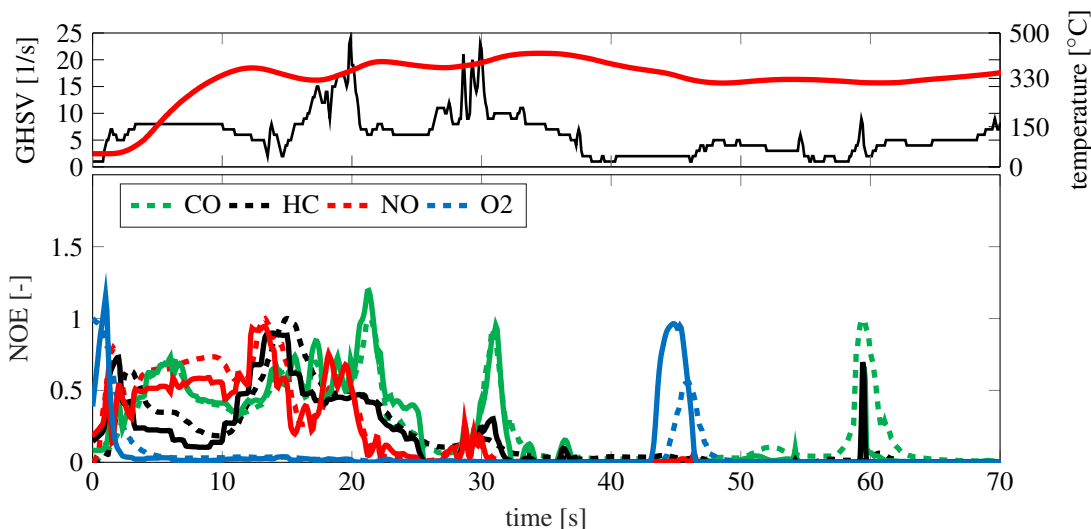
(a) Normalized outlet emissions (NOE) to the inlet feed.
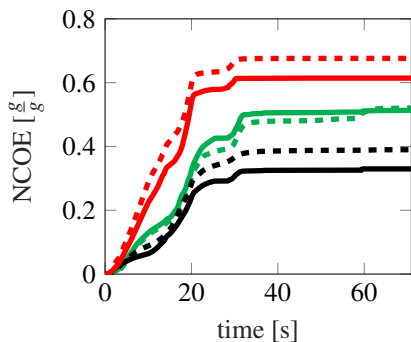
(b) Normalized cumulative outlet emissions (NCOE) to the inlet feed.
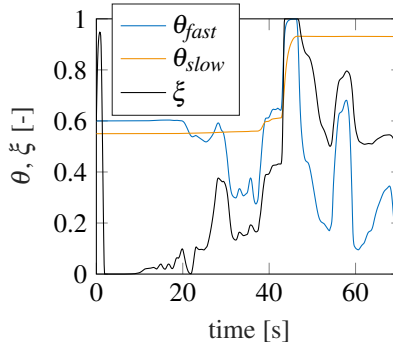
(c) Spatially averaged θ and ξ values.

Figure 4.8: First 70 s of a WLTP cycle: measurement results are depicted as dashed lines and simulations are represented as solid lines.

Figure 4.9 shows the analysis of the complete cycle. For a better readability, only the NCOE values are shown. The gap between the model prediction and the measurement results is increasing over time, because the plot represents the cumulative emission level. Here, single deviations are integrated over time as well. The top of Figure 4.9 shows

the measured and predicted outlet temperature in addition to the inlet conditions of the temperature and the *GHSV*. Due to the assumption of an adiabatic system, the predicted temperature is sightly above the measured one. Considering that no drive cycle is in the calibration data, it can be stated that good quality is achieved.
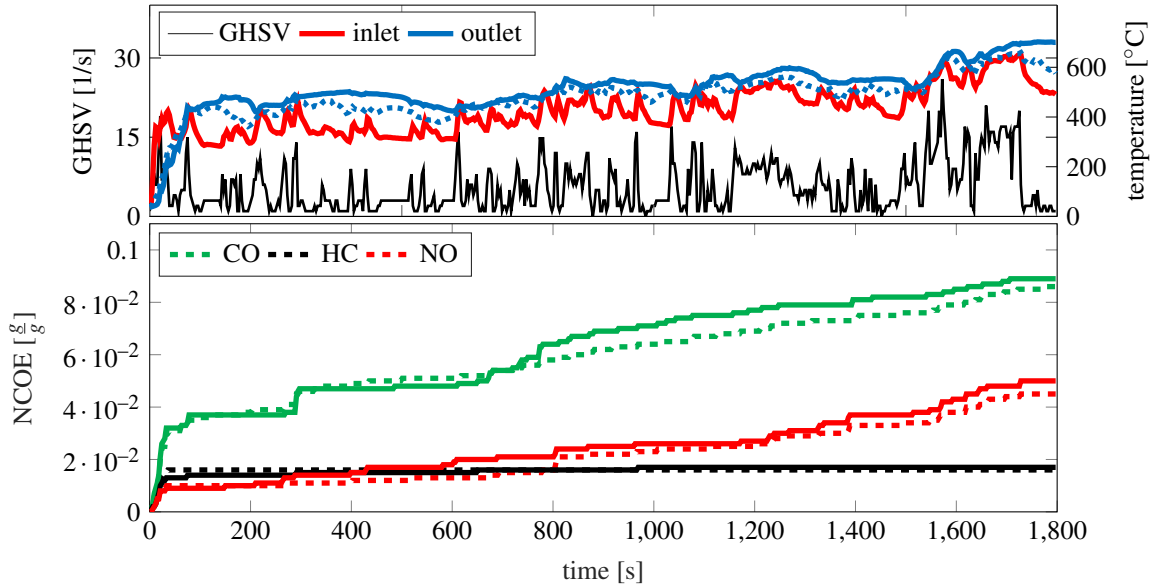
Figure 4.9: Measured and simulated WLTP cycle (measurement results are depicted as dashed lines, the corresponding simulations are depicted as solid lines).

4.3.2 Impact of λ-Oscillations

The application of λ-oscillations (dithering) to influence the conversion at high-load conditions and accelerate the light-off has been discussed by several authors [174, 193–197]. To simulate the catalysts response to dithering, different modeling approaches ranging from an increased NO adsorption [184] to reduced activation energies [181, 200] has been applied. To the author's knowledge, the present approach is the first global reaction mechanism to include and explain the impact of dithering during light-off as well as at warm operation. We assume that there are two different phenomena. Whereas the enlarged conversion window for NO under dithering conditions is an oxygen storage effect, the faster light-off is unlikely to be an OSC phenomenon, since the ceria reactions are only active at higher temperatures than the catalyst light-off [126, 206]. Therefore, we model the enhanced catalytic activity with a decreased impact of competing reactions by capturing the dynamics of the surface coverage via an empirical factor ξ.
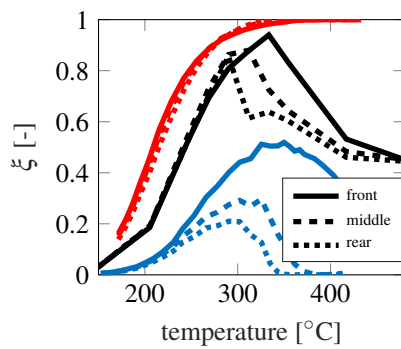
(a) ξ-values for steady-state light-off with and without λ-oscillations.
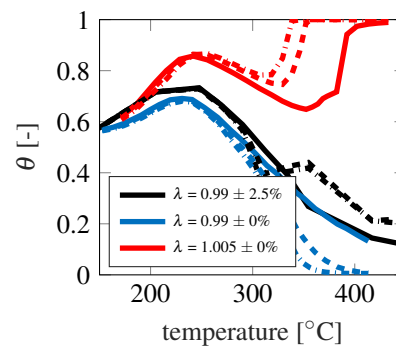
(b) Corresponding θ-values.
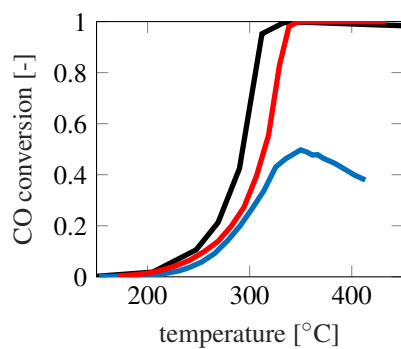
(c) Comparison of the simulated CO conversion.
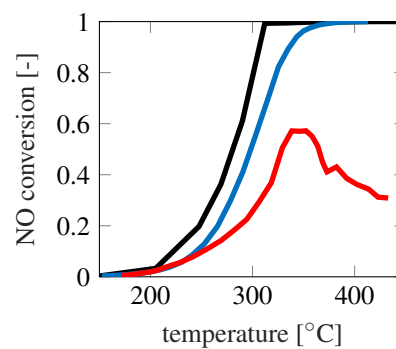
(d) Comparison of the simulated NO conversion.

Figure 4.10: Influence of the inlet λ on the simulated ξ and θ values: Comparison of steady-state light-offs at dithered $\lambda = 0.99 \pm 2.5\%$ and at constant $\lambda = 0.99$ and $\lambda = 1.005$.

Figure 4.10 shows the simulation results of the light-offs with static λ-values at slightly rich and lean conditions as well as the corresponding dithering experiment. The light-off under dithering condition (black lines in Figure 4.10 c,d) reaches the highest NO and CO conversion. Gong et al. [199] as well as Bounechada et al. [195] detected a similar behavior. The latter suggested that the noble metals reach a more active oxidation state under dithering conditions. In order to capture the measured characteristics in our modeling, dithering keeps the extent of reduced or oxidized active centers in a medium range (4.10 a). The higher catalytic activity under dithering conditions is then reproduced with a reduced inhibition due to CO and NO / O_2 respectively.

The enhanced CO conversion at high temperature in case of dithering can be explained with the more active water-gas-shift reaction, which we scaled with ξ (see Table 4.2). The oxygen storage θ, shown in Figure 4.10 b, does not influence the conversion strongly. The θ-value of the dithering and the corresponding static light-off are similar and only differ at elevated temperatures.
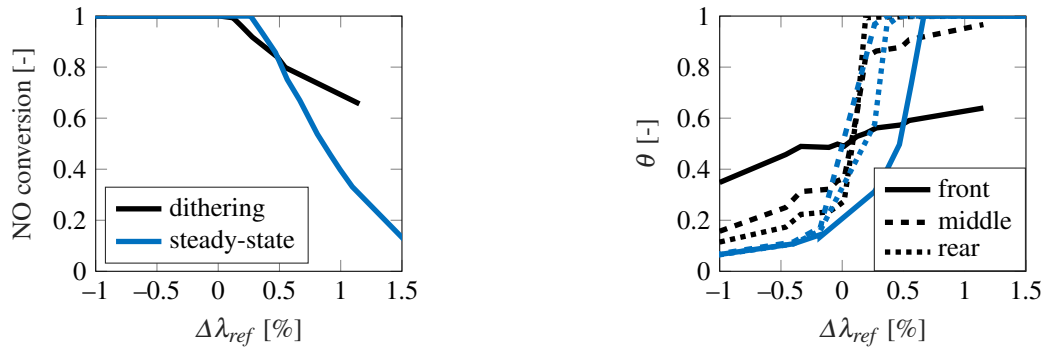
(a) Comparison of the simulated NO conversion with and without λ-oscillations.

(b) Corresponding θ-values.

Figure 4.11: Influence of dithering on the NO conversion window at $460\,\mathrm{kg \cdot h^{-1}}$.

The enhanced conversion window in λ-sweeps is attributed to the additional conversion due to the oxygen storage capacity (OSC) of the catalyst. As long as there are fuel rich phases, the oxygen storage will deplete enough to increase the NO conversion in the lean phases even if the averaged λ-value is slightly lean. Figure 4.11 a depicts the comparison of the simulated NO conversion as a function of the averaged inlet λ-value with and without λ-oscillations, which corresponds to the two λ-sweeps shown in Figure 4.4 f and 4.5 b. Here, the empirical factor ξ has a negligible influence since the catalyst is not limited by inhibition.

The extent of filling of the oxygen storage θ explains the visible differences in Figure 4.11 a. Whereas in the rear part of the filter the characteristics are similar under dithering as well as steady-state conditions, the front part of the filter remains at medium filling level if λ-oscillations are applied (see Figure 4.11 b). Figure 4.12 shows the time-resolved simulation results at a dithered λ of 1.009 ($\Delta\lambda = +0.9\%$). On the left side, one lean pulse with the corresponding spatially averaged θ-value and the NO conversion is depicted. There is a NO breakthrough at the very end of the lean pulse. As can be seen in Figure 4.12 b in the front half of the filter, the oxygen storage is depleted at the beginning of the lean transition because of the fuel rich phase before. The lean inlet feed then fills the oxygen storage from the front until it is full and there is a short NO breakthrough. The following rich pulse depletes the oxygen storage again to the starting point. A constant lean feed would oxidize all the available oxygen storage material and the NO conversion is constantly reduced. Obviously, the short NO breakthrough at dithering conditions is overcompensated by the reduced NO conversion of the non-dithered case. The additional conversion due to the ceria reactions could be one explanation for the higher overall conversion at dithering conditions [184, 195]. Note that the CO conversion will behave similar in a slightly rich regime. However, the difference between dithered and non-dithered operations are smaller since the CO abatement is not stoichiometrically hindered due to the water-gas-shift reaction.
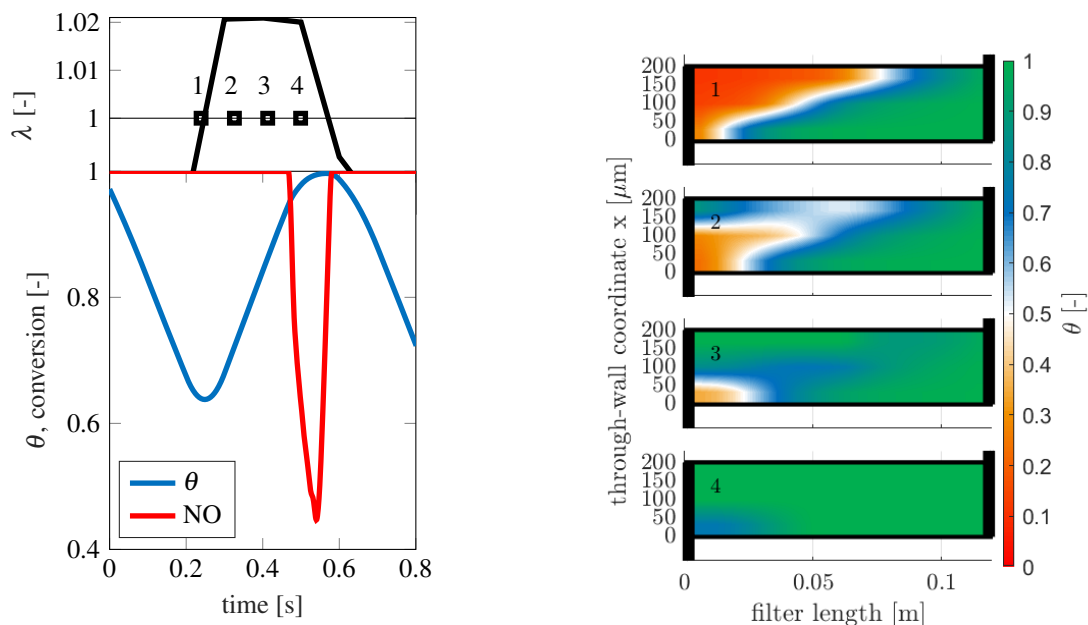
(a) Global spatially averaged θ-values, NO conversion and the corresponding λ-value. The numbered points correspond to the sequenced on the right.

(b) Sequence of spatial θ-distributions during the switch from rich to lean conditions.

Figure 4.12: Time-resolved behavior at dithering condition with a mean λ-value of 1.009 at $460\,\text{kg·h}^{-1}$.

4.4 Conclusion

Especially for the relatively new cGPFs, there are still modeling approaches missing for the highly transient conditions encountered in automotive aftertreatment. Thus, we extended our previously published cGPF channel scale model [95] to simulate catalytic reactions. With the aim to capture all relevant transient phenomena, the applied reaction mechanism includes two different ceria sites and a time dependent oxidation extent of the PGM centers. To determine the kinetic parameters, measurements of the catalytic performance of an in-wall coated cGPF are conducted on a dynamic engine test bench. The determined kinetic parameters achieve a high quality of prediction validated with a WLTP drive cycle, which is not part of the original calibration data.

The modeling results offer likely explanations for the impact of λ-oscillations. The enhanced light-off at dithering conditions can be explained by less competitive adsorption of the emission species when the inlet feed is periodically switched from an oxidizing to a reducing regime. The time- and spatially-resolved extent of ceria site oxidation shows that the enlarged NO conversion window at dithered lean conditions is an oxygen storage phenomenon. Due to fuel-rich phases, the oxygen storage in the front part of the filter is depleted and can absorb a part of the lean pulse even if the average λ-value is on the lean side. Next to a better system design, the model offers the possibility to develop λ-control strategies. Future work will also include a detailed analysis on the impact of the washcoat distribution in cGPFs on the catalytic performance.

4.5 Appendix

The following section lists the applied measurement conditions,the optimization algorithm with the resulting kinetic parameters and additional results of the measurement simulation comparison.

4.5.1 Measurement Conditions and Preprocessing

In order to avoid any impact of soot accumulation, a pre-defined, in situ regeneration procedure, using a lean operation of the combustion engine as well as several fuel cuts, is applied. All gaseous species are measured directly in front of the filter without the use of

a continuous volume sampling (CVS) unit, which would cause low-pass deformations of the signals [186]. Before the measured engine-out signal is applied in the simulations, an additional preprocessing is required. Obviously, a constant time-shift of the gas analyzer's signal to the λ-sensor is necessary in order to correct the residence time of the gas in the sampling lines between the analyzer and the sample. Still, especially under dithering, the time response of the gas analyzers is not fast enough to resolve high-frequency λ-oscillations. Therefore, we determine a correlation between the raw emissions and the UEGO-sensor similar to the work of Zeng et al. [184]. The fundamental assumption is that even if the signal is wrong because of a low-pass filtering in the measurement equipment at one certain point in time, the cumulative value will be correct. Thus, we reconstruct the original dynamics in three steps, which can be seen in Figure 4.13. The data of several steady-state λ-sweeps at different load and speed settings is used to generate a lookup table that connects the measured λ-signal with the corresponding raw emissions of the model species. This table is used in a first step to obtain new raw emissions signal $s_i^{EO,dyn}$. The resulting signals have an identical dynamics as the measured λ-sensor signal. In a second step, the signals are vertically shifted by a value $c_{i,shift}$ until their integral value and the integral of the original measured data $s_i^{EO,meas}$ is identical during a time sequence from t_j to Δt_{corr}:

$$\int_{t_j}^{t_j+\Delta t_{corr}} s_i^{EO,meas} dt = \int_{t_j}^{t_j+\Delta t_{corr}} s_i^{EO,dyn} + c_{i,shift} dt \qquad (4.24)$$

A Δt_{corr} of 3 s is applied for the dithering data. In a third step the O_2-signal is adjusted to exactly match the measured λ-signal via equation (4.25).

$$O_2 = 0.5 \cdot (\lambda \cdot (CO + H_2 + 9HC + 2CO + H_2O) - NO - N_2O - CO_2 - H_2O) \qquad (4.25)$$

In Figure 4.13, the three steps for a part of a steady-state light-off under dithering conditions are applied on a sequence of a light-off at λ 0.99. The different characteristics depict the original measurement data and the corresponding values at the different steps for the determined λ-value by Equation 17, the CO value and the cumulative CO value. Note that all CO data are normalized to the raw measured signal.
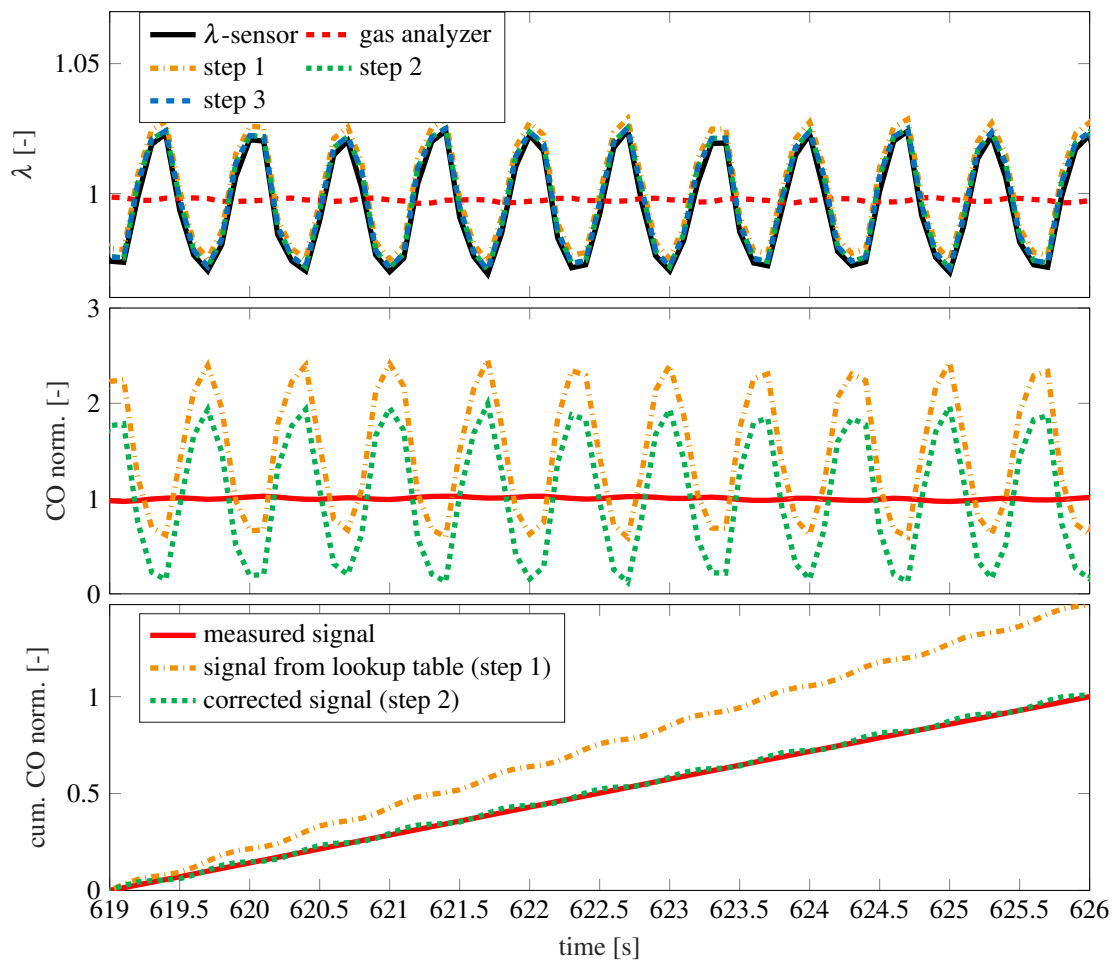
Figure 4.13: Three steps of the inlet data preprocessing applied on a snippet of a light-off at λ $0.99 \pm 2.5\%$ and 1.5 Hz.

4.5.2 Objective Function

In this section we describe the applied objective functions. For the two different types of experiments in the calibration data (steady-state and OSC measurements), two objective functions are necessary.

1) Steady-state objective function

In order to equalize the weighting between different species, it is necessary to scale the fitness values. Therefore, the model prediction of the outlet molar fraction y^{sim} and the measured value y^{meas} are normalized:

$$\tilde{y}_i^{sim} = \frac{|y_i^{sim} - min(y_i^{meas})|}{max(y_i^{meas}) - min(y_i^{meas})} \tag{4.26}$$

$$\tilde{y}_i^{meas} = \frac{|y_i^{meas} - min(y_i^{meas})|}{max(y_i^{meas}) - min(y_i^{meas})} \tag{4.27}$$

The normalized values $\tilde{y}^{sim}$ and $\tilde{y}^{meas}$ are in the interval from 0 to 1 for reacting and close to this interval for product species. We compare the $\tilde{y}$ of the measurement and the model prediction to determine an error e for every species i at the various steady-state points n_{meas}:

$$e_i = \frac{\sqrt{(\tilde{y}_i^{meas} - \tilde{y}_i^{sim})^2}}{\tilde{y}_i^{meas} + 0.01} \tag{4.28}$$

The constant of 0.01 is added to the denominator to avoid drastically increasing error values at diminishing $\tilde{y}_i^{meas}$. Naturally, the best practice is to avoid measurement points with no tailpipe emissions because these points are not significant for the kinetics. The parallel calibration of several species however makes it necessary to include conditions at which a part of the species is fully converted. In order to obtain a single deviation dev_i for every species, the error values are added:

$$dev_i = \frac{1}{n_{meas}} \Sigma^{n_{meas}} e_i \tag{4.29}$$

Depending on the calibration data and the parameter set the deviations dev_i of several species are then added in order to obtain one fitness value with the possibility to add weights to the deviation of a species with a factor.

2) Transient profile (OSC)

Due to the low-pass deformation [186], a direct comparison of the measured outlet data with the simulation is not feasible. Even at a fast sampling, measurement devices imprint a smoothing on the signal that deforms sharp transients into wider but lower peaks as described above. We therefore determine the fitness value with the cumulative emissions. The normalized cumulative outlet emissions (NCOE) are used in order to equalize between the different species:

$$e_i = \frac{1}{t_{end} - t_{start}} \cdot \frac{\sqrt{\int_{t=t_{start}}^{t=t_{end}} (NCOE_i^{sim} - NCOE_i^{meas})^2 dt}}{NCOE_i^{meas}(t_{end})} \tag{4.30}$$

The determined error values e_i are then added, again with the possibility to introduce weights, to form a single fitness value.

Table 4.5 shows the applied calibration scheme. Since a variation of all parameter in parallel is not feasible, the calibration is divided into steps. Hereby, a subset of the measurement data is combined with parameters that are significant for the chosen data. In order to find a global optimum, the sequence is repeated several times.

Table 4.5: Calibration scheme: sequences of the calibration with the goal and applied experiments. The steps 1,2 and 5-7 are repeated after finishing the whole sequence.

	Step	Goal	Parameters	Experiments
Calibration	1	PGM kinetic	$r_1 - r_3, r_7 - r_9$	LO-0.97, LO-0.99, LO-1.004, LO-1.03
	2	Inhibition	G_1, G_2	LO-0.97, LO-0.99, LO-1.004, LO-1.03, LS medium load, LS high load
	3	Steam reforming	r_3, r_6, r_8, G_3	LO-0.97, LS medium load, LS high load
	4	$\Gamma_{fast} + \Gamma_{slow}$	$\Gamma_{fast} + \Gamma_{slow}$	OSC experiment
	5	fOSC	$r_{12} - r_{16}, \Gamma_{fast}$	high-load LS at dithering
	6	WGS, slow OSC	$r_5, r_{17}\text{-}r_{21}$	OSC experiment
	7	K_ξ	$K_{\xi,Ox}, K_{\xi,Red}$	LO-0.99 at dithering conditions
Validation	-	-	-	WLTP cycle

Table 4.6: Kinetic parameters

reaction		$A_{pre}[\frac{m^3}{s \cdot mol}]$	$E_A[-\frac{kJ}{mol}]$
R1	$CO + 0.5O_2 \rightarrow CO_2$	3.028e+21	144
R2	$H_2 + 0.5O_2 \rightarrow H_2O$	1.026e+19	85
R3	$C_3H_6 + 4.5O_2 \rightarrow 3CO_2 + 3H_2O$	5.959e+19	112
R4	$CH_4 + 2O_2 \rightarrow CO_2 + 2H_2O$	4.780e+11	124
R5	$CO + H_2O \rightleftharpoons CO_2 + H_2$	3.737e+12	75
R6	$C_3H_6 + 3H_2O \rightleftharpoons 3CO + 6H_2$	1.887e+14	120
R7	$CO + NO \rightarrow CO_2 + 0.5N_2$	7.914e+14	58
R8	$C_3H_6 + 9NO \rightarrow CO_2 + 0.5\ N_2$	3.590e+11	110
R9	$H_2 + N_2O \rightarrow H_2O + N_2$	3.775e+06	76
R10	$CO + 2NO \rightarrow CO_2 + N_2O$	7.412e+11	37
R11	$CO + N_2O \rightarrow CO_2 + N_2$	2.119e+13	81
R12	$0.5O_2 + fCe_2O_3 \rightarrow 2fCeO_2$	6.278e+10	75
R13	$H_2 + 2fCeO_2 \rightleftharpoons fCe_2O_3 + H_2O$	3.164e+10	80
R14	$CO + 2fCeO_2 \rightleftharpoons fCe_2O_3 + CO_2$	4.214e+14	120
R15	$C_3H_6 + 12fCeO_2 \rightarrow 6fCe_2O_3 + 3CO + 3H_2O$	2.020e+14	125
R16	$NO + Ce_2O_3 \rightarrow 2CeO_2 + 0.5N_2$	2.881e+13	105
R17	$0.5O_2 + Ce_2O_3 \rightarrow 2CeO_2$	7.853e+09	80
R18	$H_2 + 2CeO_2 \rightleftharpoons Ce_2O_3 + H_2O$	5.635e+06	85
R19	$CO + 2CeO_2 \rightleftharpoons Ce_2O_3 + CO_2$	9.580e+08	106
R20	$C_3H_6 + 12CeO_2 \rightarrow 6Ce_2O_3 + 3CO + 3H_2O$	5.396e+07	117
R21	$NO + Ce_2O_3 \rightarrow 2CeO_2 + 0.5N_2$	1.434e+08	80
R ξ_{Ox}	$PGM \rightarrow PGM - O$	4.150e+01	15
R ξ_{Red}	$PGM - O \rightarrow PGM$	2.070e-01	-8

Table 4.7: Inhibition Parameters: $K_i = A \cdot exp(\frac{H_{Ad}}{R \cdot T})$

Parameter	$A[\frac{m^3}{mol}]$	$H_{Ad}[\frac{J}{mol}]$
K_1	1.491e+03	629.41
K_2	1.792e+05	273.29
K_3	6.295e+02	1643.93
K_4	3.608e+02	10.38
K_5	1.490e+05	186.00
$K_{\xi,1}$	4.46e+01	0
$K_{\xi,2}$	4.15e+01	0

Table 4.8: Ceria site density

site	specific surface area $[\frac{m^2}{m^3}]$
Γ_{fast}	57.0
Γ_{slow}	68.0

4.5.3 Applied Kinetic Parameters

The resulting parameter set used for all presented simulations is listed in Table 4.6 and 4.7. The equilibrium constant K_{eq} of the water-gas-shift (WGS) and the steam reforming (SR) reaction are determined by the Gibbs energy. For a faster performance, the temperature dependence of the Gibbs energy is considered via a polynomial fit. The resulting equilibrium constants are determined by:

$$K_{eq,WGS} = exp(-\frac{-4.1034 \cdot 10^4 [\frac{J}{mol}] + 44.19[\frac{J}{mol \cdot K}] \cdot T - 5.553 \cdot 10^{-3}[\frac{J}{mol \cdot K^2}]T^2}{R \cdot T}) \quad (4.31)$$

$$K_{eq,SR} = exp(-\frac{3.826 \cdot 10^5 [\frac{J}{mol}] - 633.8[\frac{J}{mol \cdot K}] \cdot T - 0.02454[\frac{J}{mol \cdot K^2}]T^2}{R \cdot T}) \quad (4.32)$$

Also, for the OSC reactions the chemical equilibrium is considered via the difference in Gibbs energy ΔG

$$K_{eq} = exp(\frac{-\Delta G}{R \cdot T}) \qquad . \quad (4.33)$$

The differences in enthalpy and entropy that determine ΔG are well known for the gaseous species. The values for the oxygen storage materials however are still discussed in the literature. We apply the rounded values from the work of Gong et al. [206] (see Table 4.9). For a possible calibration, these values are handled as parameters in the model. ΔG for the H_2 OSC reaction (R13,R18) is therefore determined as

$$\Delta G_{H2-OSC} = (-241.83 \cdot 10^3 \frac{J}{mol} - \Delta H^0_{CeO}) \cdot 10^3 - T \cdot (58.12 \frac{J}{mol \cdot K} - \Delta S^0_{CeO}) \quad , \quad (4.34)$$

and accordingly for the CO reaction (R14, R19)

$$\Delta G_{CO-OSC} = (-282.99 \cdot 10^3 \frac{J}{mol} - \Delta H^0_{CeO}) \cdot 10^3 - T \cdot (15.73 \frac{J}{mol \cdot K} - \Delta S^0_{CeO}) \quad . \quad (4.35)$$

Table 4.9: Thermodynamic properties of the ceria sites

ceria site	ΔH^0 [kJ/mol]	ΔS^0 [J/mol K]
fast	-250	-0.6
slow	-250	-0.6

4.5.4 Impact of Dithering

In order to present the impact of dithering solely on the measurement results more clearly, Figure 4.14 depicts a light-off as well as λ-sweeps with and without λ-oscillations.
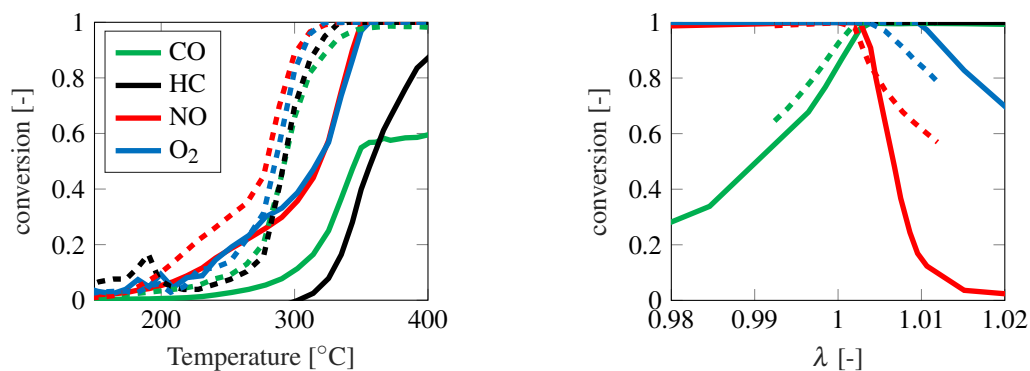
(a) Quasi-steady light-Off at mean λ:0.99.

(b) λ-sweep from rich to lean.

Figure 4.14: Impact of dithering on measured quasi-steady light-off at 115 kg/h and λ-sweep at 260 kg/h. Solid lines represent measurement results without λ-oscillations, dashed lines depict measurements at a λ-amplitude of 2.5% at a 1.5 Hz frequency.

4.5.5 Steady-State H$_2$ and N$_2$O Values

Additional to the conversions depicted in the results section, the normalized outlet emissions (NOE) of H$_2$ and N$_2$O for all steady-state operating points are shown in Figure 4.15. The model prediction and the measurement are normalized to the maximum measured outlet value of all measurements, which is in the slightly lean light-off for N$_2$O and on the rich side of high load λ-sweep for H$_2$. This normalization allows to differentiate between a high and a low discrepancy. It can be seen that the general trends are captured. However, the quality is not as good as for the major components.
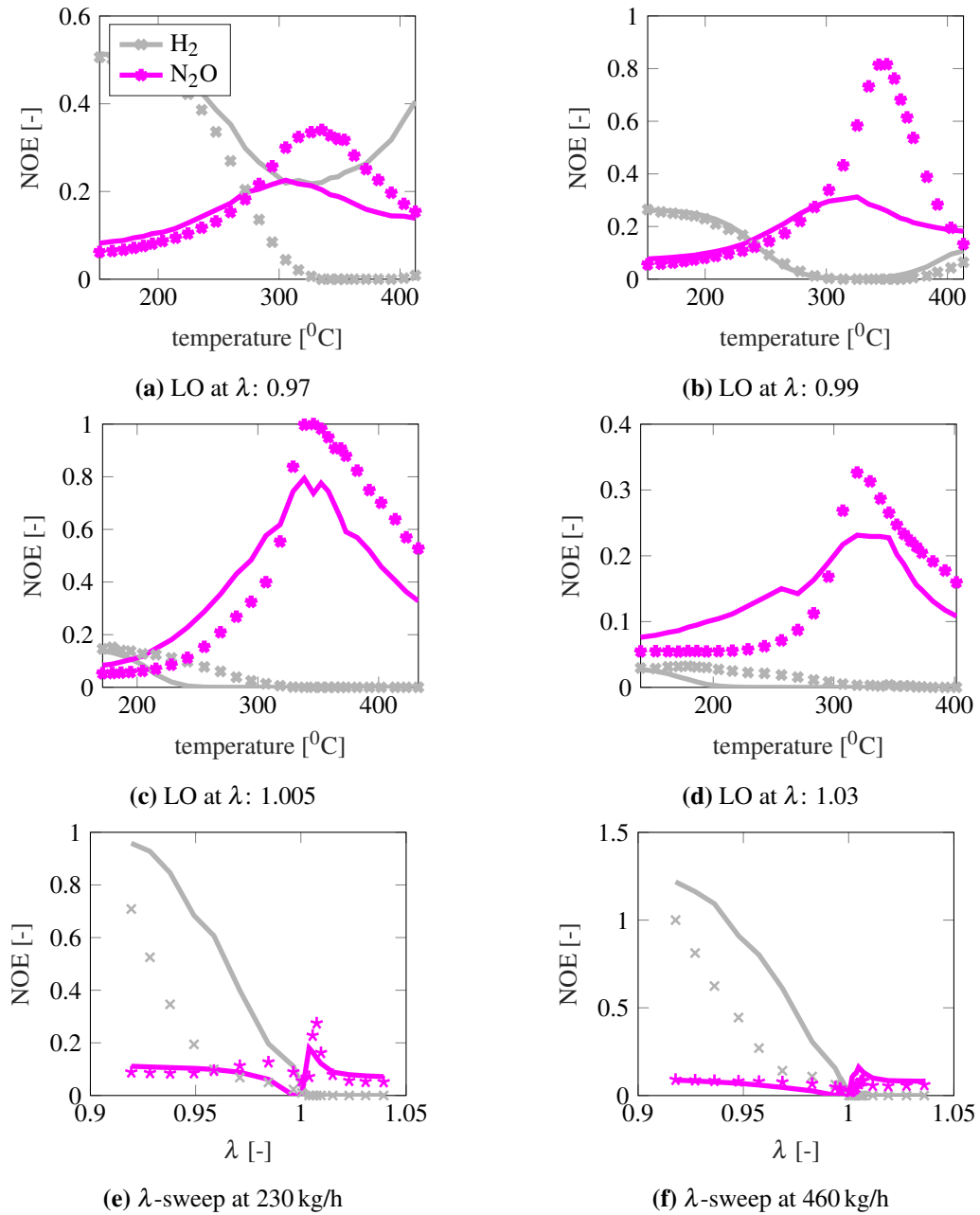
Figure 4.15: N_2O and H_2 model fit: quasi-steady-state light-off at 115 kg/h for different λ-values and λ-scans at 260 kg/h and 460 kg/h. Measurement results are depicted as symbols and simulation results represent the lines.

5 A Model-Based Analysis of Washcoat Distribution on Zoned Coated Gasoline Particulate Filters

Summary of the publication

The integration of three-way catalysts (TWC) and gasoline particulate filters into a single so-called coated GPF (cGPF) can decrease the necessary packaging volume and costs in exhaust gas aftertreatment systems. Similar to classical TWCs, it is possible to introduce advanced coating technologies, in the presented case zoning, which creates zones of high and low washcoat loading, resulting in a filter with an axial non-uniformity of the washcoat distribution. In addition to zoning, a filter can either be coated solely in-wall or have a partially or fully on-wall coating, which leads to a variety of coating configurations. To investigate the impact of the coating configuration, a previously published validated cGPF model is applied to evaluate the pressure drop, high load conversion, and light-off performance of fresh cGPFs. The simulations reveal an enhanced light-off at steady-state conditions if more washcoat is deposited at the front part of the filter or on the inlet channel. Under transient conditions, however, a filter with a catalytic layer on the outlet channel performs best.

Individual Contributions of the Candidate

The methodology as well as the implementation and software were carried out by the
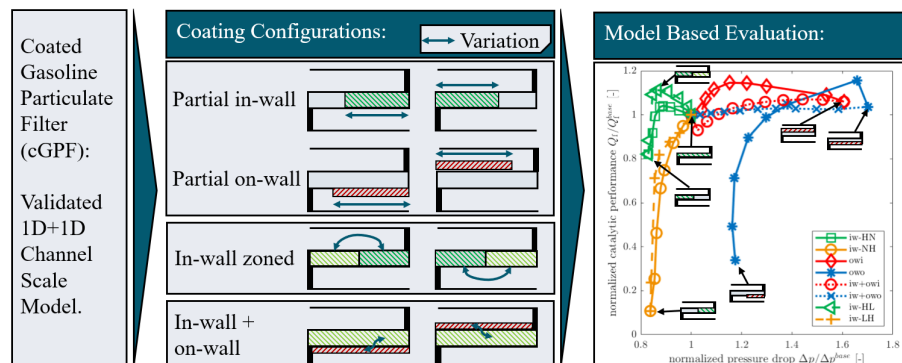
105

candidate. Jens Neumanns supervised the modeling process. Prof. Olaf Hinrichsen helped reviewing and editing the manuscript which was written by the candidate.

5.1 Introduction

Nowadays, particulate filters are a standard component in the exhaust gas aftertreatment systems of diesel as well as gasoline vehicles. For the latter, gasoline particulate filters (GPF) are a relatively new technology [68, 80] to cope with the increasingly stringent legislation regarding the particle number emissions [67, 70]. The GPF is a wall-flow device consisting of square channels plugged at alternate ends in adjacent channels such that the exhaust gas mixture passes through the walls of a porous substrate [79, 80, 85]. The filtration which is strongly dependent on the microstructure of the porous media mainly proceeds via the particle diffusion mechanism due to the small size of the nanoparticles emitted by modern gasoline engines [80, 85].

In addition to the GPF, the exhaust gas aftertreatment system of a gasoline engine contains three-way catalysts (TWC) in order to reduce the emissions of CO, NO, and unburned hydrocarbons (HC). The integration of three-way catalysts (TWC) and GPF into a single so-called coated gasoline particulate filter (cGPF) offers different benefits. The combination of two devices reduces the necessary packaging volume for the exhaust aftertreatment system, which helps to increase the total catalytic active volume to that necessary to meet legislation for real driving emissions (RDE) [31, 217]. Additionally, it offers the opportunity to place the GPF closer to the engine, thus enabling more effective regenerations of the filter without introducing a catalytic inactive heat sink into the system [74, 218, 219].

GPFs are usually coated with three-way catalysts made of Pd/Rh on an alumina/ceria support [41, 90, 160], whereas DPFs are mostly coated with a Cu/zeolite washcoat for NOx reduction or Pt/alumina as oxidation catalyst [220–222]. Depending on the properties of the catalyst slurry and the washcoating method, the catalyst is either deposited in the wall or on the walls of either inlet or outlet channel [96, 97]. A mix of both, in-wall and on-wall, is also possible depending on the washcoat loading. Punke et al. [223] suggested that zoning, i.e. the introduction of zones with different catalytic loadings, could be beneficial during a cold start. With zoning, a new degree of freedom can be introduced to optimize the filter with respect to the catalytic conversion, filtration, and backpressure as well as cost-effectiveness. The resulting complexity in coating options makes modeling approaches that can evaluate the effectiveness of the different coating possibilities necessary.

Simulation studies on channel scale compared the conversion performance of in-wall coated filters with conventional open monoliths [169, 170, 201]. For DPFs with an integrated coated diesel oxidation catalyst, Dardiotis et al. [220] evaluated the influence of zoning. The authors found that it is beneficial to place more catalytic coating in the front part of the filter for a faster light-off. However, Dardiotis et al. [220] did not consider the influence of zoning on thermal mass or on wall flow distribution. Karamitros et al. [222] included the impact of the different wall-flow behavior as they compared a uniform coated DPF with two zoned ones.

On a much finer pore scale, Kočí et al. [110] introduced the application of 3D-CFD calculations based on X-Ray microtomography (XRM) data. Leskovjan et al. [162] determined the permeability of different filters including partially on-wall coated filters using XRM data and Plachá et al. [87] calculated the particle capture in the pore scale regime with this data. Also, simple first-order reactions were already implemented in this framework [163]. Belot et al. [103] applied pore scale simulations on virtually created differently coated filter walls and validated their modeling with additive manufacturing [224]. In the study, the authors compared on a pore scale uniform in-wall coating with a non-uniform coating at increasing washcoat amounts. Other work focused on the application process of three-way catalysts on filters. Blažek et al. [97] applied time-resolved XRM to bring new insights into the drying dynamics of the washcoat in and on the porous filter wall. In their subsequent pressure loss experiments, the authors compared different coatings. A dense on-wall layer showed the highest pressure loss, whereas a macro-porous on-wall layer was comparable to a solely in-wall coated filter [97].

Since pore scale models capture only a tiny part of one wall in a single channel of the filter, it is challenging to evaluate a whole filter with these models. Studies applying channel scale models that are coarser but make an evaluation of a filter concept possible are rare and previously focused only on DPF coatings such as SCR or DOC. In addition, the possibility of an on-wall coating is not considered at all in these works [170, 220, 222]. Thus, there is still no study that clearly differentiates the impact of on-wall and in-wall coating in combination with zoning. In order to close this gap, we apply our channel scale model [95], which was recently extended by a global reaction kinetics [168] for TWC coatings, on different filter configurations and compare the catalytic performance under relevant operating conditions. The applied kinetics and the cGPF model were validated within a broad range of steady-state measurements as well as transient drive cycles on an in-wall coated filter [168]. This in-wall filter is therefore regarded as a base configuration for the variations of washcoat distribution presented here.

5.2 Methodology

A methodology was developed to virtually construct filters with axially gradients or zones of washcoat distributions but the same overall catalyst mass. In a second step, a porous media model determines the spatial porosity and permeability to capture the influence on flow distribution and on thermal behavior. By applying our previously published reaction kinetics, a direct comparison of the different configurations under realistic operating conditions is possible. Naturally, a reference filter with defined properties is necessary. The applied configuration shown in Table 5.1 is identical to an in-wall coated, cordierite filter that was extensively studied in a previous work of ours [168]. For this *base* filter, the difference between the model prediction and the measured values are 10 K in average for the $T50$-value of the main pollutants CO, HC and NO at steady-state light-offs at four different λ-values. Under rich conditions, the difference for the NO $T50$-value decreases to 3 K [168]. In the transient validation, the emission levels of a WLTC are estimated within a 5% error range.

Table 5.1: Substrate properties valid for all considered configurations.

diameter [mm]	136
length, L [mm]	120
cell density [cpsi]	300
wall thickness, th [mil]	8
porosity, $\varepsilon_{\text{cord}}$ (prior to coating) [-]	0.64
porosity, ε_{base} [-]	0.47
tortuousity, τ [-]	3.5
porosity of the optional on-wall layer, ε_{ow} [-]	0.1
ϕ_{wsc}^{base} [-]	0.17
washcoat loading [g/l]	75
PGM ratio Pt:Pd:Rh [-]	0:7:2
heat capacity of cordierite, c_{cord} [J/kgK] (see [126])	$\dfrac{-3.44 \cdot 10^7 [\frac{\text{K} \cdot \text{J}}{\text{kg}}]}{T^2} + 1071[\frac{\text{J}}{\text{kg} \cdot \text{K}}] + 0.156[\frac{\text{J}}{\text{kg} \cdot \text{K}^2}] \cdot T$
heat capacity of the washcoat (γ-Al$_2$O$_3$), c_{wsc} [J·Kg^{-1}K^{-1}] (see [225])	$\dfrac{1\,[\text{kg}]}{101.96\,[\text{mol}]} \cdot (102.42[\frac{\text{J}}{\text{molK}}] + 38.75 \cdot 10^{-3}[\frac{\text{J}}{\text{kg} \cdot \text{K}^2}] \cdot T - 1.591 \cdot 10^{-3}[\frac{\text{J}}{\text{kg} \cdot \text{K}^3}] \cdot T^2 + 2.63\,10^{-3}[\frac{\text{J}}{\text{kg} \cdot \text{K}^4}] \cdot T^3 - 3 \cdot 10^{-3}[\frac{\text{JK}}{\text{kg}}] \cdot T^{-2}$
washcoat density, ρ_{wsc} [kg/m^3]	1710
cordierite density (see [225]), ρ_{cord} [kg/m^3]	2050
thermal conductivity (see [126]), λ [W·m^{1-}·K^{-1}]	1.5

5.2.1 Considered Configurations

To describe possible coating configurations of cGPFs, three parameters are introduced: the fraction of washcoat deposited on-wall ζ, the partial coating factor ξ, and the zoning intensity of the coated low zone χ. Equation (5.1) to Equation (5.3) describe these parameters with the help of the total washcoat mass of the filter m_{wsc}.

$$\zeta = \frac{m_{\text{wsc,ow}}}{m_{wsc,ow} + m_{\text{wsc,iw}}} \tag{5.1}$$

$$\xi = \frac{L_{\text{coated}}}{L_{\text{chan}}} \tag{5.2}$$

$$\chi = \frac{m_{\text{wsc,low}}}{m_{\text{wsc,high}} + m_{\text{wsc,low}}} \tag{5.3}$$

Figure 5.1 shows the resulting topologies. Note that the corresponding pairs on the left and right sides of Figure 5.1 are mirrored. In each case two of the numbers are kept constant and one is varied. Table 5.2 illustrates the value range for the different configurations considered in this work. The coating gap of the on-wall coated filters (owi, owo) is chosen in a way that the exhaust flow is forced to flow either through or along a catalytic active zone. A screening study conducted beforehand revealed that configurations, which allow the exhaust gas flow to bypass the catalytic layer e.g., an owi configuration with a gap at the front, exhibit a low catalytic performance and only minor benefits regarding the pressure loss.

Table 5.2: Considered filter configurations and their description.

Topologies	figure	on-wall fraction ζ	partial coating factor ξ	fraction zoned low χ
iw-HN, iw-NH	5.1a, 5.1b	0	[0.5 ... 1]	0
iw-HL, iw-LH	5.1c, 5.1d	0	0.5	[0 to 0.5]
owi, owo	5.1e, 5.1f	1	[0.5 to 1]	0
iw+owi, iw+owo	5.1g, 5.1h	[0 to 1]	1	1

Since the washcoat volume and the washcoat mass are constant in each case, the porosity and on-wall layer thickness varies, see Section 5.2.3. The resulting values at different

(a) In-wall high-no (iw-HN)

(b) In-wall no-high (iw-NH)

(c) In-wall high-low (iw-HL)

(d) In-wall low-high (iw-LH)

(e) On-wall inlet channel (owi)

(f) On-wall outlet channel (owo)
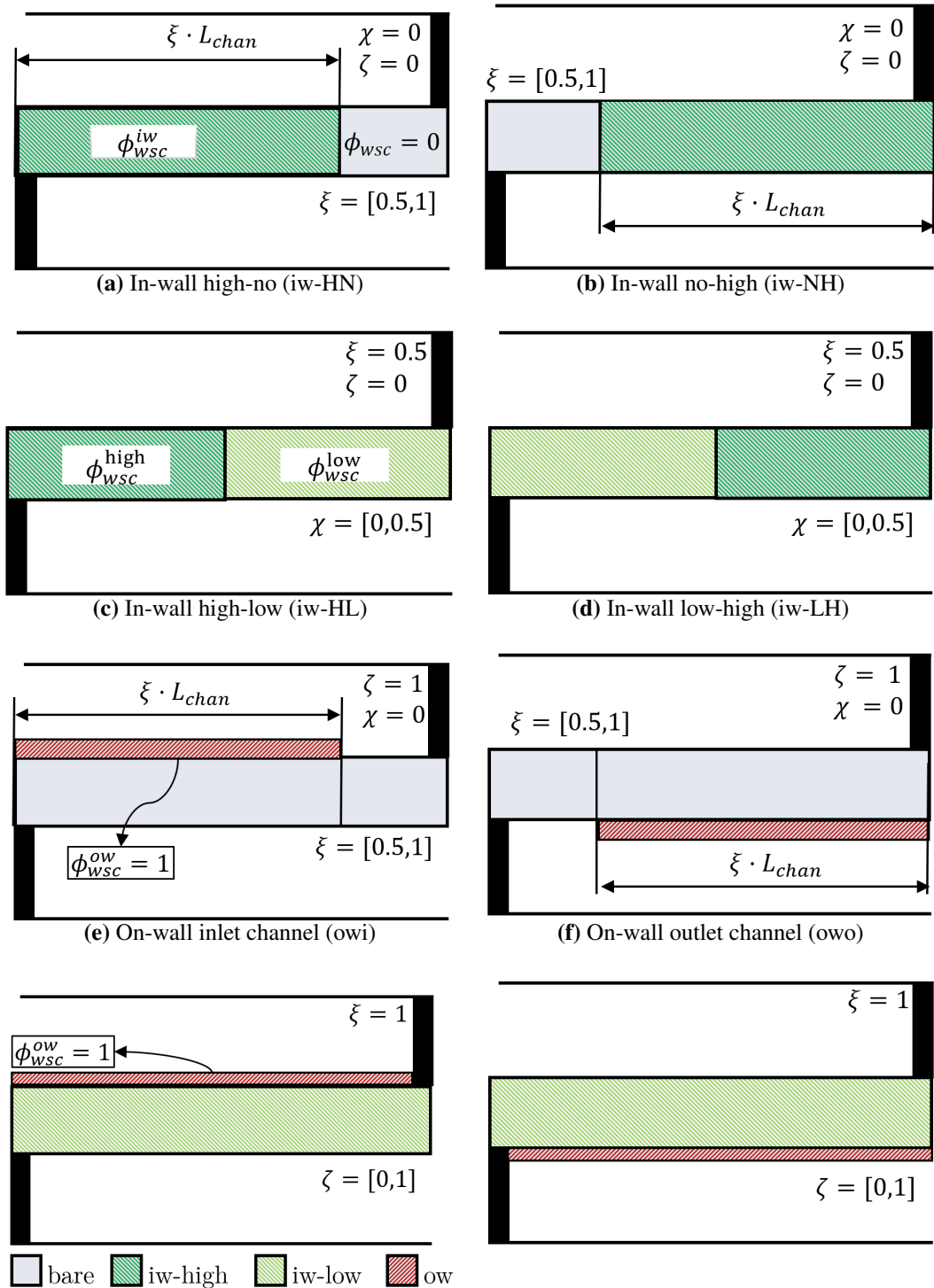
(g) In-wall and on-wall inlet channel (iw+owi)

(h) In-wall and on-wall outlet channel (iw+owo)

Figure 5.1: cGPF configurations. Green and red coloring indicates catalytic active porous media whereas grey indicates inert material. Flow direction is from top left to bottom right. The variation range of the parameters for every case is given in the square brackets.

partial coating factors ξ can be found in Figure 5.13 in the appendix. The configurations iw-HL and iw-LH (Figure 5.1c,5.1d) describe a zoning of the washcoat in two in-wall zones of equal length with either high loading at the front and lower loading at the rear or vice versa. Additionally, two configurations with both on-wall and in-wall coating (iw-owi, iw-owo) are considered (Figure 5.1g,5.1h). Here, the splitting ratio of the washcoat between on-wall and in-wall is varied, which leads to a spread between a uniformly in-wall coated filter at $\zeta = 0$ and a solely on-wall coated filter at $\zeta = 1$.

5.2.2 Reactor Model
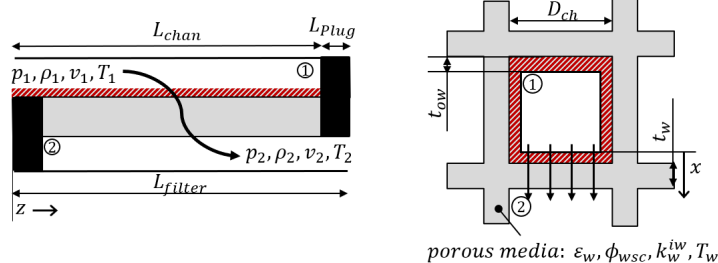
Figure 5.2: Model description.

The transient reactor model of this work was previously published in [168]. The model solves the governing equations for the conservation of energy, species, and momentum for one representative pair of an inlet and an outlet channel and the separating porous wall as can be seen in Figure 5.2. In the channels, one-dimensional profiles of the velocity, temperature, and species concentration are computed. Corresponding transfer coefficients [153, 226] describe radial transfer effects. Applying a 1D+1D approach [133, 169, 170], the porous medium is discretized in axial and trough-wall direction. Here, radial as well as axial heat and mass transfer are considered. An additional on-wall layer can be applied either on the inlet or on the outlet channel. The interested reader can find a detailed description of the modeling approach in 5.5.2. The resulting reaction rates $\dot{r}_i$ are scaled by the local washcoat fraction ϕ_{wsc} (see Equation (5.4)) similar to the work of Karamitros et al. [222] as well as Greiner et al. [163] to capture with the influence of non-uniform coating on the reaction rates.

$$\dot{r}_i = \phi_{\text{wsc}} \cdot \dot{r}_{i,\text{wsc}} \tag{5.4}$$

To ensure sufficient accuracy, a grid convergence study of the axial discretization is conducted for two representative filter configurations. The results can be seen in 5.5.3.

5.2.3 Porous Media Model

A rigorous porous media model is applied to correctly capture the differences in thermal and wall-flow behavior. To cope with an additional catalytic on-wall layer or the heterogeneous properties of the porous media, every finite element can be attributed with a permeability k_w, porosity ε, and washcoat fraction ϕ_{wsc}. The influence of the trapezoidal cross section of an on-wall layer on one wall on pressure drop is considered by Equation (5.5), which is derived from an integration of Darcy's law [78].

$$k_{w,ow}^* = 2k_{ow} \cdot (log(\frac{D_{chan}}{D_{chan} - 2t_{ow}}))^{-1} \tag{5.5}$$

The channel wall volume is characterized by its porosity ε and its washcoat volume fraction ϕ_{wsc}. Together with the fraction of cordierite ϕ_{cord} these numbers close the volume balance. As a consequence, a local increase in the washcoat fraction will decrease the porosity. The resulting density $\bar{\rho}$ and the corresponding heat capacity of the porous media $\bar{c}$ is then determined by

$$\bar{\rho}\bar{c} = \varepsilon \cdot \rho_{gas} \cdot c_{gas,p} + \phi_{wsc} \cdot \rho_{wsc} \cdot c_{wsc} + \phi_{cord} \cdot \rho_{cord} \cdot c_{cord} \tag{5.6}$$

with the densities ρ, heat capacities c from Table 5.1 and fluid heat capacity $c_{gas,p}$ from correlations of the VDI Heat Atlas [155]. The properties of the exhaust gas mixture are determined via correlations for the single species and appropriate averaging methods [155]. With a set spatial ϕ_{wsc} and the porosity of the bare substrate ε_{cord}, the resulting porosity is calculated via Equation (5.7).

$$\varepsilon = 1 - ((1 - \varepsilon_{cord}) + \phi_{wsc}) \tag{5.7}$$

Further, in analogy to soot loading models [78, 122], we apply a porosity-dependent permeability for the filter wall in order to capture the influence of different washcoat fractions on the flowfield in the channels. The permeability determines the wall-flow and greatly impacts the overall pressure drop. With the permeability k_w^{base} of the reference filter, the permeability at a different porosity is expressed as

$$k_w = k_w^{base} \cdot \frac{f(\varepsilon)}{f(\varepsilon^{base})} \qquad . \tag{5.8}$$
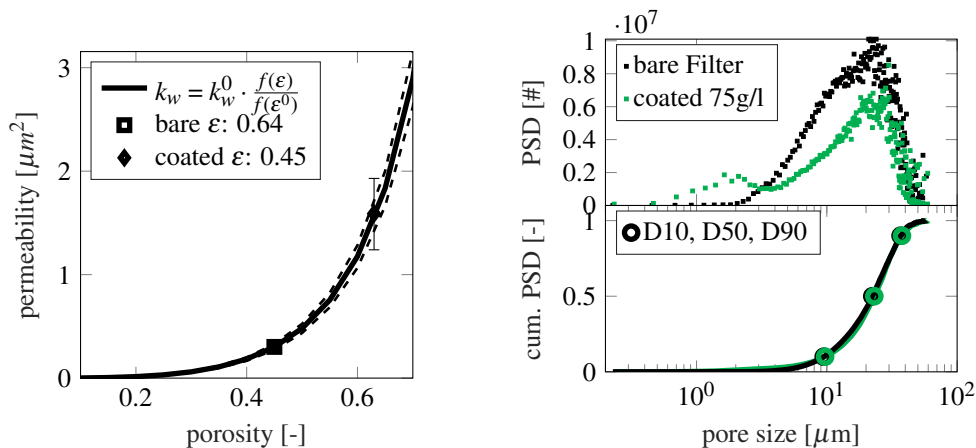
(a) Dependency of the permeability on the porosity of the porous media with two a priori determined permeabilities and their corresponding 95% confidence intervals.

(b) Measured pore size distribution of a bare and a coated GPF.

Figure 5.3: Impact of coating permeability and pore size distribution.

Hereby, $f(\varepsilon)$ is Kuwabara's formula [111]: $f(\varepsilon) = (1-\varepsilon)^{-1} \cdot (1 - \frac{9}{5}(1-\varepsilon)^{\frac{1}{3}} + (1-\varepsilon) - \frac{1}{5}(1-\varepsilon)^2)$. To apply Equation (5.8) it is necessary to know the permeability and porosity of one *base* filter. Therefore, we determine the permeability of an in-wall coated filter and a corresponding bare substrate utilizing pressure drop experiments [95]. As *base* case we apply the permeability of the coated filter because especially, in that case, the wall flow is the dominant contributor to the overall pressure drop. In contrast, the impact of the permeability on the pressure drop of the bare substrate is less as can be seen from the wide confidence intervals shown in Figure 5.3a , which illustrates the permeability at different porosities with the determined permeabilities of the two filters as markers. The dashed lines show the correlation with the upper and lower 95% confidence interval of the *base* filter's permeability. It has to be pointed out that the confidence interval of the coated filter is so small that it is not distinguishable from the marker. As can be seen in Figure 5.3a, the correlation correctly estimates the permeability of the bare filter.

The description of the permeability with the porosity is based on the assumption that the relative pore size distribution of the porous media only slightly changes with coating. To further validate this hypothesis, X-ray microtomography (XRM) scans of the two filters were conducted. Figure 5.3b displays the number of pores determined by the maximum sphere inscription method [167]. Whereas the total number of pores decreases, the cumulative pore size distribution and especially the mean pore size (D50) shift only slightly.

The permeability of the on-wall layer is more complex to determine since it depends mostly on cracks and the macro porosity of the layer [110, 162], which is not in the scope of this work. Therefore, we assume a constant on-wall permeability k_{ow} of $0.035\,\mu\mathrm{m}^2$, which is similar to the permeabilities determined by Leskovjan et al. [162] for densely on-wall coated filters.

Table 5.3 lists the formulas applied to determine the local washcoat loading ϕ_{wsc}, on-wall layer thickness t_{ow}, and permeability k_{w} for the different concepts. Assuming a constant total washcoat mass and washcoat density, ϕ_{wsc} is calculated by multiplying the washcoat fraction of the *base* case $\phi_{\mathrm{wsc}}^{base}$ with the appropriate parameters for the case-specific washcoat distribution. For on-wall concepts, the thickness of the catalytic layer corresponding to the washcoat volume of the *base* case is of interest. For more readability, t_{ow} is calculated by applying the area of the on-wall layer $A_{\mathrm{wsc}}^{\mathrm{ow}}$. A constant porosity $\varepsilon_{\mathrm{ow}}$ of 0.1 is assumed for all on-wall layers.

Table 5.3: Calculation of the washcoat fraction ϕ_{wsc} and permeability k_{w} for the different filter configuration. The corresponding local porosity ε can be determined by Equation (5.7) ($\varepsilon = 1 - ((1 - \varepsilon_{\mathrm{cord}}) + \phi_{\mathrm{wsc}})$) from ϕ_{wsc}. For all uncoated parts of a filter, the properties of the bare substrate ($\varepsilon_{\mathrm{cord}}$) are applied (see Table 5.1).

configuration	ϕ_{wsc}	k_{w}
iw-HN / iw-NH	$\phi_{\mathrm{wsc}}^{\mathrm{iw}} = \frac{1}{\xi} \cdot \phi_{\mathrm{wsc}}^{base}$	$k_{\mathrm{w}}^{\mathrm{iw}} = k_{\mathrm{w}}^{base} \cdot \frac{f(\varepsilon^{\mathrm{iw}})}{f(\varepsilon^{base})}$
iw-HL / iw-LH	$\phi_{\mathrm{wsc}}^{\mathrm{iw-high}} = (\xi^{-1} - \xi^{-1} \cdot \chi)\,\phi_{\mathrm{wsc}}^{base}$ $\phi_{\mathrm{wsc}}^{\mathrm{iw-Low}} = (\xi^{-1} - \xi^{-1} \cdot (1-\chi))\,\phi_{\mathrm{wsc}}^{base}$	$k_{\mathrm{w}}^{\mathrm{iw-high}} = k_{\mathrm{w}}^{base} \cdot \frac{f(\varepsilon^{\mathrm{iw-high}})}{f(\varepsilon^{base})}$ $k_{\mathrm{w}}^{\mathrm{iw-low}} = k_{\mathrm{w}}^{base} \cdot \frac{f(\varepsilon^{\mathrm{iw-low}})}{f(\varepsilon^{base})}$
owi / owo	$A_{\mathrm{wsc}}^{\mathrm{ow}} = \frac{2(\frac{D_{\mathrm{filter}}^2}{4\pi} - D_{\mathrm{chan}}^2) \cdot \phi_{\mathrm{wsc}}^{base}}{\xi \cdot (1 - \varepsilon_{\mathrm{ow}})}$ $t_{\mathrm{ow}} = 0.5 \cdot (D_{\mathrm{chan}} - \sqrt{D_{\mathrm{chan}}^2 - A_{\mathrm{wsc}}^{\mathrm{ow}}})$ $\phi_{\mathrm{wsc}}^{\mathrm{ow}} = 1 - \varepsilon_{\mathrm{ow}}$	$k_{\mathrm{w}}^{\mathrm{ow}} = 0.035\,\mu m^2$ $k_{\mathrm{w}}^{\mathrm{iw}} = k_{\mathrm{w}}^{base} \cdot \frac{f(\varepsilon^{\mathrm{bare}})}{f(\varepsilon^{base})}$
iw+owi / iw+owo	$A_{\mathrm{wsc}}^{\mathrm{ow}} = 2\zeta \cdot (\frac{D_{\mathrm{filter}}^2}{4\pi} - D_{\mathrm{chan}}^2) \cdot \frac{\phi_{\mathrm{wsc}}^{base}}{1 - \varepsilon_{\mathrm{ow}}}$ $t_{\mathrm{ow}} = 0.5 \cdot (D_{\mathrm{chan}} - \sqrt{D_{\mathrm{chan}}^2 - A_{\mathrm{wsc}}^{\mathrm{ow}}})$ $\phi_{\mathrm{wsc}}^{\mathrm{ow}} = 1 - \varepsilon_{\mathrm{ow}}$ $\phi_{\mathrm{wsc}}^{\mathrm{iw}} = \phi_{\mathrm{wsc}}^{base} \cdot (1 - \zeta)$	$k_{\mathrm{w}}^{\mathrm{ow}} = 0.035\,\mu m^2$ $k_{\mathrm{w}}^{\mathrm{iw}} = k_{\mathrm{w}}^{base} \cdot \frac{f(\varepsilon^{\mathrm{iw}})}{f(\varepsilon^{base})}$

5.3 Results and Discussion

Next to filtration performance, pressure drop and catalytic performance are the key criteria of a cGPF. Thus, we apply virtual experiments to first evaluate the impact of the coatings

on the pressure drop. In a second step, the catalytic conversion at high space velocities is analyzed. In the last step, two different light-off scenarios, a quasi-steady-state case with an inlet temperature ramp of $1\,\mathrm{K\cdot s^{-1}}$ and a transient light-off at a heating rate of $30\,\mathrm{K\cdot s^{-1}}$, highlight the impact of zoning.

Table 5.4: Inlet conditions for the different experiments.

experiment	λ [-]	mass flow [$\mathrm{kg\cdot h^{-1}}$]	temperature [°C]
pressure drop	0.999	450	800
quasi steady light-off	0.999	110	100 to 400 at $1\,\mathrm{K\cdot s^{-1}}$
transient light-off	0.999	110	20 to 700 at $30\,\mathrm{K\cdot s^{-1}}$
high-load variation	0.999	100 to 1700	600

Table 5.4 lists the inlet conditions for the different experiments. In all cases, the feed gas is a mixture with the slightly rich λ-value of 0.999. The applied composition, shown in Table 5.5, corresponds roughly to a medium-load engine out of a direct injection gasoline engine [126].

Table 5.5: Inlet feed applied in all experiments. The mixture has a λ-value of 0.999

species	fraction [-]
CO [ppm]	2400
CO_2 [%]	12.8
HC [ppm]	315
CH_4 [ppm]	32
H_2 [ppm]	1120
NO [ppm]	2230
O_2 [ppm]	1860
H_2O [%]	12.9
N_2 [%]	73.3

5.3.1 Pressure Drop

Figure 5.4a depicts pressure drop as a function of mass flow for the four axially zoned configurations at the minimum ($\xi = 0.5$) and maximum ($\xi = 1$) considered partial coating factor. As the compressible flow is defined by a pressure boundary at the outlet and a mass flow at the inlet, it can be observed that the inlet density is influenced by the pressure drop. This results in a slightly decreasing slope for the fully coated on-wall filters that have the highest backpressure.
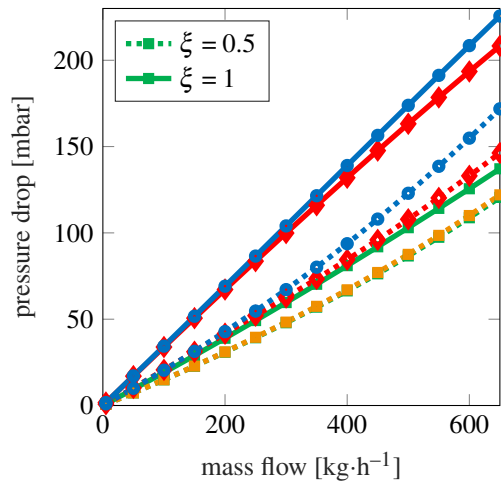
(a) Pressure drop for different configurations.
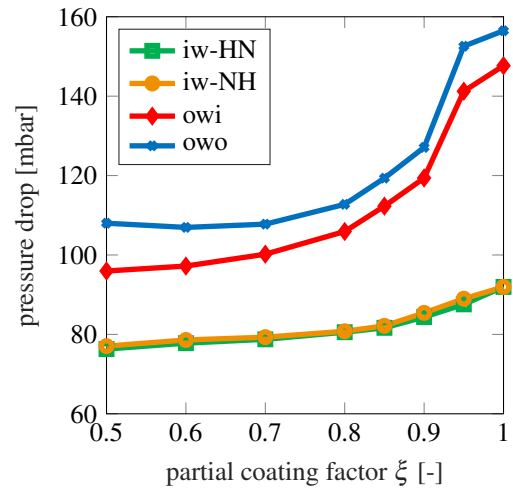
(b) Pressure drop for different partial coating factors ξ at $450 \, \mathrm{kg \cdot h^{-1}}$ and $800\,^{\circ}\mathrm{C}$.
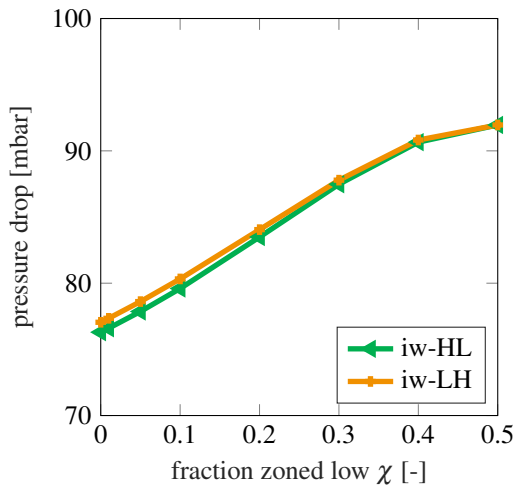
(c) Pressure drop for different washcoat distribution χ at a constant partial coating factor $\xi = 0.5$ at $450 \, \mathrm{kg \cdot h^{-1}}$ and $800\,^{\circ}\mathrm{C}$.
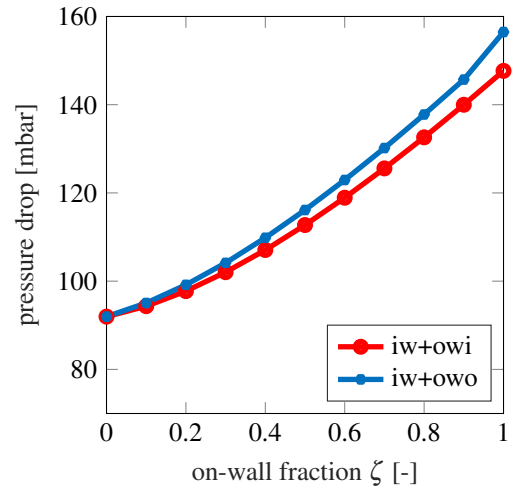
(d) Pressure drop at varying on-wall fractions ζ for fully coated filter ($\xi = 1$) at $450 \, \mathrm{kg \cdot h^{-1}}$ and $800\,^{\circ}\mathrm{C}$.

Figure 5.4: Pressure drop for different coating parameters.

Since pressure drop is relevant at high load conditions, Figures 5.4b to d depict pressure drop at $450\,\mathrm{kg\cdot h^{-1}}$ and $800\,^\circ\mathrm{C}$ for different coating parameters. As can be seen, on-wall coating leads to an increased pressure drop. With decreasing partial coating factors ξ, the resulting coating gap, however, can greatly reduce the pressure drop. The impact of a partial coating on the purely in-wall coated configuration is smaller since the differences in permeability are not as high as for the on-wall coated configurations. Because the result is dependent on the on-wall permeability, which is kept constant, the impact of this value is evaluated in Figure 5.15 in the appendix. If the flow resistance in the catalytic on-wall layer is higher than that of the filter walls, a coating gap will decrease the pressure drop. The variations of the χ- and ζ-values reveal that the pressure drop gradually changes from the corresponding extreme cases, e.g., from an in-wall coating ($\zeta = 0$) to a purely on-wall coated filter ($\zeta = 1$), of Figure 5.4d.

Furthermore, comparing the owi with the owo cases, it is beneficial to place the zones with higher permeability at the rear of the filter (Figure 5.4a). Due to the axial distribution of the wall velocity, there is an increase in wall-flow at the rear. Therefore, the mass flow through a coating gap at the rear is higher than through a coating gap with the same size at the front of the filter. The axial wall-flow distribution depends on the pressure difference between the inlet and the outlet channel. Whereas the pressure loss in the outlet channel increases with the channel length due to the rising channel velocity, the inlet channel pressure only slightly decreases due to the decreasing velocity [145, 154, 171]. Figure 5.16 in the appendix shows the channel pressure profiles and the resulting wall velocities for different partial coating factors ξ. The different pressure profiles result in a larger difference in the rear part of the filter and therefore more wall-flow at this point. Therefore, the owi and the iw-HN configuration with the coating gap at the rear have a lower pressure drop than their mirrored counterparts owo and iw-NH.

5.3.2 High-Load Conversion

As a first comparison of catalytic behavior, a steady-state variation of the mass flow is conducted. Since the catalysts are usually warm under operating conditions at high load, e.g., highway driving, a constant inlet temperature of $600\,^\circ\mathrm{C}$ is chosen for this virtual experiment. At this temperature, the reaction rate does not limit the conversion when applying the characteristics of a fresh catalyst. Rather, the mass transfer in the channel and the walls decreases the observed conversion. Under industrially relevant conditions, an aged cGPF would be applied for this experiment to capture kinetic as well as mass transfer limitation. However, we expect the configurations to show different aging characteristics

due to differences in the thermal behavior and contact with deactivating substances e.g., oil [227]. Applying an appropriate deactivation is out of the scope of this work. Still, differences in the mass transfer limitation allow to elucidate the impact of zoning.

(a) NO conversion over GHSV at a partial coating factor $\xi = 0.8$.

(b) NO conversion for the different configurations at a $GHSV = 8 \cdot 10^5 \text{h}^{-1}$.

(c) NO conversion for different coating ratio at a ξ-value of 0.5 and a $GHSV = 8 \cdot 10^5 \text{h}^{-1}$.

(d) NO conversion at different on-wall fractions for fully coated and axially zoned filters at $GHSV = 8 \cdot 10^5 \text{h}^{-1}$.
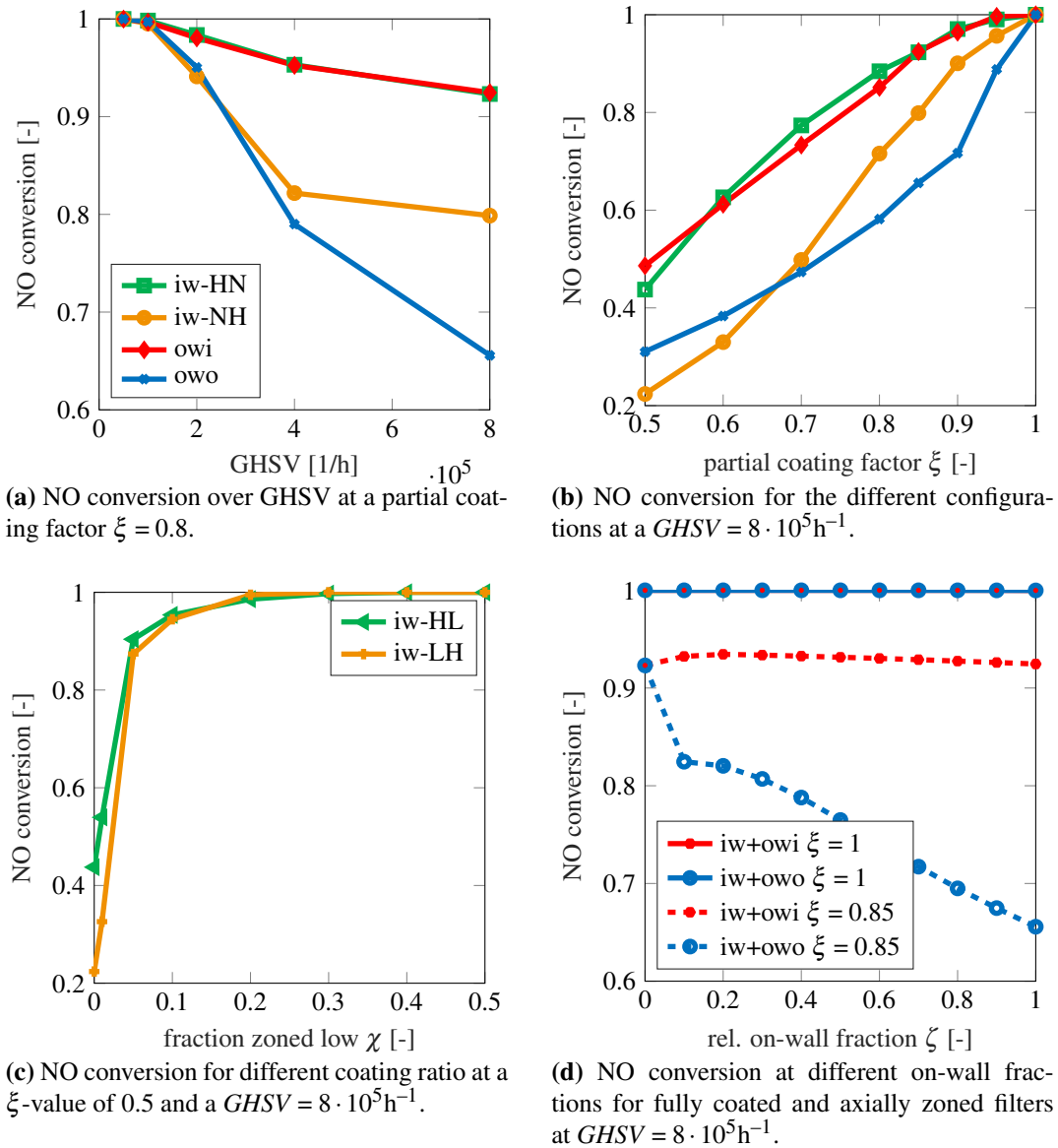
Figure 5.5: Impact of the GHSV on the considered configurations at a λ-value of 0.999

Figure 5.5a displays the impact of space velocity on NO conversion for different axially zoned configurations at a partial coating factor ξ of 0.8. The owo and iw-NH configurations with the coating gap at the front deliver a sharper decrease than the corresponding owi and iw-HN configurations. The other subplots in Figure 5.5 display the NO conversion for different coating parameters at a constant GHSV of $8 \cdot 10^5 \text{ h}^{-1}$. As can be seen in Figure 5.5b, all configurations show a considerable conversion loss when coating length is reduced which is a sign for an external mass transfer limitation as the overall catalytic

activity is the same for every filter. The owo and iw-NH configurations, however, are more strongly impacted. A configuration without coating gap (Figure 5.5c) is less strongly impacted since the fluid has to flow through a catalytic layer. A variation of the on-wall fraction ζ (Figure 5.5d) does not influence the coated length and the flow is forced to pass through the catalyst. Therefore, the high-load conversion is not affected by the ζ-value.

To further elucidate the difference between the configuration with coating gap, Figure 5.6 shows the NO concentration in the channels at a ξ-value of 0.8. Under the studied operating conditions, there exists an external mass transfer limitation [228]. This mass transfer between the channel and the wall mainly limits the conversion. Due to wall-flow, mass transfer in the inlet channel is higher than the one from the outlet channel to the wall [153, 226]. As can be seen in Figure 5.6, the NO concentration declines in the inlet channels for all configurations except the owo. Here, the NO fraction stays almost constant along the inlet channel length due to the severe diffusion limitation through the porous wall to the catalytic layer.
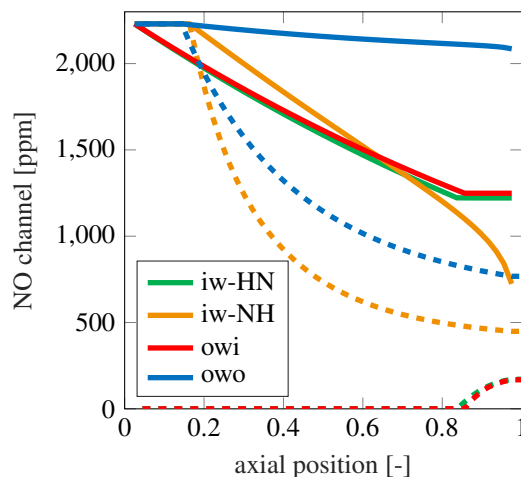
Figure 5.6: Axial NO fraction in the channels for partially coated filters at a ξ-value of 0.8. Solid lines depict the NO fraction in the inlet channel and dashed lines the one in the outlet channel.

5.3.3 Steady-State Light-Off

A fast light-off is the key for the application of catalysts in automotive exhaust gas aftertreatment because a major part of the emissions is released during the warm-up phase of the catalysts [229]. A crucial parameter to assess light-off performance is the $T50$-value that corresponds to the inlet temperature with a 50% conversion. Naturally, the choice of testing conditions, especially space velocity, impacts the $T50$. Even though the applied reaction network includes all major automotive pollutants, the next figures include only

the NO-values for readability. The interested reader can find the analysis of CO and HC emissions in 5.5.6, proving that NO is representative for the main pollutants.

(a) Quasi-steady NO light-off curve for different configurations.

(b) Comparison of NO T50 temperatures as a function of the axial partial coating ξ.

(c) T50 for different washcoat distribution.

(d) T50 at varying fraction on-wall fraction ζ.
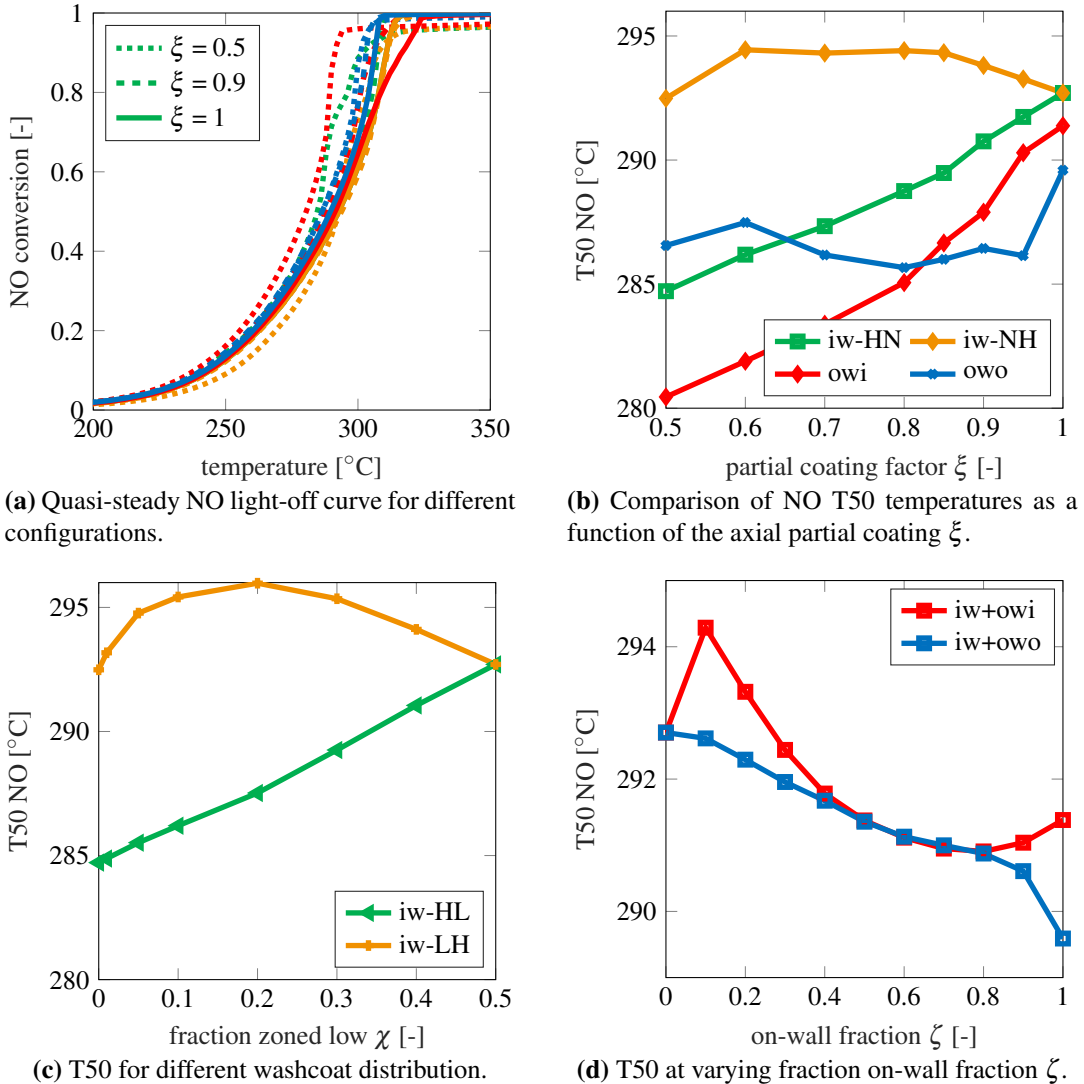
Figure 5.7: Light-off experiment with a heating rate of $1\,\mathrm{K \cdot s^{-1}}$ at $110\,\mathrm{kg \cdot h^{-1}}$.

Figure 5.7 summarizes the results of a quasi steady-state light-off experiment at a mass flow of $110\,\mathrm{kg \cdot h^{-1}}$. The inlet heating rate of $1\,\mathrm{K \cdot s^{-1}}$ is low enough that the filter heats up evenly. For the three different ξ-values of 0.5, 0.9 and 1, the light-off curves are depicted in Figure 5.7a. For all configurations, the $T50$ is in a narrow range between 280 and 300 °C.

An owi coating however shows an earlier light-off, especially when the partial coating factor ξ is decreased. Similarly, an in-wall coating with a higher amount of catalyst in the front reduces the $T50$ as can be seen when reducing the fraction zoned low χ

(Figure 5.7c). These findings are consistent with the results of Dardiotis et al. [220] and Karamitros et al. [222]. The owo and iw-NH configurations are not as strongly influenced by zoning since the $T50$-values are almost constant (Figure 5.11b, 5.11c).

(a) In-wall coated high-no (iw-HN).

(b) In-wall coated no-high (iw-NH).

(c) On-wall coated inlet channel (owi).

(d) On-wall coated outlet channel (owo).
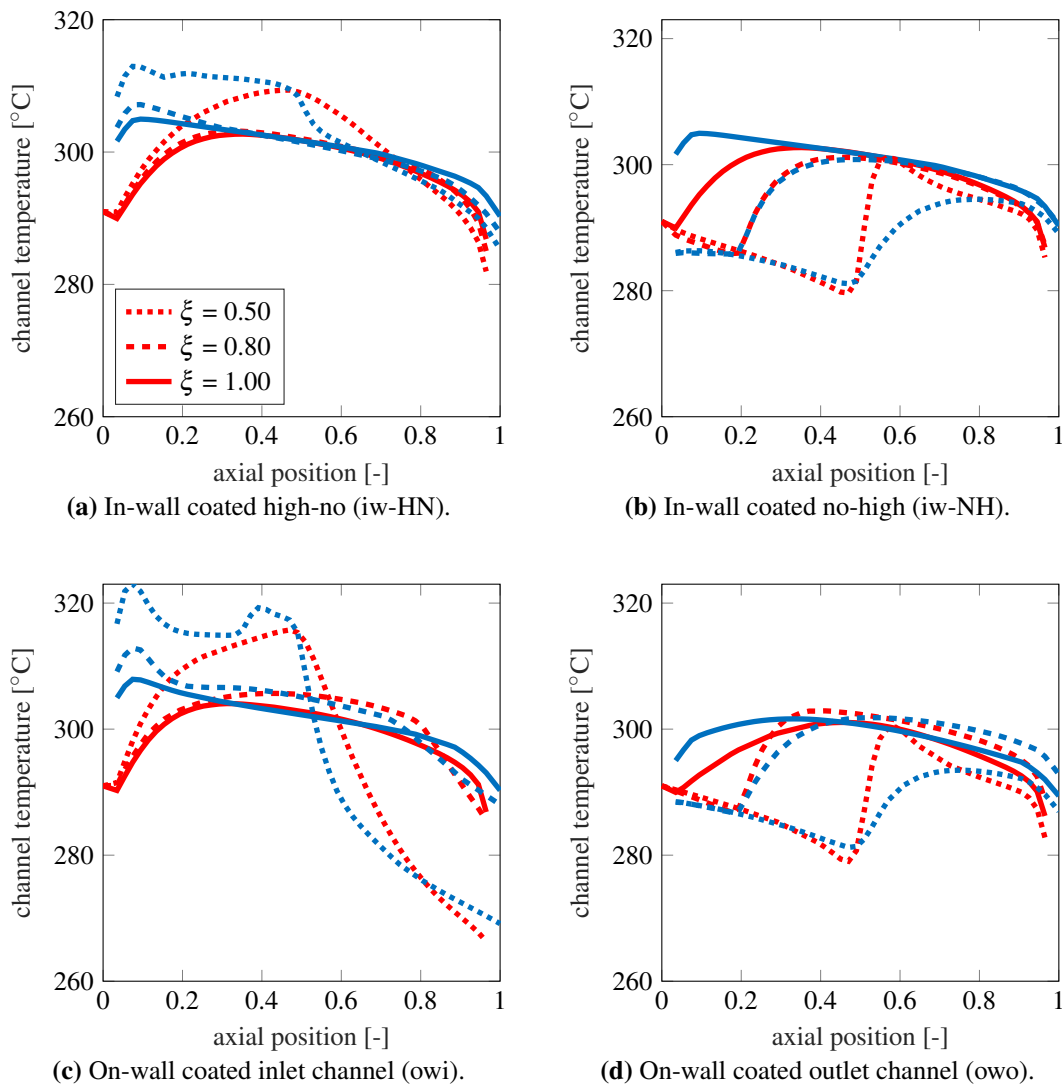
Figure 5.8: Temperature in the channels for different configurations during the light-off experiment at a inlet temperature of 290 °C. Blue lines represent the simulation result for the outlet channel and red lines represent the values for the inlet channel.

The earlier light-off of the iw-HN and owi configurations at low ξ can be explained by the thermal behavior of the monolith as discussed in the following. Figure 5.8 represents the axial temperature profiles in the inlet and outlet channel at an inlet temperature of 290 °C. The owi and iw-HN cases (Figure 5.8a, 5.8c) show a temperature increase due to exothermic reaction heat at the front part of the filter, whereas the owo and iw-NH configurations (Figure 5.8b, 5.8d) reveal a slight temperature decrease along the uncoated

length and less reaction heat downstream.
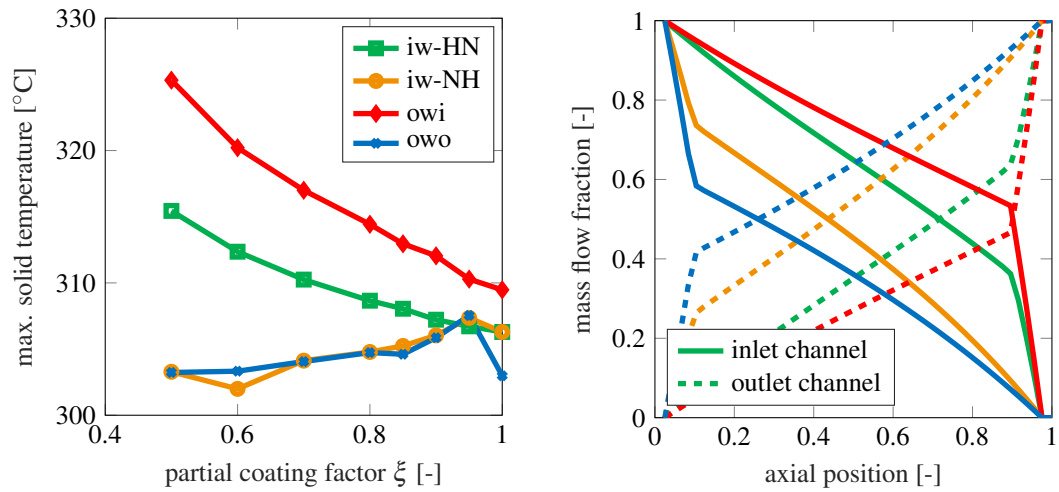
(a) Maximum solid temperature at an inlet temperature of 290 °C.

(b) Mass flow distribution for the different configuration at a partial coating factor ξ of 0.9.

Figure 5.9: Maximum temperature in the solid and mass flow distribution between inlet and outlet channel.

The maximum solid temperature, again at an inlet temperature of 290 °C, in Figure 5.9a shows that the temperature increases with more washcoat deposited at the front of the filter due to the higher reaction heat. However, more interestingly, the owo configurations at high ξ-values have the lowest $T50$-values (see Figure 5.7b) even though the reaction heat is similar to the other configurations at this ξ-range. Due to the coating gap at the front of the filter, the incoming mass flow is split equally between the inlet and outlet channel at the beginning of the on-wall layer. As can be seen in Figure 5.9b, approximately half the mass flow remains in the inlet channel downstream of the coating gap, whereas the mass flow splits more unequally for the other configurations. Therefore, the other configurations obtain a higher axial velocity in the inlet channel compared to the owo configurations, which increases the limitation due to mass transfer from the channel to the filter wall as well as decreases the residence time.

The expected drawback of approximately half the mass flow in the uncoated inlet channel for the owo configuration is strongly reduced by diffusion through the highly porous, inert filter wall. The left-hand side of Figure 5.10 shows the spatial NO conversion at a ξ-value of 0.9 for the four different configurations at a temperature slightly above the $T50$. Even though the owo case has no catalyst on the inlet channel or in its adjacent walls, the NO fraction decreases in the axial direction. This can be explained by diffusion from the inlet channel through the inert wall to the catalytic layer. Thus, against expectations, a small
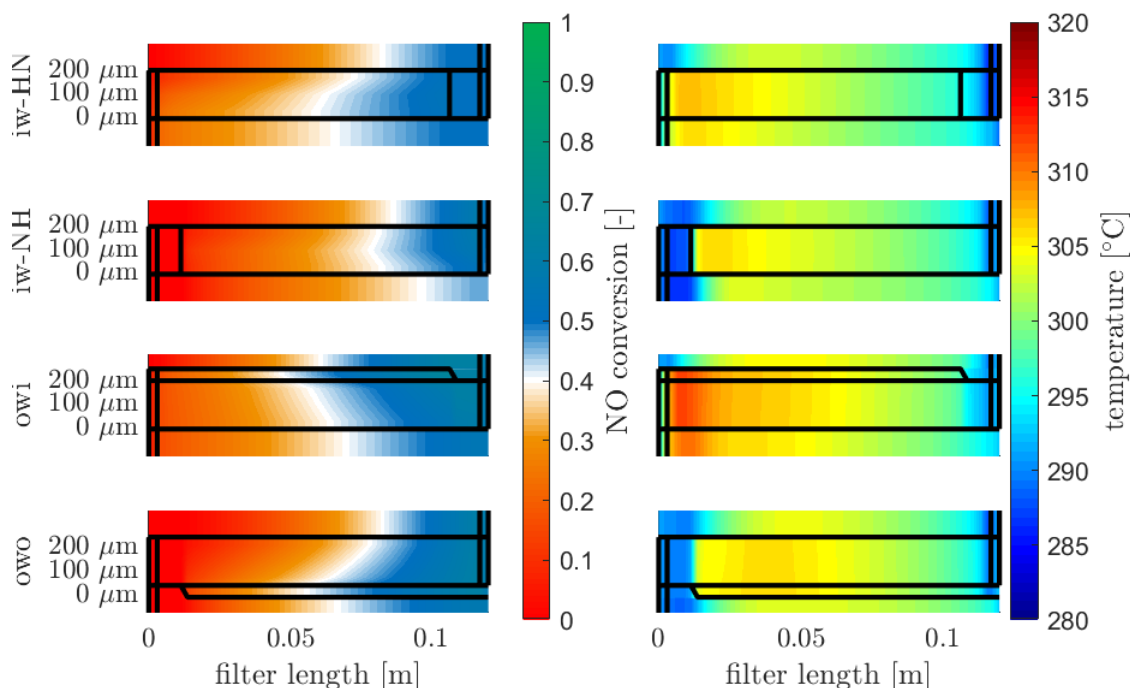
Figure 5.10: Spatial temperature and NO conversion for the iw-HN, iw-NH, owi and owo configurations at a ξ-value of 0.90 at an inlet temperature of 290 °C.

coating gap at the front of the filter can enhances the light-off behavior compared to the other configuration at the same ξ-level. The catalytic layer is even slightly colder than in the owi or iw-HN cases as can be seen from the spatial temperature distribution at the right side of Figure 5.10.

5.3.4 Transient Light-Off

Under real-world conditions in automotive aftertreatment, catalysts are usually heated at higher rates, because reducing the warm-up time is crucial to decreasing emissions. Placing the monolith close to the engine and operating in a special catalyst heating mode often achieves a heating rate of $30\,\mathrm{K{\cdot}s^{-1}}$ [126, 168, 230]. To evaluate the shown configurations under these practically relevant conditions, a corresponding light-off experiment with a faster temperature ramp from room temperature to $700\,°\mathrm{C}$ at a heating rate of $30\,\mathrm{K{\cdot}s^{-1}}$ is conducted, see Table 5.4.

Figure 5.11a shows the time-resolved NO conversion for different configurations. To evaluate the impact of the zoning parameters, again the $T50$-value is applied. Due to the faster heat up and the thermal inertia, the values, based on the inlet temperature, are higher than under quasi-steady conditions. As illustrated in Figure 5.11b, an on-wall coating
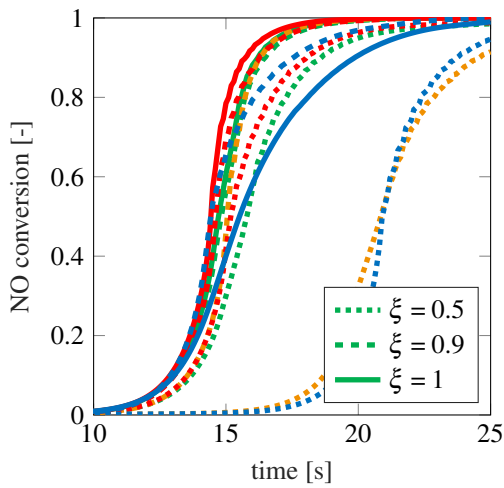
(a) Transient NO light-off curve for the iw-HN, iw-NH, owo and owo configuration at different ξ-values.
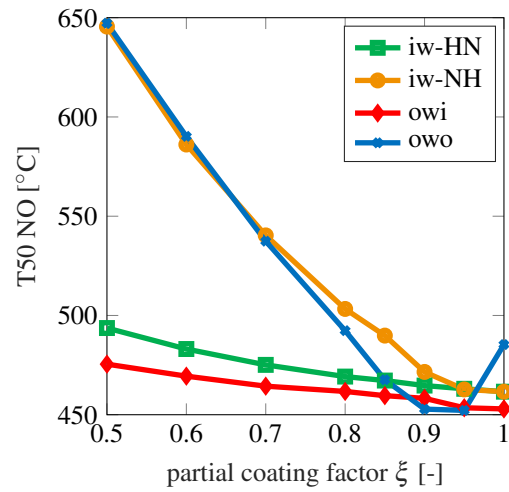
(b) Comparison of NO T50 temperatures as a function of the axial partial coating ξ.
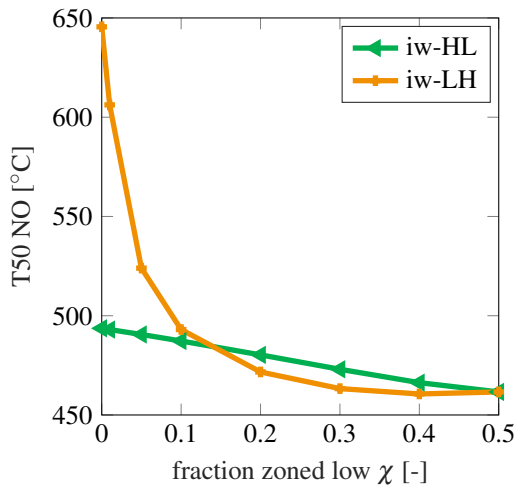
(c) T50 for the iw-HL and iw-LH configurations.
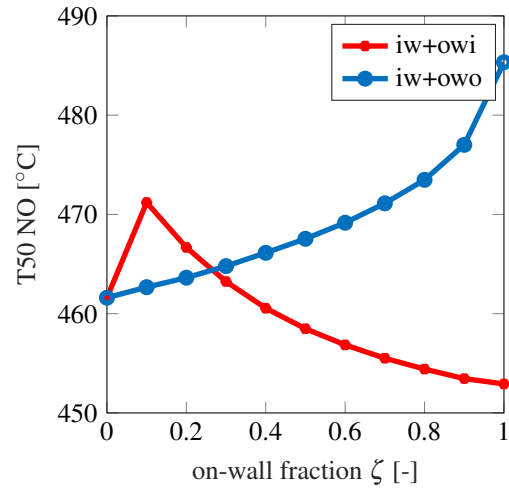
(d) T50 over the partial on-wall coating factor ζ.

Figure 5.11: Light-off experiment with an inlet heating rate of $30\,\mathrm{K{\cdot}s^{-1}}$ at $110\,\mathrm{kg{\cdot}h^{-1}}$.

of the inlet channel decreases the $T50$ compared to a solely in-wall coating, whereas especially for low ξ-values the inert thermal mass at the front drastically increases the $T50$ for the owo and iw-NH configurations. At high ξ-numbers, the different topologies become more similar: the $T50$ of the in-wall coated configuration is slightly higher than the $T50$ of the corresponding on-wall coated configuration. Again for the owo-case, the more even split of the mass flow between both channels reduces the mass transfer limitation due to the lower axial velocities. At a partial coating factor ξ of one, the $T50$ of the owo-configuration sharply increases because without the coating gap there is no beneficial split of the incoming gas flow between the channels.

In contrast to the steady-state conditions, a more dense coating of the front part does not decrease the light-off temperature under these conditions. As can be seen in Figure 5.11c, the $T50$ decreases at a more uniform coating. These results are consistent with the coating length variation (Figure 5.11a), demonstrating that at increasing ξ-values the $T50$ decreases.

Figure 5.11d depicts the ζ-variation. Since no coating gap is considered, the owo-case shows higher $T50$-values with increasing on-wall fraction, due to the thermal inertia of the uncoated filter wall. For the inlet channel coating, it can be seen that a minimum fraction of roughly half the washcoat needs to be deposited on-wall for a benefit under transient conditions. At low ζ-values the thin but dense catalytic layer acts as diffusion barrier into the coated filter wall, resulting in a higher $T50$ for these filters.

5.3.5 Summary of the Simulation Results

There is no configuration that performs best in all presented virtual experiments. To further cluster the influence of the coating parameters on the results, a combined quality factor of the catalytic performance Q_f is defined. Equations (5.9) and (5.10) apply a simple scaling with the best configuration set to one and the worst to zero. Equation (5.10) for the high-load conversion X differs from Equation (5.9) because here the highest value is ranked as one, whereas the lowest $T50$ is obviously preferable. Minimum *min* and maximum *max* are the global values over all conducted coating parameter variations.

$$Q_{f,T50} = \frac{max(T50) - T50}{max(T50) - min(T50)} \tag{5.9}$$
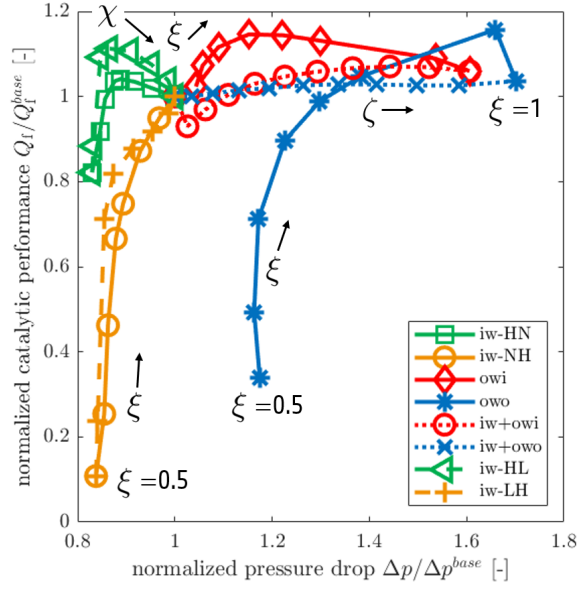
Figure 5.12: Quality factor of the catalytic performance and pressure drop normalized to the values of the *base* filter.

$$Q_{f,X} = \frac{X - min(X)}{max(X) - min(X)} \tag{5.10}$$

The quality factors for the different experiments are then combined into a single number.

$$Q_f = Q_{f,T50_{steady}} + Q_{f,T50_{transient}} + Q_{f,X} \tag{5.11}$$

For a more conclusive comparison, the resulting quality factor Q_f and the pressure drop Δp are normalized to the values of the *base* case. Thus, the uniformly in-wall coated cGPF has a normalized quality factor and pressure drop of one. Figure 5.12 depicts the normalized Q_f and Δp for all considered configurations.

As can be seen in Figure 5.12, in-wall configurations achieve the lowest pressure drop and at high partial coating factors ξ good catalytic performance. On-wall configurations, on the other hand, can perform well however with the here applied assumptions, their pressure drop is higher. A coating that concentrates mainly on the rear part of the filter yields the lowest catalytic performance.

One key aspect of cGPF is particle filtration efficiency, which is well-known to be sensitive to the microstructure of the filter. However, to incorporate the filtration performance

into the quality factor, a detailed knowledge of the resulting pore size distribution of the on-wall layer as well as of the heterogeneous in-wall coating would be necessary.

5.4 Conclusion and Outlook

Due to the distinction of in-wall and on-wall coating as well as the introduction of axial zoning, the filter reactor offers various coating topologies. For the practical deployment as cGPF, we apply three non-dimensional parameters to describe different concepts in various gradations. In a systematic, model-based evaluation, the pressure drop and the catalytic performance of these concepts are compared. A previously published and validated cGPF channel-scale model is extended by a porous media model to incorporate the impact of the washcoat loading on the porosity, permeability, and catalytic reactivity.

The simulation results reveal that, as an extreme case of zoning, a coating gap delivers a strong reduction in the pressure drop for on-wall coated filters. However, compared to an in-wall coated configuration, the pressure drop is still higher. More interestingly, the comparison under high mass flow conditions reveals that a long coated length is necessary to achieve high conversions. Under light-off conditions, the optimum coating length depends on the temperature rate. Under quasi-steady-state conditions, a high washcoat loading at the front of the filter reduces the light-off temperature due to an evolving hotspot at the front. Under transient conditions, however, a more uniform coating offers benefits. Against expectations, an on-wall coating of the outlet channel with a small gap at the front of the filter achieves the earliest light-off due to the beneficial split of the incoming mass flow between the inlet and outlet channel. Evaluating all the results show that an in-wall coated filter with a small coating gap at the rear offers the best compromise between pressure drop and chemical conversion.

In additions to the presented findings it needs to be considered, that our analysis is based on a fresh filter without aging, ash, or soot accumulation. The interplay with soot and ash will vary among the configurations. Also the thermal, as well as the chemical aging characteristics, will differ among the topologies [227]. Thermal aging could be captured by evaluating the simulated temperature during critical scenarios [231]. A different global washcoat loading that was not in the scope of this study could change the ranking due to the sensitivity of the pressure drop and wall flow on the thickness and permeability of the on-wall layer.

Summarizing, the reactor engineering analysis presented in this work demonstrates the impact of the macroscopic coating topology on filter performance and provides an explanation of the phenomena involved on reactor scale.

5.5 Appendix

The following section contains the resulting porous media characteristics depending on the coating parameters as well as the underlying model description. In addition, a grid convergence study shows that a sufficient discretization was chosen.

5.5.1 Porosity and Layer Thickness of the cGPF Configurations

Since the total washcoat mass is kept constant for every configuration, the porosity and on-wall layer thickness vary. In Figure 5.13, the resulting layer thickness and porosity are depicted as a function of the describing parameters. For the uncoated part of the filter, the properties of the bare substrate are applied.

5.5.2 Model Description

The reactor model solves the governing equations for the conservation of energy, species, and momentum for one representative pair of an inlet and an outlet channel and the separating porous wall. Whereas the species conservation and, with it, the oxidation status of the oxygen storage are treated as transient, the fluid energy and momentum balances are solved quasi-steady, leading to a significant decrease in computation time. For the solid temperature, an increased time step is applied because of the lower gradients compared to the species balance.

All governing equations are solved in Matlab R2018b. For the momentum and overall mass balance Equation (5.12) to Equation (4.10), the solver bvp4c is applied. The enthalpy balance in the channels (Equation (5.16)) is solved via ode15s and is coupled with the mass and momentum balances with a recursive scheme. A method of lines approach with the 1D+1D discretization of the channel pair integrates Equations (5.16)-(5.21) for the species and enthalpy balance utilizing the solver ode15s. For faster performance, the sparsity patterns of the corresponding Jacobi matrix are supplied and the maximum order
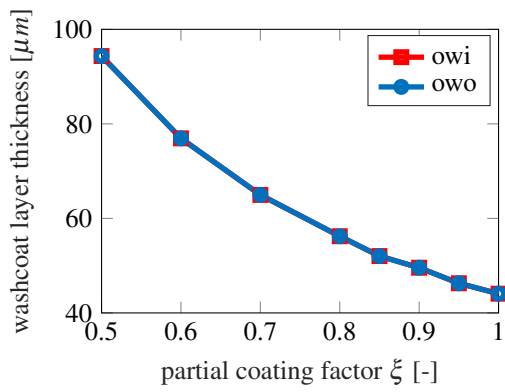
(a) On-wall layer thickness.
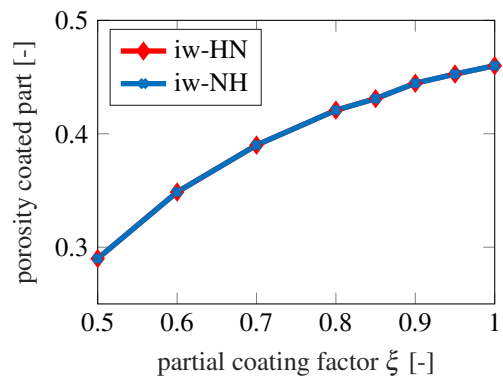
(b) Porosity of the coated part of the wall.
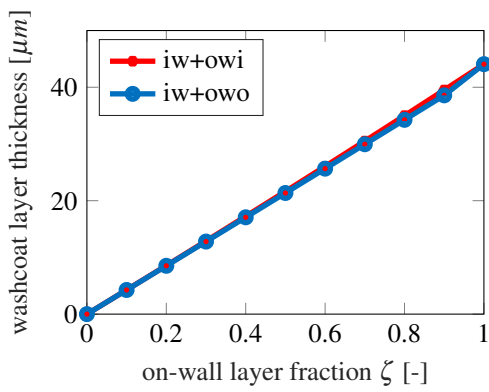
(c) On-wall washcoat thickness.
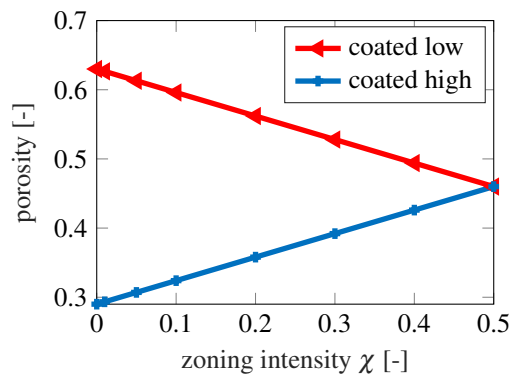
(d) Porosity of the two zones.

Figure 5.13: Resulting washcoat thickness and porosity for the different coating parameters at constant total washcoat volume.

is set to two. Additionally, all quantities are normalized to the same order of magnitude to achieve consistent tolerances.

5.5.2.1 Mass and Momentum Balance

In the following equations, index j is 1 for the inlet channel and 2 for the outlet channel. Equation (5.12) couples channel velocity v_j with the wall velocity v_w via the continuity equation:

$$D_j^2 \frac{\partial \rho_j v_j}{\partial z} = (-1)^j \cdot 4 D_j \cdot \rho_j \cdot v_w \qquad (5.12)$$

In the channels, no radial deviation of the pressure is considered. Therefore, a 1D-pressure profile p is determined by:

$$\frac{\partial p_j}{\partial z} = -\beta_j(Re_w) \cdot \frac{d(\rho_j \cdot v_j^2)}{dz} - 2 \cdot \frac{\eta_j}{D_j^2} \cdot C_{j,f}(Re_w) \cdot v_j \qquad (5.13)$$

The coefficient $\beta_j(Re_w)$ and the friction coefficient $C_{j,f}(Re_w)$ are interpolated using the tables provided by Bissett et al. [153]. The wall Reynolds number Re_w has an upper bound of three as recommended in the literature [153, 171]. The channels are coupled via Darcy's law (5.14).

$$p_1 - p_2 = \eta \cdot \frac{v_w}{k_w} \cdot t_w \qquad (5.14)$$

The additional pressure loss due to expansion and contraction at the filter's inlet and outlet are determined with Equation (5.15).

$$\Delta p_j = \frac{\zeta_j}{2\rho_j} \cdot (\frac{\dot{m}}{D_j^2})^2 \qquad (5.15)$$

Here, $\dot{m}$ is the mass flow entering or exiting the channel and the local resistance coefficient ζ_j is set to 1.25 according to Leskovjan et al. [162].

5.5.2.2 Enthalpy Balance

The heat transfer coefficient h is derived via the Nusselt correlation of Bissett et al. [153]. The porous medium is assumed as homogeneous, and the ideal gas law is used. All material data, e.g., viscosity, heat capacity, are calculated with correlations from the VDI

Heat Atlas [155].

The channel gas phase temperature is assumed quasi-steady:

$$c_{gas,p}\rho_j v_j \cdot \frac{\partial T_j}{\partial z} = \frac{4}{D_j} \cdot (h_j + (-1)^j \cdot c_{gas,p}\rho_j v_{\mathrm{w}}) \cdot (T_{\mathrm{w}}|_{x=-(1-j)\cdot t_{\mathrm{w}}} - T_j) \tag{5.16}$$

In the wall, the homogeneous temperature is derived by:

$$\bar{\rho}\bar{c}\frac{\partial T_{\mathrm{w}}}{\partial t} = \lambda_s \cdot \frac{\partial^2 T_{\mathrm{w}}}{\partial z^2} + \lambda_s \cdot \frac{\partial^2 T_{\mathrm{w}}}{\partial x^2} + \frac{v_{\mathrm{w}}\rho_{\mathrm{w}}c_{gas,p}\partial T_{\mathrm{w}}}{\partial x} + \Sigma \dot{r}_i \cdot H_B^0 \tag{5.17}$$

with $\bar{\rho}\bar{c}$ as the thermal mass of the wall defined by Equation (5.6).

To achieve consistency between the channel and wall modeling, the enthalpy flux term in through-wall direction is set to

$$\bar{\rho}\bar{c}\frac{\partial T_{\mathrm{w}}}{\partial x}|_{x=-(1-j)\cdot t_w} = \frac{4}{D_j} \cdot (h_j + (-1)^j \cdot c_{gas,p}\rho_j v_{\mathrm{w}}) \cdot (T_{\mathrm{w}}|_{x=-(1-j)\cdot t_w} - T_j) \tag{5.18}$$

at the boundaries.

5.5.2.3 Species Balance

The species balance is solved fully transient in the channels for each species with the mass transfer coefficient k_j derived from the correlation of Bissett et al. [153] under the assumption of equal values for Nusselt and Sherwood numbers.

$$\frac{\partial c_j}{\partial t} = -v_j \cdot \frac{\partial c_j}{\partial z} - \frac{4}{D_j} \cdot (k_j \cdot (c_j - c_{\mathrm{w}}|_{x=-(1-j)\cdot t_w}) + (-1)^j \cdot v_{\mathrm{w}} \cdot c_j) \tag{5.19}$$

In the wall, diffusion in the through-wall direction is considered via an effective diffusion coefficient D_{eff}. The species balance in the wall, given in Equation (5.20) with $\dot{r}$ as the reaction rate of the respective species, is determined by the reaction network of Table 5.6.

$$\frac{\partial c_{\mathrm{w}}}{\partial t} = \frac{\partial(v_{\mathrm{w}} \cdot c_{\mathrm{w}})}{\partial x} - D_{eff} \cdot \frac{\partial^2 c_{\mathrm{w}}}{\partial x^2} + \dot{r} \tag{5.20}$$

By analogy to the enthalpy balance, the boundary conditions are set to

$$D_{eff} \cdot \frac{\partial c_w}{\partial x}|_{x=-(1-j)\cdot t_w} = k_j \cdot (c_w|_{x=-(1-j)\cdot t_w} - c_j) \qquad . \tag{5.21}$$

For effective diffusion coefficient D_{eff}, the parallel pore model is used:

$$D_{i,eff} = D_{i,M} \cdot \frac{\varepsilon_w}{\tau} \tag{5.22}$$

Here, $D_{i,M}$ is the diffusion coefficient of the species i in the mixture, ε_w is the porosity of the wall, including the effect of the coating, and τ is the tortuosity, which is an empirical correction factor. The calculated $D_{i,eff}$ correspond well to the measured values of Kröcher et al. [213].

5.5.2.4 Reaction Network

Table 5.6 lists all applied reactions with their parameters. The network includes all standard reactions [126, 179, 187] and the parameters are calibrated to a fresh in-wall coated filter [168] used here as the *base* filter. The choice of two different ceria sites (fast and slow) as well as C_3H_6 as the only HC species is explained in detail in reference [168].

5.5.3 Grid Convergence Study

In order to validate the discretization choice of 50 axial elements, a grid convergence study is conducted. A transient light-off with a temperature gradient of $30\,\text{K}\cdot\text{s}^{-1}$ for the two filter configurations iw-HN and owi at a ξ-value of 0.5 is simulated. The configuration as well as the experiments are assumed as the most demanding in terms of accuracy. Figure 5.14a shows the cumulative outlet NO emissions normalized to the cumulative inlet NO emissions (NCOE) after 25 s. With the mass fractions w of a species i, Equation (5.23) determines the NCOE.

$$NCOE = (\frac{1}{\int_{t_0}^{t_{end}} \dot{m} \cdot w_j^{in} dt}) \cdot \int_{t_0}^{t} \dot{m} \cdot w_j^{out} dt \tag{5.23}$$

Table 5.6: Kinetic parameters

reaction		$A_{pre}[\frac{m^3}{s \cdot mol}]$	$E_A[-\frac{kJ}{mol}]$
R1	$CO + 0.5O_2 \rightarrow CO_2$	3.028e+21	144
R2	$H_2 + 0.5O_2 \rightarrow H_2O$	1.026e+19	85
R3	$C_3H_6 + 4.5O_2 \rightarrow 3CO_2 + 3H_2O$	5.959e+19	112
R4	$CH_4 + 2O_2 \rightarrow CO_2 + 2H_2O$	4.780e+11	124
R5	$CO + H_2O \rightleftharpoons CO_2 + H_2$	3.737e+12	75
R6	$C_3H_6 + 3H_2O \rightleftharpoons 3CO + 6H_2$	1.887e+14	120
R7	$CO + NO \rightarrow CO_2 + 0.5N_2$	7.914e+14	58
R8	$C_3H_6 + 9NO \rightarrow 3CO_2 + 4.5\,N_2$	3.590e+11	110
R9	$H_2 + N_2O \rightarrow H_2O + N_2$	3.775e+06	76
R10	$CO + 2NO \rightarrow CO_2 + N_2O$	7.412e+11	37
R11	$CO + N_2O \rightarrow CO_2 + N_2$	2.119e+13	81
R12	$0.5O_2 + fCe_2O_3 \rightarrow 2fCeO_2$	6.278e+10	75
R13	$H_2 + 2fCeO_2 \rightleftharpoons fCe_2O_3 + H_2O$	3.164e+10	80
R14	$CO + 2fCeO_2 \rightleftharpoons fCe_2O_3 + CO_2$	4.214e+14	120
R15	$C_3H_6 + 12fCeO_2 \rightarrow 6fCe_2O_3 + 3CO + 3H_2O$	2.020e+14	125
R16	$NO + Ce_2O_3 \rightarrow 2CeO_2 + 0.5N_2$	2.881e+13	105
R17	$0.5O_2 + Ce_2O_3 \rightarrow 2CeO_2$	7.853e+09	80
R18	$H_2 + 2CeO_2 \rightleftharpoons Ce_2O_3 + H_2O$	5.635e+06	85
R19	$CO + 2CeO_2 \rightleftharpoons Ce_2O_3 + CO_2$	9.580e+08	106
R20	$C_3H_6 + 12CeO_2 \rightarrow 6Ce_2O_3 + 3CO + 3H_2O$	5.396e+07	117
R21	$NO + Ce_2O_3 \rightarrow 2CeO_2 + 0.5N_2$	1.434e+08	80
R ξ_{Ox}	$PGM \rightarrow PGM-O$	4.150e+01	15
R ξ_{Red}	$PGM-O \rightarrow PGM$	2.070e-01	-8

Table 5.7: Inhibition parameters: $K_i = A_{Ad} \cdot exp(\frac{H_{Ad}}{R \cdot T})$

Parameter	$A_{Ad}[\frac{m^3}{mol}]$	$H_{mathrmAd}[\frac{J}{mol}]$
K_1	1.491e+03	629.41
K_2	1.792e+05	273.29
K_3	6.295e+02	1643.93
K_4	3.608e+02	10.38
K_5	1.490e+05	186.00
$K_{\xi,1}$	4.46e+01	0
$K_{\xi,2}$	4.15e+01	0

Table 5.8: Ceria site density

site	specific surface area $[\frac{m^2}{m^3}]$
Γ_{fast}	57.0
Γ_{slow}	68.0

In Figure 5.14b, the relative deviation to the 200 element case is illustrated. As can be seen, the relative deviation of the NCOE as well as the outlet temperature are below 1% at a discretization of 50 axial elements.
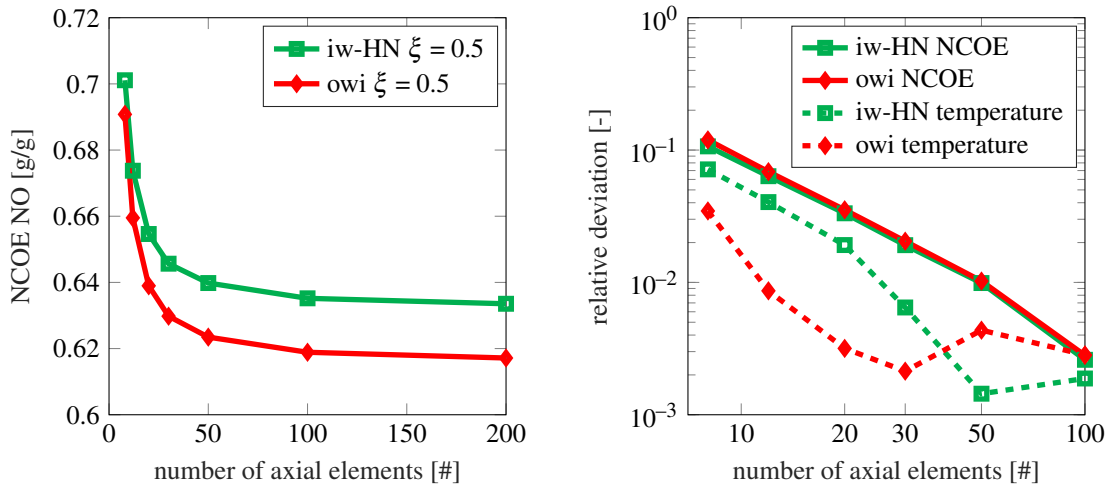
(a) Normalized cumulative outlet emissions (NCOE) of a 25 s time sequence.

(b) Relative outlet temperature and NO NCOE compared to the simulation result with an axial discretization of 200 elements.

Figure 5.14: Grid convergence study.

5.5.4 Sensitivity on the On-wall Layer Permeability

The permeability of an on-wall layer strongly depends on the macroscopic structure of the layer, e.g., cracks [110, 162]. We apply a catalytic layer permeability corresponding to values similar to the measurements of Leskovjan et al. [162]. To evaluate the impact on the pressure drop for different partial coating factors in the case of an on-wall coating in the inlet channel, a sensitivity study is shown in Figure 5.15. At decreasing permeabilities, the impact of the coating gap increases, whereas at permeabilities in the order of magnitude of the bare substrate's value ($1.6\,\mu m^2$), the contraction of the channel's cross-section is the dominant factor.
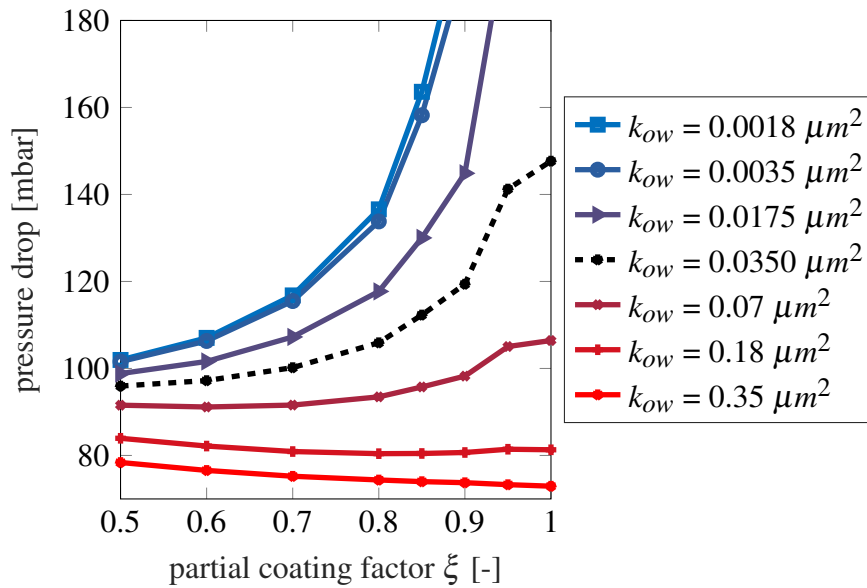
Figure 5.15: Pressure drop at $450\,\text{kg}\cdot\text{h}^{-1}$ and $800\,^{\circ}\text{C}$ for owi configurations at different ξ. The dashed line represents the filter with the on-wall layer permeability applied in this work.

5.5.5 Wall Velocities for Different Configurations

To highlight the impact of axial zoning, Figure 5.16 shows the 1D pressure profiles in the channels as well as the resulting wall velocity for different partial coating factors. As a boundary condition, the ambient pressure downstream of the filter is set to 1.2 bar to meet the expected pressure losses of the rear part of the exhaust gas system.

5.5.6 Steady-State Light-Off Data for CO and HC

As an addition to Figure 5.7 the following plots depict the $T50$-value for CO and HC (modeled as C_3H_6). As can be seen in Figure 5.17 and Figure 5.18, all trends observed for NO replicate for the other species with only slight deviations.
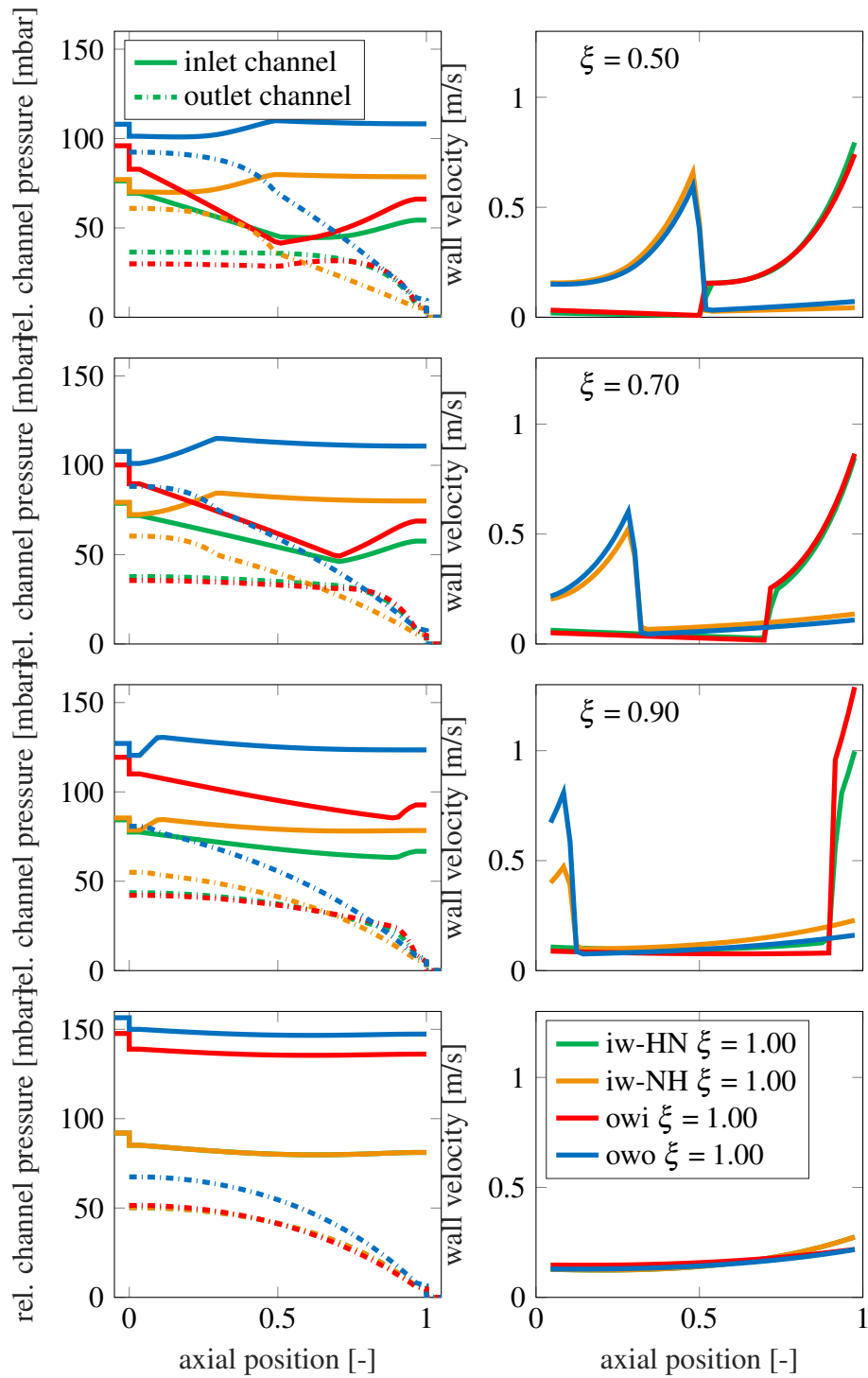
Figure 5.16: Wall velocity and pressure profiles in the inlet and outlet channels for different filter configurations at $450\,\mathrm{kg\cdot h^{-1}}$ and $800\,^\circ\mathrm{C}$.
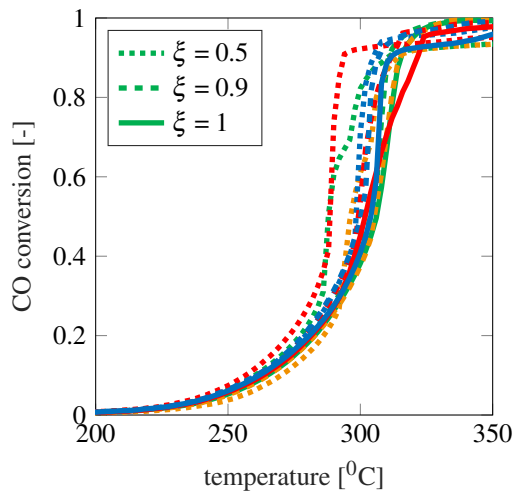
(a) Quasi-steady NO light-off curve for different configurations.
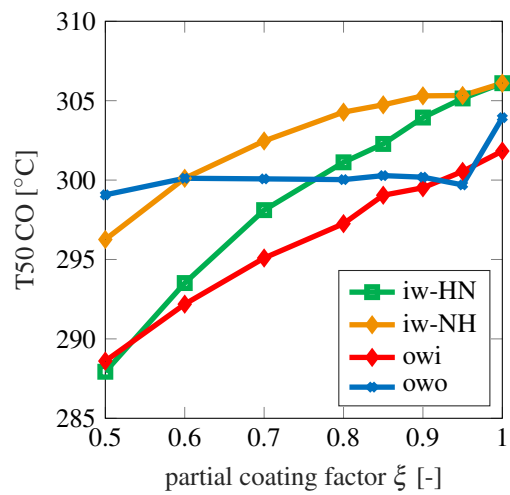
(b) Comparison of CO T50 temperatures as a function of the axial partial coating ξ.
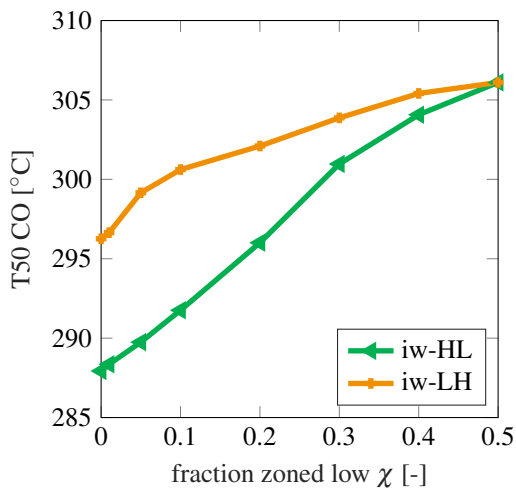
(c) T50 for different washcoat distribution.
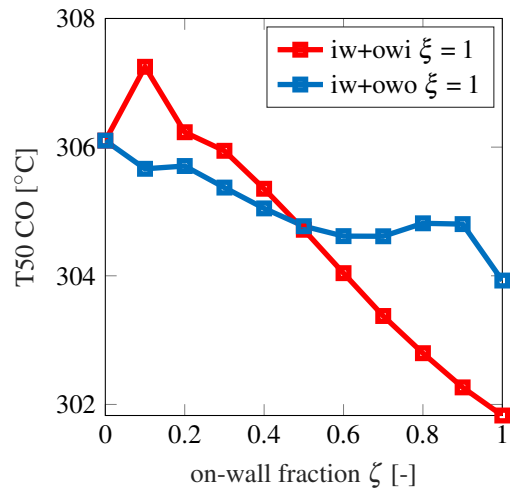
(d) T50 at varying fraction on-wall fraction ζ.

Figure 5.17: Light-off experiment with a heating rate of $1\,\mathrm{K{\cdot}s^{-1}}$ at $110\,\mathrm{kg{\cdot}h^{-1}}$.
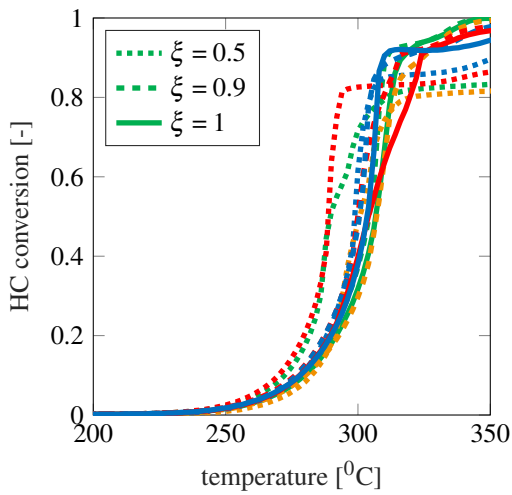
(a) Quasi-steady NO light-off curve for different configurations.
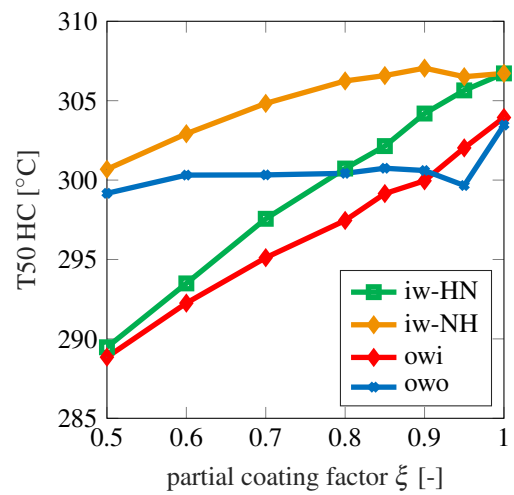
(b) Comparison of HC T50 temperatures as a function of the axial partial coating ξ.
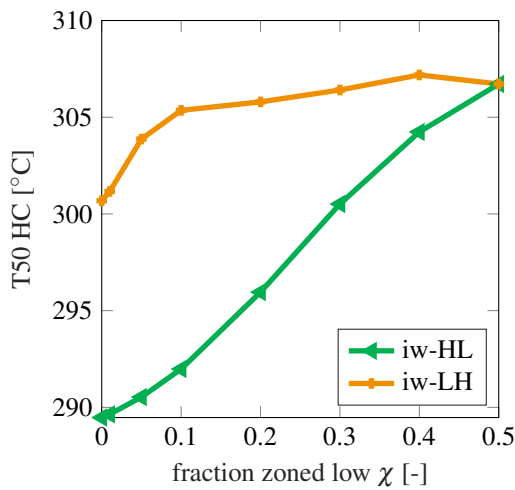
(c) T50 for different washcoat distribution.
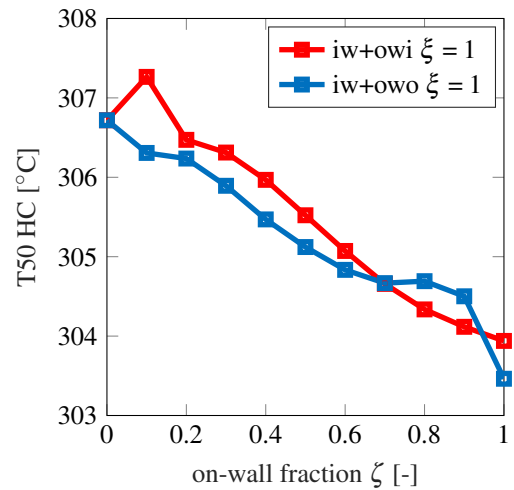
(d) T50 at varying fraction on-wall fraction ζ.

Figure 5.18: Light-off experiment with a heating rate of $1\,\mathrm{K\cdot s^{-1}}$ at $110\,\mathrm{kg\cdot h^{-1}}$.

6 Summary and Outlook

The extension of operating conditions under which upcoming vehicles must meet lower emissions standards, requires more catalytic volume that is earlier at its operating temperature. The coated gasoline particulate filter (cGPF) is a technology receiving increasing interest. The combination of the necessary GPF with a three-way catalyst at a close-coupled location in the exhaust gas aftertreatment system can help to increase the total catalytic volume and avoid heat sinks. In this thesis, the cGPF is examined from a modeling perspective, whereby each chapter extends a simulation approach. The transient processes relevant in industrial application require a macroscopic model which still addresses the chemical-physical content with sufficient depth. Therefore, pore scale phenomena are simplified in a manner that allows to calculate transient processes with all relevant species in order to advance modeling strategies for exhaust gas aftertreatment design.

In a first step, the filtration characteristics of uncoated GPFs under industrial relevant operating conditions are investigated. In a channel scale model that discretizes the channel axially and the wall in axial and through wall direction (1D+1D), a macroscopic filtration approach is embedded. This approach describes the pore scale characteristics by the means of statistical functions. A new correlation for the filtration due to inertial deposition is implemented. Previously, most filtration models, aimed for the development of diesel particulate filters, were validated at lower temperatures and mass flow than the ones encountered for gasoline engines. Thus, the particle size resolved fresh filtration efficiency of seven different cordierite filters was determined on a specially equipped dynamic engine test bench. After a minor calibration step, the resulting simulation model accurately predicts transient cold-start experiments. In addition, the influence of the wall thickness and the pore-size distribution, experimentally determined with the remaining five filters, is captured correctly by the proposed approach. Here, the transient cold start filtration efficiency is strongly dependent on the mean pore size whereas the wall thickness impacts the result less. A comparison of five different filtration models with the proposed novel approach shows that the results of most modeling approaches are similar at low space velocities. However, a further increase in space velocity distinguishes the

approaches. The proposed approach yields a stagnation in the filtration efficiency whereas the models show a decrease. From a practical view, the experimental and model findings mean that an increase in the open frontal area, thus a decrease in space velocity, yields large benefits in pressure drop but has only minor impact on filtration. The pore size distribution, on the other hand, has the greatest influence on the filtration efficiency and should be optimized.

In a next step, the simulation is extended to model the filtration efficiency of coated filters. The, therefore, necessary pore scale characteristics are determined by highly resolved 3D X-ray microscopy of two differently coated GPFs and their corresponding bare substrate. The model predictions fit the accompanying measurements of the filters conducted on a dynamic engine test bench well. In addition, the influence of the coating on the filter's permeability was investigated via lattice-Boltzmann CFD calculations and measurements. A simplified correlation for the change in permeability due to coating dependent on the substrate's porosity and the bare substrate's characteristics was proposed. The resulting filtration model can reliably predict the fresh filtration efficiency of coated and uncoated GPFs under a vast variety of operating conditions. The simulation as well as the measurements reveal that cGPFs have disadvantages in filtration efficiency compared to uncoated filters. The high porosity and the larger pore sizes necessary to integrate the coating reduce the filtration efficiency. Additionally, both coated filters show a reduction of small pores due to the coating. This change in the microstructure further decreases the filtration performance.

In order to capture the chemical conversion behavior, the model is extended with a global reaction mechanism. The mechanism includes two different ceria sites and a time dependent extent of oxidation of the active centers in order to accurately model all relevant transient phenomena. The catalytic performance of an in-wall coated GPF is determined on a dynamic engine test bench to calibrate and validate the approach. Since fluctuations in the λ-value of the incoming feed are next to the cold start a major source of emission under practical conditions, measurements and simulation under controlled high frequency λ-oscillation are conducted. Under these conditions the light-off temperature is lower than under steady-state conditions. This is a phenomenon that the model correctly replicates. Under warm conditions, the λ oscillations result in a enlarged NO conversion window. Here, the time- and spatially-resolved extent of ceria site oxidation determined with the simulation model explain this behavior. During fuel-rich phases, the oxygen storage in the front part of the filter is depleted. During the subsequent lean peak the oxygen storage can absorb a part of the lean pulse even if the average λ-value is on the lean side. Due to the broad validation basis, the reaction mechanism can be applied to

model a variety of driving cycles or scenarios.

In a last step, a simulation study investigates the impact of the coating technology on the chemical conversion behavior of the filter. Three coating parameters are introduced to describe the washcoat distribution on channel scale. Under the assumption of constant properties for the uncoated substrate and a constant available mass of catalyst, the catalyst distribution is varied. With the application of the developed predictive porous media model, the pressure drop, high-load conversion and light-off performance of each coating configuration are evaluated. The simulation results reveal that no configuration performs best under all conditions. However, zoning increases especially the light-off performance compared to uniformly coated filters. A higher washcoat loading in the front part of the filter wall decreases the steady-state as well as transient light-off temperature without severe penalties during high load experiments. Notable is the good performance of filter with solely on-wall coating on the outlet channel. If a coating gap is inserted in the front part of this filter, the light-off temperature is strongly reduced due to the beneficial split of the incoming mass flow between the inlet and outlet channel. The presented reactor engineering analysis explains the impact of the macroscopic coating topology on filter performance and can be applied to optimize the coating of GPFs.

While important insights are provided in this thesis, the shown modeling approach has still potential for further optimization. For the validation of the reaction mechanism, only a fresh in-wall coated cGPF was applied. Here, detailed measurements with different coating technologies, e.g. partial on-wall, and aging states of the filter could be applied. Also, at the moment, the reaction kinetics only includes the major pollutants. A further extension to insert secondary emissions, e.g. ammonia or formaldehyde, would be helpful. However, suitable measurement equipment to determine the concentration of these species during dynamic operations is rare.
The Nu and Sh correlations for heat and mass transfer remain a major element of uncertainty. Whereas, there are many works focusing on these correlation for flow-through monoliths, e.g. classical TWCs, the only modeling studies for filters apply the strong simplifications of a developed, laminar flow along the whole channel. Mostly, the light-off behavior is affected by the heat and mass transfer. Here, fundamental modeling work joint with validation measurements of uncoated filters would be necessary to propose new correlations.

Due to the lower filtration efficiency of coated filters compared to conventional GPFs, there is the possibility to integrate an inert membrane similar to an ash or soot layer

on the inlet channel [98, 99]. This fine, highly porous layer enhances fresh filtration efficiency because of its small pore size. In addition, large pore openings on the inlet channel surface are filled. The interaction of the porous media with this inert membrane strongly influences the filtration efficiency and the resulting pressure drop. Further investigations are required in order to incorporate such a membrane into a simulation model. Especially, highly resolved X-Ray computed tomography is helpful to understand the resulting structure on the inlet channel after inserting the membrane.

Next to improvement of the underlying models in the current scope, a broader application should be considered as well. Obviously, the presented reaction mechanism can also be applied to conventional TWCs. With ability to capture the behavior of the exhaust gas system as a whole, the development of λ-control strategies can be supported with simulations. Future legislation may require the onboard monitoring of the emitted emissions. The simulation model in its current state is not suitable for this task since it does not have real time capability. However, due to its physical foundation, extrapolation is possible which allows the build of reduced order models with far less measuring effort.

Bibliography

[1]   M. Crippa, G. Janssens-Maenhout, D. Guizzardi, S. Galmarini, *Journal of Environmental Management* **2016**, *183*, 959–971.

[2]   J. Huang, X. Pan, X. Guo, G. Li, *The Lancet Planetary Health* **2018**, *2*, e313–e323.

[3]   R. Stone, *Science* **2002**, *298*, 2106–2107.

[4]   C. A. Pope, M. Ezzati, D. W. Dockery, *The New England Journal of Medicine* **2009**, *360*, 376–386.

[5]   V. Matthias, J. Bieser, T. Mocanu, T. Pregger, M. Quante, M. O. Ramacher, S. Seum, C. Winkler, *Transportation Research Part D: Transport and Environment* **2020**, *87*, 102536.

[6]   S. B. Kang, S. B. Nam, B. K. Cho, I.-S. Nam, C. H. Kim, S. H. Oh, *Catalysis Today* **2014**, *231*, 3–14.

[7]   M. Tanaka, Y. Tsujimoto, T. Miyazaki, M. Warashina, S. Wakamatsu, *Chemosphere - Global Change Science* **2001**, *3*, 185–197.

[8]   T. W. Chan, E. Meloche, J. Kubsh, R. Brezny, *Environmental Science & Technology* **2014**, *48*, 6027–6034.

[9]   R. Niranjan, A. K. Thakur, *Frontiers in Immunology* **2017**, *8*, 763.

[10] B. A. A. L. van Setten, M. Makkee, J. A. Moulijn, *Catalysis Reviews* **2001**, *43*, 489–564.

[11] M. Shima, *Nihon eiseigaku zasshi. Japanese Journal of Hygiene* **2017**, *72*, 159–165.

[12] M. V. Twigg, *Applied Catalysis B: Environmental* **2007**, *70*, 2–15.

[13] J. Colls, *Air Pollution*, CRC Press, **2002**.

[14] *Traffic and Environment*, (Eds.: W. Berg, D. Gruden, O. Hutzinger), Springer, Berlin, **2003**.

[15] M. Shelef, R. McCabe, *Catalysis Today* **2000**, *62*, 35–50.

[16] Umweltbundesamt, Die europäische Abgas-Gesetzgebung, (Ed.: Umweltbundesamt), **2020**.

[17] J. Pavlovic, B. Ciuffo, G. Fontaras, V. Valverde, A. Marotta, *Transportation Research Part A: Policy and Practice* **2018**, *111*, 136–147.

[18] M. Dietrich, X. Chen, M. Sarkar, *SAE International Journal of Advances and Current Practices in Mobility* **2021**, *3*, 516–527.

[19] R. Suarez-Bertoa, V. Valverde, M. Clairotte, J. Pavlovic, B. Giechaskiel, V. Franco, Z. Kregar, C. Astorga, *Environmental Research* **2019**, *176*, 108572.

[20] J. Gallus, U. Kirchner, R. Vogt, T. Benter, *Transportation Research Part D: Transport and Environment* **2017**, *52*, 215–226.

[21] B. Degraeuwe, M. Weiss, *Environmental Pollution (Barking Essex: 1987)* **2017**, *222*, 234–241.

[22] S. Kumar Pathak, V. Sood, Y. Singh, S. A. Channiwala, *Transportation Research Part D: Transport and Environment* **2016**, *44*, 157–176.

[23] S. Kwon, Y. Park, J. Park, J. Kim, K.-H. Choi, J.-S. Cha, *The Science of the Total Environment* **2017**, *576*, 70–77.

[24] J. E. Jonson, J. Borken-Kleefeld, D. Simpson, A. Nyíri, M. Posch, C. Heyes, *Environmental Research Letters* **2017**, *12*, 094017.

[25] J. Pavlovic, K. Anagnostopoulos, M. Clairotte, V. Arcidiacono, G. Fontaras, I. P. Rujas, V. V. Morales, B. Ciuffo, *Transportation Research Record: Journal of the Transportation Research Board* **2018**, *2672*, 23–32.

[26] M. Weiss, P. Bonnel, J. Kühlwein, A. Provenza, U. Lambrecht, S. Alessandrini, M. Carriero, R. Colombo, F. Forni, G. Lanappe, P. Le Lijour, U. Manfredi, F. Montigny, M. Sculati, *Atmospheric Environment* **2012**, *62*, 657–665.

[27] R. O'Driscoll, M. E. J. Stettler, N. Molden, T. Oxley, H. M. ApSimon, *The Science of the Total Environment* **2018**, *621*, 282–290.

[28] T. Khan, H. C. Frey, *The Science of the Total Environment* **2018**, *622-623*, 790–800.

[29] B. Giechaskiel, F. Riccobono, T. Vlachos, P. Mendoza-Villafuerte, R. Suarez-Bertoa, G. Fontaras, P. Bonnel, M. Weiss, *Frontiers in Environmental Science* **2015**, *3*, 919.

[30] J. Ko, K. Kim, W. Chung, C.-L. Myung, S. Park, *Fuel* **2019**, *238*, 363–374.

[31] B. Giechaskiel, V. Valverde, A. Kontses, A. Melas, G. Martini, A. Balazs, J. Andersson, Z. Samaras, P. Dilara, *Catalysts* **2021**, *11*, 607.

[32] European comissions, COMMISSION REGULATION (EU) 2017/1151, **6.2017**.

[33] R. van Basshuysen, F. Schäfer, *Handbuch Verbrennungsmotor: Grundlagen, Komponenten, Systeme, Perspektiven*, 7., vollst. überarb. und erw. Aufl., Springer Vieweg, Wiesbaden, **2015**.

[34] D. Schmidt, H. Maschmeyer, C. Beidl, F. Raß in *VPC – Simulation und Test 2016*, (Eds.: J. Liebl, C. Beidl), Proceedings, Springer Fachmedien Wiesbaden, Wiesbaden, **2017**, pp. 1–18.

[35] G. H. Abd-Alla, *Energy Conversion and Management* **2002**, *43*, 1027–1042.

[36] F. Fricke, PhD thesis, Aachen, **2007**.

[37] T. Kobayashi, T. Yamada, K. Kayano, *Applied Catalysis B: Environmental* **2001**, *30*, 287–292.

[38] Q. Wang, G. Li, B. Zhao, M. Shen, R. Zhou, *Applied Catalysis B: Environmental* **2010**, *101*, 150–159.

[39] J. Wang, H. Chen, Z. Hu, M. Yao, Y. Li, *Catalysis Reviews* **2015**, *57*, 79–144.

[40] M. Haneda, T. Kaneko, N. Kamiuchi, M. Ozawa, *Catalysis Science & Technology* **2015**, *5*, 1792–1800.

[41] S. Rood, S. Eslava, A. Manigrasso, C. Bannister, *Proceedings of the Institution of Mechanical Engineers Part D: Journal of Automobile Engineering* **2020**, *234*, 936–949.

[42] W. A. Mannion, K. Aykan, J. G. Cohn, C. E. Thompson, J. J. Mooney in *Catalysts for the Control of Automotive Pollutants*, (Ed.: J. E. McEvoy), Advances in Chemistry, American Chemical Society, WASHINGTON, D. C., **1975**, pp. 1–13.

[43] S. B. Kang, I.-S. Nam, B. K. Cho, C. H. Kim, S. H. Oh, *Chemical Engineering Journal* **2015**, *259*, 519–533.

[44] K. Ramanathan, C. S. Sharma, *Industrial & Engineering Chemistry Research* **2011**, *50*, 9960–9979.

[45] J. Gong, C. Rutland in SAE Technical Paper Series, SAE International, **2013**.

[46] T. Okajima, S. Sivakumar, H. Shingyouchi, K. Yamaguchi, J. Kusaka, M. Nagata, *Industrial & Engineering Chemistry Research* **2021**, *60*, 1583–1601.

[47] H. Santos, M. Costa, *Energy Conversion and Management* **2008**, *49*, 291–300.

[48] D. Feriyanto, H. Pranoto, H. Carles, A. M. Leman, *IOP Conference Series: Earth and Environmental Science* **2020**, *485*, 012004.

[49] D. Chatterjee, O. Deutschmann, J. Warnatz, *Faraday Discussions* **2002**, *119*, 371–384.

[50] *Ottomotor mit Direkteinspritzung: Verfahren, Systeme, Entwicklung, Potenzial*, 1. Aufl., (Ed.: R. van Basshuysen), Vieweg, Wiesbaden, **2007**.

[51] J. Kašpar, P. Fornasiero, M. Graziani, *Catalysis Today* **1999**, *50*, 285–298.

[52] K. J. Springer, R. C. Stahman in SAE Technical Paper Series, SAE International, **1977**.

[53] J. S. Howitt, M. R. Montierth, *SAE Transactions* **1981**, *90*, 493–501.

[54] K. J. Baumgard, D. B. Kittelson in SAE International, **1985**.

[55] O. Salvat, P. Marez, G. Belot, *SAE Transactions* **2000**, *109*, 227–239.

[56] F. Zhao, M.-C. Lai, D. Harrington, *Progress in Energy and Combustion Science* **1999**, *25*, 437–562.

[57] P. G. Fischer, PhD thesis, Otto-von-Guericke-Universität Magdeburg, Fakultät für Maschinenbau, **2020**.

[58] *Soot Formation in Combustion*, (Eds.: V. I. Goldanskii, F. P. Schäfer, J. P. Toennies, H. K. V. Lotsch, H. Bockhorn), Springer Berlin Heidelberg, Berlin, Heidelberg, **1994**.

[59] C. Schueck, T. Koch, W. Samenfink, E. Schuenemann, S. Tafel, O. Towae, *SAE International Journal of Engines* **2016**, *9*, 2010–2021.

[60] D. E. Hall, C. J. Dickens in SAE Technical Paper Series, SAE International, **1999**.

[61] B. D. Stojkovic, T. D. Fansler, M. C. Drake, V. Sick, *Proceedings of the Combustion Institute* **2005**, *30*, 2657–2665.

[62] S. Viswanathan, D. Rothamer, A. Zelenyuk, M. Stewart, D. Bell, *Journal of Aerosol Science* **2017**, *113*, 250–264.

[63] S. Frommater, J. Neumann, C. Hasse, *International Journal of Engine Research* **2018**, *19*, 168–178.

[64] S. Frommater, J. Neumann, C. Hasse, *International Journal of Engine Research* **2021**, *22*, 1166–1179.

[65] A. Ibald-Mulli, H.-E. Wichmann, W. Kreyling, A. Peters, *Journal of Aerosol Medicine* **2002**, *15*, 189–201.

[66] A. Valavanidis, K. Fiotakis, T. Vlachogianni, *Journal of Environmental Science and Health. Part C* **2008**, *26*, 339–362.

[67] B. Giechaskiel, A. Joshi, L. Ntziachristos, P. Dilara, *Catalysts* **2019**, *9*, 586.

[68] A. Mamakos, N. Steininger, G. Martini, P. Dilara, Y. Drossinos, *Atmospheric Environment* **2013**, *77*, 16–23.

[69] B. Giechaskiel, A. Mamakos, J. Andersson, P. Dilara, G. Martini, W. Schindler, A. Bergmann, *Aerosol Science and Technology* **2012**, *46*, 719–749.

[70] M.-C. O. Chang, J. E. Shields, *Journal of the Air & Waste Management Association* **2017**, *67*, 677–693.

[71] A. Überall, R. Otte, P. Eilts, J. Krahl, *Fuel* **2015**, *147*, 203–207.

[72] R. Zhan, S. T. Eakle, P. Weber in SAE Technical Paper Series, SAE International, **2010**.

[73] A. Craig, J. Warkins, K. Aravelli, D. Moser, L. Yang, D. Ball, T. Tao, D. Ross, *SAE International Journal of Engines* **2016**, *9*, 1276–1288.

[74] S. Spiess, K.-F. Wong, J.-M. Richter, R. Klingmann, *Topics in Catalysis* **2013**, *56*, 434–439.

[75] T. W. Chan, M. Saffaripour, F. Liu, J. Hendren, K. A. Thomson, J. Kubsh, R. Brezny, G. Rideout, *Emission Control Science and Technology* **2016**, *2*, 75–88.

[76] J. S. Howitt, *Diesel Exhaust Aftertreatment, 1998*, SAE International, **1998**.

[77] H. Lüders, P. Stommel, S. Geckler in SAE Technical Paper Series, SAE International, **1999**.

[78] A. G. Konstandopoulos, M. Kostoglou, E. Skaperdas, E. Papaioannou, D. Zarvalis, E. Kladopoulou in *SAE Technical Paper Series 2000*, *Vol. 2000-01-1016*, SAE International, **2000**.

[79] B. Guan, R. Zhan, H. Lin, Z. Huang, *Journal of Environmental Management* **2015**, *154*, 225–258.

[80] C. Lambert, T. Chanko, D. Dobson, X. Liu, J. Pakko, *Emission Control Science and Technology* **2017**, *3*, 105–111.

[81] Y. Otani, C. Kanaoka, H. Emi, *Aerosol Science and Technology* **1989**, *10*, 463–474.

[82] K. W. Lee, J. A. Gieseke, *Environmental Science & Technology* **1979**, *13*, 466–470.

[83] J. Gong, C. J. Rutland, *Environmental Science & Technology* **2015**, *49*, 4963–4970.

[84] J. R. Serrano, H. Climent, P. Piqueras, E. Angiolini, *Energy* **2016**, *112*, 883–898.

[85] J. Gong, M. L. Stewart, A. Zelenyuk, A. Strzelec, S. Viswanathan, D. A. Rothamer, D. E. Foster, C. J. Rutland, *Chemical Engineering Journal* **2018**, *338*, 15–26.

[86] T. Boger, D. Rose, P. Nicolin, N. Gunasekaran, T. Glasson, *Emission Control Science and Technology* **2015**, *1*, 49–63.

[87] M. Plachá, P. Kočí, M. Isoz, M. Svoboda, E. Price, D. Thompsett, K. Kallis, A. Tsolakis, *Chemical Engineering Science* **2020**, *226*, 115854.

[88] T. Boger in *Reducing Particulate Emissions in Gasoline Engines*, (Ed.: SAE International), **2018**, pp. 115–144.

[89] Y. Ito, T. Shimoda, T. Aoki, Y. Shibagaki, K. Yuuki, H. Sakamoto, C. Vogt, T. Matsumoto, W. Heuss, P. Kattouah, M. Makino, K. Kato in SAE Technical Paper Series, SAE International, **2013**.

[90]   Y. Ito, T. Shimoda, T. Aoki, K. Yuuki, H. Sakamoto, K. Kato, D. Thier, P. Kattouah, E. Ohara, C. Vogt in *SAE Technical Paper Series*, SAE International, **2015**.

[91]   I. Mikulic, H. Koelmann, S. Majkowski, P. Vosejpka, *Proceedings of 19. Aachener Kolloquium Fahrzeug- und Motorentechnik* **2010**, 449.

[92]   L. Hentschel, W. Demmelbauer-Ebner, J. Theobald, W. Wendt, *Proceedings of 26. Aachener Kolloquium Fahrzeug- und Motorentechnik* **2017**, 971.

[93]   Q. Porter, A. Strzelec in *SAE International*, **2019**.

[94]   J. Yang, P. Roth, T. D. Durbin, K. C. Johnson, D. R. Cocker, A. Asa-Awuku, R. Brezny, M. Geller, G. Karavalakis, *Environmental Science & Technology* **2018**, *52*, 3275–3284.

[95]   R. Walter, J. Neumann, O. Hinrichsen, *Environmental Science & Technology* **2020**, *54*, 9285–9294.

[96]   T. A. Nijhuis, A. E. W. Beers, T. Vergunst, I. Hoek, F. Kapteijn, J. A. Moulijn, *Catalysis Reviews* **2001**, *43*, 345–380.

[97]   M. Blažek, M. Žalud, P. Kočí, A. York, C. M. Schlepütz, M. Stampanoni, V. Novák, *Chemical Engineering Journal* **2021**, *409*, 128057.

[98]   Q. Porter, A. Strzelec in *SAE International*, **2019**.

[99]   D. Rose, T. Boger, H. Wu, I.-O. Roychelle, *MTZ - Motortechnische Zeitschrift* **2021**, 60–63.

[100] P. Kočí, M. Isoz, M. Plachá, A. Arvajová, M. Václavík, M. Svoboda, E. Price, V. Novák, D. Thompsett, *Catalysis Today* **2017**, DOI `10.1016/j.cattod.2017.12.025`.

[101] *Filtration: Principles and Practices*, 2. ed., rev. and expanded., (Ed.: M. J. Matteson), Dekker, New York, NY, **1987**.

[102] Y. Liu, J. Gong, J. Fu, H. Cai, G. Long, *Journal of Aerosol Science* **2009**, *40*, 307–323.

[103] I. Belot, D. Vidal, R. Greiner, M. Votsmeier, R. E. Hayes, F. Bertrand, *Chemical Engineering Journal* **2021**, *406*, 127040.

[104] J. Gong, *Passive Ammonia SCR and Filtration Modeling for Fuel-Neutral Engine Aftertreatment Systems*, Ann Arbor, MI : ProQuest LLC, 2014, **2014**.

[105] T. Tosco, D. L. Marchisio, F. Lince, R. Sethi, *Transport in Porous Media* **2013**, *96*, 1–20.

[106] G. A. Narsilio, O. Buzzi, S. Fityus, T. S. Yun, D. W. Smith, *Computers and Geotechnics* **2009**, *36*, 1200–1206.

[107] W. Long, M. Hilpert, *Environmental Science & Technology* **2009**, *43*, 4419–4424.

[108] W. Long, H. Huang, J. Serlemitsos, E. Liu, A. H. Reed, M. Hilpert, *Colloids and Surfaces A: Physicochemical and Engineering Aspects* **2010**, *358*, 163–171.

[109] G. Boccardo, D. L. Marchisio, R. Sethi, *Journal of Colloid and Interface Science* **2014**, *417*, 227–237.

[110] P. Kočí, M. Isoz, M. Plachá, A. Arvajová, M. Václavík, M. Svoboda, E. Price, V. Novák, D. Thompsett, *Catalysis Today* **2019**, *320*, 165–174.

[111] S. Kuwabara, *Journal of the Physical Society of Japan* **1959**, *14*, 527–532.

[112] J. Happel, *AIChE Journal* **1959**, *5*, 174–177.

[113] S. Viswanathan, D. A. Rothamer, D. E. Foster, T. D. Fansler, A. Zelenyuk, M. L. Stewart, D. M. Bell, *International Journal of Engine Research* **2016**, *18*, 543–559.

[114] W. C. Hinds, *Aerosol Technology: Properties, Behavior, and Measurement of Airborne Particles*, Second Edition, Wiley-Interscience, s.l., **1999**.

[115] E. A. Kladopoulou, S. L. Yang, J. H. Johnson, G. G. Parker, A. G. Konstandopoulos, A Study Describing the Performance of Diesel Particulate Filters During Loading and Regeneration - A Lumped Parameter Model for Control Applications, **2003**.

[116] E. Ohara, Y. Mizuno, Y. Miyairi, T. Mizutani, K. Yuuki, Y. Noguchi, T. Hiramatsu, M. Makino, A. Takahashi, H. Sakai, M. Tanaka, A. Martin, S. Fujii, P. Busch, T. Toyoshima, T. Ito, I. Lappas, C. D. Vogt in SAE Technical Paper Series, SAE International, **2007**.

[117] G. Koltsakis, O. Haralampous, C. Depcik, J. C. Ragone, *Reviews in Chemical Engineering* **2013**, *29*, 1–61.

[118] B. S. Mahadevan, J. H. Johnson, M. Shahbakhti, *Emission Control Science and Technology* **2017**, *3*, 171–201.

[119] P. Tandon, A. Heibel, J. Whitmore, N. Kekre, K. Chithapragada, *Chemical Engineering Science* **2010**, *65*, 4751–4760.

[120] D. Zhong, S. He, P. Tandon, M. Moreno, T. Boger in SAE International400 Commonwealth Drive, Warrendale, PA, United States, **2012**.

[121] K. Premchand, Dissertation, Michigan Technological University, Houghton, **2013**.

[122] J. Gong, S. Viswanathan, D. A. Rothamer, D. E. Foster, C. J. Rutland, *Environmental Science & Technology* **2017**, *51*, 11196–11204.

[123] S. H. Oh, G. B. Fisher, J. E. Carpenter, D. Goodman, *Journal of Catalysis* **1986**, *100*, 360–376.

[124] S. Tischer, C. Correa, O. Deutschmann, *Catalysis Today* **2001**, *69*, 57–62.

[125] H. Stotz, L. Maier, A. Boubnov, A. Gremminger, J.-D. Grunwaldt, O. Deutschmann, *Journal of Catalysis* **2019**, *370*, 152–175.

[126] R. Holder, M. Bollig, D. R. Anderson, J. K. Hochmuth, *Chemical Engineering Science* **2006**, *61*, 8010–8027.

[127] G. Koltsakis, A. M. Stamatelos, *Chemical Engineering Science* **1999**, *54*, 4567–4578.

[128] G. C. Koltsakis, P. A. Konstantinidis, A. M. Stamatelos, *Applied Catalysis B: Environmental* **1997**, *12*, 161–191.

[129] T. S. Auckenthaler, C. H. Onder, H. P. Geering, J. Frauhammer, *Industrial & Engineering Chemistry Research* **2004**, *43*, 4780–4788.

[130] S. K. Rao, R. Imam, K. Ramanathan, S. Pushpavanam, *Industrial & Engineering Chemistry Research* **2009**, *48*, 3779–3790.

[131] H. J. Kwon, J. Hyun Baik, Y. Tak Kwon, I.-S. Nam, S. H. Oh, *Chemical Engineering Science* **2007**, *62*, 5042–5047.

[132] D. N. Tsinoglou, G. C. Koltsakis, J. C. Peyton Jones, *Industrial & Engineering Chemistry Research* **2002**, *41*, 1152–1165.

[133] M. A. Mitsouridis, D. Karamitros, G. Koltsakis, *Emission Control Science and Technology* **2019**, *5*, 238–252.

[134] S. E. Voltz, C. R. Morgan, D. Liederman, S. M. Jacob, *Industrial & Engineering Chemistry Product Research and Development* **1973**, *12*, 294–301.

[135] S. B. Kang, I.-S. Nam, B. K. Cho, C. H. Kim, S. H. Oh, *Chemical Engineering Journal* **2015**, *278*, 328–338.

[136] MATLAB, *version 9.5 (R2018b)*, The MathWorks Inc., Natick, Massachusetts, **2019**.

[137] D. Rose, T. Boger in (Ed.: SAE International), SAE International400 Commonwealth Drive, Warrendale, PA, United States, **2009**.

[138] T. Donateo, M. Giovinazzi, *Energy Procedia* **2017**, *126*, 891–898.

[139] J. S. MacDonald in SAE International, **1983**.

[140] A. G. Konstandopoulos, J. H. Johnson in SAE International, **1989**.

[141] F. Payri, A. Broatch, J. R. Serrano, P. Piqueras, *Energy* **2011**, *36*, 6731–6744.

[142] M. J. Murtagh, D. L. Sherwood, L. S. Socha, *SAE Transactions* **1994**, *103*, 251–261.

[143] S. Marre, J. Palmeri, A. Larbot, M. Bertrand, *Journal of Colloid and Interface Science* **2004**, *274*, 167–182.

[144] I. Belot, D. Vidal, M. Votsmeier, R. E. Hayes, F. Bertrand, *Chemical Engineering Science* **2020**, *221*, 115656.

[145] S. Korneev, S. Onori, *Journal of Dynamic Systems Measurement and Control* **2020**, *142*, DOI 10.1115/1.4046151.

[146] S. Yang, C. Deng, Y. Gao, Y. He, *Advances in Mechanical Engineering* **2016**, *8*, 168781401663732.

[147] G. A. Merkel, D. M. Beall, D. L. Hickman, M. J. Vernacotola in SAE International, **2001**.

[148] Q. Porter, A. Strzelec in SAE Technical Paper Series, SAE International, **2019**.

[149] D. E. Rosner, P. Tandon, *Chemical Engineering Science* **1995**, *50*, 3409–3431.

[150] E. Gal, G. Tardos, R. Pfeffer, *AIChE Journal* **1985**, *31*, 1093–1104.

[151] T. D'Ottavio, S. L. Goren, *Aerosol Science and Technology* **1982**, *2*, 91–108.

[152] V. A. Kirsh, A. A. Kirsh, *Colloid Journal* **2017**, *79*, 481–486.

[153] E. J. Bissett, M. Kostoglou, A. G. Konstandopoulos, *Chemical Engineering Science* **2012**, *84*, 255–265.

[154] J. D. Cooper, A. York, A. J. Sederman, L. F. Gladden, *Chemical Engineering Journal* **2019**, *377*, 119690.

[155] M. Kleiber, R. Joh in *VDI Heat Atlas*, Springer Berlin Heidelberg, Berlin, Heidelberg, **2010**, pp. 119–152.

[156] Landerl, C., Michael, D. Spanring, M. Ruelicke, B. Durst, O. Hartmann, S. Schmuck-Soldan in 26th Aachen Colloquium Automobile and Engine Technology 2017 RWTH Aachen University. - 2, Aachener Kolloquium Fahrzeug- und Motorentechnik GbR, Aachen, **2017**, pp. 35–56.

[157] Cambustion, DMS 500 User Manual: fast particulate analyzer, Cambridge, **2017**.

[158] Horriba LTd., MEXA-2100SPCS user manual, Kyoto, **2019**.

[159] European comissions, Commission Regulation (EC) No 692/2008, **01.07.2017**.

[160] N. R. Collins, M. V. Twigg, *Topics in Catalysis* **2007**, *42-43*, 323–332.

[161] A. Della Torre, G. Montenegro, A. Onorati, G. Tabor, *Energy Procedia* **2015**, *81*, 836–845.

[162] M. Leskovjan, J. Němec, M. Plachá, P. Kočí, M. Isoz, M. Svoboda, V. Novák, E. Price, D. Thompsett, *Industrial & Engineering Chemistry Research* **2021**, *60*, 6512–6524.

[163] R. Greiner, T. Prill, O. Iliev, B. A. van Setten, M. Votsmeier, *Chemical Engineering Journal* **2019**, *378*, 121919.

[164] Y. Wang, J. Gong, C. Su, Q. Ou, Q. Lyu, D. Pui, M. J. Cunningham, *Environmental Science & Technology* **2020**, *54*, 11230–11236.

[165] M. Bonarens, R. Greiner, M. Votsmeier, D. Vidal, *Journal of Aerosol Science* **2022**, *160*, 105900.

[166] VGSTUDIO MAX, *version 3.3*, Volume Graphics GmbH, Heidelberg, Germany, **2019**.

[167] V. Novák, F. Štěpánek, P. Kočí, M. Marek, M. Kubíček, *Chemical Engineering Science* **2010**, *65*, 2352–2360.

[168] R. Walter, J. Neumann, O. Hinrichsen, *Industrial & Engineering Chemistry Research* **2021**, *60*, 16993–17005.

[169] C. K. Dardiotis, O. A. Haralampous, G. C. Koltsakis, *Industrial & Engineering Chemistry Research* **2006**, *45*, 3520–3530.

[170] B. Opitz, A. Drochner, H. Vogel, M. Votsmeier, *Applied Catalysis B: Environmental* **2014**, *144*, 203–215.

[171] J. Cooper, L. Liu, N. Ramskill, T. Watling, A. York, E. Stitt, A. Sederman, L. Gladden, *Chemical Engineering Science* **2019**, *209*, 115179.

[172] M. Václavík, M. Plachá, P. Kočí, M. Svoboda, T. Hotchkiss, V. Novák, D. Thompsett, *Materials Characterization* **2017**, *134*, 311–318.

[173] A. S. Kota, D. Luss, V. Balakotaiah, *Chemical Engineering Journal* **2015**, *262*, 541–551.

[174] P. Kočí, M. Kubíček, M. Marek, *Industrial & Engineering Chemistry Research* **2004**, *43*, 4503–4510.

[175] Hiroaki Koga, Akihide Hayashi, Yoshinori Ato, Kohei Tada, Saburo Hosokawa, Tsunehiro Tanaka, Mitsutaka Okumura, *Catalysis Today* **2019**, *332*, 236–244.

[176] M. Real, R. Hedinger, B. Pla, C. Onder, *International Journal of Engine Research* **2021**, *22*, 640–651.

[177] M. Balenovic, J. H. B. J. Hoebink, A. C. P. M. Backx, A. J. L. Nievergeld in International Fuels & Lubricants Meeting & Exposition, SAE International, **1999**.

[178] J. Xu, R. Clayton, V. Balakotaiah, M. P. Harold, *Applied Catalysis B: Environmental* **2008**, *77*, 395–408.

[179] H. J. Kwon, J. H. Baik, S. B. Kang, I.-S. Nam, B. J. Yoon, S. H. Oh, *Industrial & Engineering Chemistry Research* **2010**, *49*, 7039–7051.

[180] M. H. Allouche, R. Enjalbert, F. Alberini, M. Ariane, A. Alexiadis, *Chemical Engineering Research and Design* **2017**, *117*, 681–687.

[181] T. Shamim, H. Shen, S. Sengupta, S. Son, A. A. Adamczyk, *Journal of Engineering for Gas Turbines and Power* **2002**, *124*, 421–428.

[182] T. Shamim, *Energy Conversion and Management* **2008**, *49*, 3292–3300.

[183] Q. Su, L. Xie, Y. Li, X. Qiao, *Canadian Journal of Chemical Engineering* **2014**, *92*, 1579–1586.

[184] F. Zeng, J. Finke, D. Olsen, A. White, K. L. Hohn, *Chemical Engineering Journal* **2018**, *352*, 389–404.

[185] K. Ramanathan, C. S. Sharma, C. H. Kim, *Industrial & Engineering Chemistry Research* **2012**, *51*, 1198–1208.

[186] M. Weilenmann, *Catalysis Today* **2012**, *188*, 121–134.

[187] A. Della Torre, G. Montenegro, A. Onorati, S. Paltrinieri, F. Rulli, V. Rossi, *Industrial & Engineering Chemistry Research* **2021**, *60*, 6653–6661.

[188] P. Kumar, T. Gu, K. Grigoriadis, M. Franchek, V. Balakotaiah, *Chemical Engineering Science* **2014**, *111*, 180–190.

[189] J. Bickel, B. Odendall, G. Eigenberger, U. Nieken, *Chemical Engineering Science* **2017**, *160*, 34–53.

[190] C. Guardiola, H. Climent, B. Pla, M. Real, *Proceedings of the Institution of Mechanical Engineers Part D: Journal of Automobile Engineering* **2019**, *233*, 3758–3774.

[191] K. Schürholz, D. Brückner, D. Abel, *Topics in Catalysis* **2019**, *62*, 288–295.

[192] H. Arunachalam, G. Pozzato, M. A Hoffman, S. Onori in *IEEE Conference on Control Technology and Applications (CCTA)*, **2017**.

[193] P. L. Silveston, *Catalysis Today* **1995**, *25*, 175–195.

[194] D. Ferri, M. Elsener, O. Kröcher, *Applied Catalysis B: Environmental* **2018**, *220*, 67–77.

[195] D. Bounechada, G. Groppi, P. Forzatti, K. Kallinen, T. Kinnunen, *Applied Catalysis B: Environmental* **2012**, *119-120*, 91–99.

[196] X. Shi, R. Seiser, J.-Y. Chen, R. Dibble, R. Cattolica, *SAE International Journal of Engines* **2015**, *8*, 1246–1252.

[197] B. Pla, L. M. Garcia-Cuevas, C. Guardiola, M. Real in SAE Technical Paper Series, SAE International, **2019**.

[198] T. Shamim, *International Journal of Automotive Technology* **2011**, *12*, 475–487.

[199] J. Gong, J. Pihl, W. Di, M.-Y. Kim, W. P. Partridge, J. Li, M. Cunningham, K. Kamasamudram, N. Currier, A. Yezerets, *Catalysis Today* **2021**, *360*, 294–304.

[200] Q. Su, PhD thesis, Heidelberg University, **2009**.

[201] B. Opitz, M. Votsmeier, *Chemical Engineering Science* **2016**, *149*, 117–128.

[202] C. Dubien, D. Schweich, G. Mabilon, B. Martin, M. Prigent, *Chemical Engineering Science* **1998**, *53*, 471–481.

[203] S. B. Kang, S. J. Han, I.-S. Nam, B. K. Cho, C. H. Kim, S. H. Oh, *Chemical Engineering Journal* **2014**, *241*, 273–287.

[204] R. Möller, M. Votsmeier, C. Onder, L. Guzzella, J. Gieshoff, *Applied Catalysis B: Environmental* **2009**, *91*, 30–38.

[205] J. Rink, N. Meister, F. Herbst, M. Votsmeier, *Applied Catalysis B: Environmental* **2017**, *206*, 104–114.

[206] J. Gong, Di Wang, J. Li, K. Kamasamudram, N. Currier, A. Yezerets, *Catalysis Today* **2019**, *320*, 51–60.

[207] R. Wunsch, C. Schön, M. Frey, D. Tran, S. Proske, T. Wandrey, M. Kalogirou, J. Schäffner, *Applied Catalysis B: Environmental* **2020**, *272*, 118937.

[208] S. H. Oh, T. Triplett, *Catalysis Today* **2014**, *231*, 22–32.

[209] A. B. Arvajová, P. Boutikos, P. Kočí, R. Pečinka, *Applied Catalysis B: Environmental* **2020**, *260*, 118141.

[210] J. Barbier, D. Duprez, *Applied Catalysis A: General* **1992**, *85*, 89–100.

[211] R. Dictor, *Journal of Catalysis* **1987**, *106*, 458–463.

[212] V. Palma, C. Ruocco, M. Cortese, M. Martino, *Catalysts* **2019**, *9*, DOI `10.3390/catal9120991`.

[213] O. Kröcher, M. Elsener, M. Votsmeier, *Industrial & Engineering Chemistry Research* **2009**, *48*, 10746–10750.

[214] J. Kennedy, R. Eberhart in Proceedings of ICNN'95 - International Conference on Neural Networks, IEEE, **27 Nov.-1 Dec. 1995**, pp. 1942–1948.

[215] A. Pedlow, G. McCullough, A. Goguet, O. Garcia-Afonso, D. Sellick, *Emission Control Science and Technology* **2018**, *4*, 113–133.

[216] J. C. Lagarias, J. A. Reeds, M. H. Wright, P. E. Wright, *SIAM Journal on Optimization* **1998**, *9*, 112–147.

[217] B. Giechaskiel, V. Valverde, A. Kontses, R. Suarez-Bertoa, T. Selleri, A. Melas, M. Otura, C. Ferrarese, G. Martini, A. Balazs, J. Andersson, Z. Samaras, P. Dilara, *Atmosphere* **2021**, *12*, 1011.

[218] J. H. Lee, M. J. Paratore, D. B. Brown, *SAE International Journal of Fuels and Lubricants* **2009**, *1*, 96–101.

[219] Y. He, D. B. Brown, S. Lu, M. J. Paratore, J. Li in SAE Technical Paper Series, SAE International, **2009**.

[220] C. K. Dardiotis, O. A. Haralampous, G. C. Koltsakis, *Chemical Engineering Science* **2008**, *63*, 1142–1153.

[221] K. G. Rappé, *Industrial & Engineering Chemistry Research* **2014**, *53*, 17547–17557.

[222] D. Karamitros, G. Koltsakis, *Chemical Engineering Science* **2017**, *173*, 514–524.

[223] A. Punke, G. Grubert, Y. Li, J. Dettling, T. Neubauer in SAE Technical Paper Series, SAE International, **2006**.

[224] I. Belot, Y. Sun, D. Vidal, M. Votsmeier, P. Causse, F. Trochu, F. Bertrand, *Chemical Engineering Journal* **2021**, *405*, 126653.

[225] M. Chase Jr., *J. Phys. Chem. Ref. Data* **1998**, 1–1951.

[226] M. Kostoglou, E. J. Bissett, A. G. Konstandopoulos, *Industrial & Engineering Chemistry Research* **2012**, *51*, 13062–13072.

[227] H. Seong, S. Choi, S. Lee, N. J. Zaluzec, T. J. Toops, M. J. Lance, D. Kim, K. Nguyen, *Industrial & Engineering Chemistry Research* **2019**, *58*, 10724–10736.

[228] S. Y. Joshi, M. P. Harold, V. Balakotaiah, *Chemical Engineering Science* **2010**, *65*, 1729–1747.

[229] O. Deutschmann, J.-D. Grunwaldt, *Chemie Ingenieur Technik* **2013**, *85*, 595–617.

[230] Z. Zheng, X. Tian, X. Zhang, *Applied Thermal Engineering* **2015**, *84*, 237–245.

[231] K. Ramanathan, S. H. Oh, *Chemical Engineering Research and Design* **2014**, *92*, 350–361.

List of Figures

List of Tables

Reprint Permissions

ACS Permissions

Extended Model for Filtration in Gasoline Particulate Filters under Practical Driving Conditions

Author: Raimund Walter, Jens Neumann, Olaf Hinrichsen
Publication: Environmental Science & Technology
Publisher: American Chemical Society
Date: Aug 1, 2020

Copyright © 2020, American Chemical Society

Modeling the Catalytic Performance of Coated Gasoline Particulate Filters under Various Operating Conditions

Author: Raimund Walter, Jens Neumann, Olaf Hinrichsen
Publication: Industrial & Engineering Chemistry Research
Publisher: American Chemical Society
Date: Dec 1, 2021

Copyright © 2021, American Chemical Society

Applying 3D X-ray Microscopy to Model Coated Gasoline Particulate Filters under Practical Driving Conditions

Author: Raimund Walter, Jens Neumann, Astrid Velroyen, et al
Publication: Environmental Science & Technology
Publisher: American Chemical Society
Date: Aug 1, 2022

Copyright © 2022, American Chemical Society

Elsevier Permissions

A model-based analysis of washcoat distribution on zoned coated gasoline particulate filters

Author: Raimund Walter, Jens Neumann, Olaf Hinrichsen

Publication: Chemical Engineering Journal

Publisher: Elsevier

Date: 1 August 2022

Journal Author Rights

List of Publications

Peer Reviewed Journal Publications

- *Extended Model for Filtration in Gasoline Particulate Filters under Practical Driving Conditions*, R. Walter, J. Neumann, O. Hinrichsen, **Environ. Sci. Technol. 2020** 54 (15), S. 9285–9294. DOI:10.1021/acs.est.0c02487.

- *Modeling the Catalytic Performance of Coated Gasoline Particulate Filters under Various Operating Conditions*, R. Walter, J. Neumann, O. Hinrichsen, **Ind. Eng. Chem. Res.** 2021 60 (47), S. 16993–17005. DOI:10.1021/acs.iecr.1c03631

- *A model-based analysis of washcoat distribution on zoned coated gasoline particulate filters*, R. Walter, J. Neumann, O. Hinrichsen, **Chem. Eng. J.** 2022 441, S. 135615. DOI: 10.1016/j.cej.2022.135615

- *Applying 3D X-Ray Microscopy to Model Coated Gasoline Particulate Filters under Practical Driving Conditions*, R. Walter, J. Neumann, A. Velroyen, O. Hinrichsen, **Environ. Sci. Technol.** 2022 56 (17), S. 12014-12023. DOI:10.1021/acs.est.2c01244.

Acknowledgments

This dissertation would not be possible without the help and support of numerous persons. My thanks to you all. The last four years were a very intense time with a mixture of stress, hopelessness, failures but also companionship, happiness, achievements, and fun, resulting in incredible personal growth.

Firstly, I would like to thank Prof. Dr.-Ing. Olaf Hinrichsen for accepting me into your research group and the trust you placed in me as an external PhD student. Beyond that, I am grateful for your guidance, your scientific suggestions and for granting me the freedom to pursue this project at BMW. I would also like to thank Prof. Dr.-Ing Harald Klein for spending your precious time in reading and evaluating this thesis.

Secondly, I would like to express my sincere gratitude to my BMW supervisor Jens Neumann. Without your dedication to create my PhD position in a first place, this project would not have been possible. Your demand for accuracy and the long discussions were sometimes challenging but helped me to develop the necessary skills and continuously pushed this work to the next step. Further, I am very grateful for the help and support of my EA-3 colleagues at BMW. On behalf of the many other colleagues, I would like to thank Nikita and Mario for the discussions about aftertreatment as well as Malte for helping me with the measurement automation. Also, I would like to thank you Janosch for many late-evening white board sessions and making the "Dok-office" a fun place to work. The BMW doctoral network was a great resource during this time. The projects we did together in the communication team have been a lot of fun and helped to improve my skills. Here, a special thanks goes to Max for correcting dozens of newsletters I wrote. Also, thanks to my students Sidney and Benni for creating nice looking front ends and forcing me to make my code more user friendly as well as to you Zhipeng for giving my simulations a third dimension.

Of course, my gratitude also goes to my family and friends for your motivational support and taking my mind off work. You tried your best in the last few years to prolong this project by inviting me to hikes, boardgame evenings and weekend trips. Here, a special thanks to my friends from the BMW doctoral network who can mostly be called Dr. already: Your support and the fun activities we did were a pillar during this time. Also, I would like to thank my friends from home, Tobi and Alex, your commitment you put into building your startup motivated me, especially in the early phase, to work hard on

my dissertation. Thanks to my sister Charlotte, we had a lot of fun in learning how to handle the new SY Dschambo together. I am also deeply thankful to my parents, Karin, and Mathias. Thank you for years of investment in my education and your unconditional support. You all made this document possible.